Engineered Supraparticles and Their Photocatalytic Applications

by

Naomi S. Ramesar

A dissertation submitted in partial fulfillment
of the requirements for the degree of
Doctor of Philosophy
(Chemical Engineering)
in the University of Michigan
2021

Doctoral Committee:

Professor Nicholas A. Kotov, Chair
Professor Melanie S. Sanford
Dean Michael J. Solomon
Professor Emeritus Levi T. Thompson

Naomi S. Ramesar

nramesar@umich.edu

ORCID iD: 0000-0002-8848-8308

Dedication

To my mom

Acknowledgements

First and foremost, I would like to express my sincere gratitude to my advisor, Professor Nicholas Kotov. I am grateful for his patience, support, and positive perspective on life. His enthusiasm and creativity as a scientist have inspired me immensely throughout the years. I appreciate Prof. Kotov's overall positivity as an advisor, it has helped me realize my abilities and potential when I could not recognize them myself.

I would also like to thank my committee members, Professors Melanie Sanford, Michael Solomon, and Levi Thompson, for their support and guidance. I am grateful to Prof. Solomon and Levi for making my transition to UofM a very welcoming experience. I am especially thankful for Levi's humor and mentorship throughout the years.

I would like to thank Professor Sharon Glotzer, Trung, and Thi for many insightful conversations. Additionally, I am grateful to Kai Sun for all the technical support on TEM and SEM.

I am thankful to the Department of Chemical Engineering and the staff (particularly Mary Beth Westin and Susan Hamlin) for their support and friendly conversations, and the University of Michigan for the Rackham Merit Fellowship.

I am appreciative to Renuka Sankaran, and Ilona Kretzschmar, my undergraduate and master's research advisors, for instilling the passion and motivation to pursue a PhD.

Over the years, I have had the opportunity and privilege to work alongside many talented individuals, developing relationships that blossomed into friendships, enriching the entire PhD

experience. I am grateful for all interactions between past and present Kotov lab members. Particularly, this journey would not be the same without Gleiciani Silveira, Luiz Gorup, Mahshid Chekini, Jihyeon Yeom, Minjeong Cha, Sumeyra Emre, Ahmet Emre, Doug Montjoy, Ming Lei, Wonjin Choi, Sunny (Mingzhu Li), and Joong Hwan Bahng. Thank you for all the Starbucks happy hours and Brazilian BBQs (picanha). Additionally, I am thankful to Valentina Omoze, Maria Ma, and Hanieh Safari for all the long days and nights we spent studying together during my first year.

I am especially thankful to my family, my mom, Stacey, sister, Sarah, and niece, Samantha; they have been my biggest supporters. My mom has worked tirelessly to see me stand where I am today, and I am forever grateful.

Most importantly, I would like to express my sincere appreciation to my husband, Jason Martinez. This year has been quite eventful, newborn twins, a pandemic, and two defenses. While Jason has motivated me throughout the years, his support during this year is more than I could have asked for.

Lastly, I could not end this without acknowledging my 11-month-old twins, Miya and Raphy. They have been the most loving and happy distractions during the dissertation writing process! Watching them grow and learn over this year has given me immense purpose and drive.

Thank you. Obrigado. Teşekkür Ederim. Gamsahabnida. Merci. Gracias. Xiexie.

Table of Contents

List of Tables

List of Figures

Abstract

Nature has developed highly specific and efficient catalysts to synthesize complex organic compounds, such as sugars in the process of photosynthesis. Due to the efficiency of these reactions, considerable effort has been placed to develop reaction schemes that can replicate the complexity of catalysts and products found in nature. The success of producing these biomimetic systems often leads to an improved understanding of biological systems, which can loop back and translate into better engineering of catalysts, aiming for instance, for enhanced stability and reduced cost.

The use of inorganic nanoparticles (NPs) for developing biomimetic catalytic systems presents a favorable choice due to their ability to combine the robustness of inorganic catalysts with selectivity similar to that of enzymes.[1] Other structural and functional characteristics similar to those of proteins can also be attained.[2] Advancement in the understanding of NP self-assembly mechanisms allowed us to engineer terminal superstructures, known as supraparticles (SPs).[3] The formation of SPs is not limited to the self-organization of inorganic NPs. Hybrid assemblies, containing NPs and multiple proteins at the same time have been developed.[4,5] All these superstructures can potentially display catalytic functionalities replicating those of enzymatic assemblies,[4] improving catalytic properties compared with singular NPs constituents due to collective interactions.[6]

The tight structural integration of NPs in SPs enhances the stability of catalysts mitigating irreversible aggregation of individual constituents. Physical dimensions of SPs with 100 nm range offer simplicity of separation.[7] Combining properties of both inorganic and biological nanoscale structures, SPs assemblies provide a cost-effective alternative to enzymes and can also improve current inorganic NPs catalysts.

Although there is evidence that suggests SPs have a positive impact on catalysis,[7–9] there is limited research studying SP catalysis, highlighting the need for improved understanding and engineering of such assemblies. This thesis provides an array of multicomponent engineered structures with a vast range of applications, from drug delivery to photocatalysis.

Initially, the facile formation of five hybrid SP assemblies composed of varying proteins, protease, formate dehydrogenase, and cytochrome C, and nanoparticles, iron disulfide, cadmium telluried, and zinc oxide, were explored. Ultimately, the work showed how counter-balancing the attractive and repulsive interactions in the system can lead to the formation of self-limiting assemblies with a wide variety of components, introducing several layers of functionality. SPs were then utilized for applications in encapsulation and cargo protection.

The self-assembly of terminal inorganic SPs, composed of a variety of semiconductor nanoparticles and their range of photocatalytic applications from chiral enantioselectivity to enhanced photo-Fenton systems were examined. Specifically, chiral zinc sulfide (ZnS) SPs, composed of L/D-penicillamine ZnS NPs and L/D-glutathione gold (Au) NPs, were self-assembled and utilized for the enantioselective conversion of L/D-tyrosine to dityrosine. SPs introduced interstitial gaps between NPs, mimicking chiral centers of enzymes, while combining the plasmonic properties of Au to achieve an enantioselective efficiency 10x better than comparable inorganic NPs.

Further studies investigated the structural flexibility offered by inorganic SPs. First, the facile one-pot, low temperature (70 °C) synthesis of spiky cadmium sulfide nanoparticles with tunable size and spike density was explored. Particles exhibited emission independent down- and up-conversion property which was explored for the degradation of rhodamine B dye under four illumination sources, ultraviolet, visible, infrared, and Xenon. Particularly showing the unexpected degradation under IR illumination. Lastly, for the first time, the formation of a wide spectrum of fibrous SP assemblies from erdite, $NaFeS_2$-$2H_2O$, by controlling the ionic strength of the synthesis medium was investigated. The SPs were employed as a photo-Fenton catalyst for the degradation of methylene blue and a model lignin compound, guaiacylglycerol-beta-guaiacyl ether. Particles showed proficient dispersion stability and excellent catalytic recyclability.

Overall, SPs are a convenient platform for engineering catalysts using different building blocks as functional modules, leading to the development of more specific and sophisticated assemblies capable of replicating multiple functions of biological nanoassemblies.

Chapter 1

Background

1.1 Self-assembly

Self-assembly is the spontaneous organization of components into ordered assemblies without external contributions. Nature is the prime example of the importance and complexity of self-assembly, with a range of essential self-assembled structures, such as protein aggregates, lipid membranes, viral capsids, and several other biological components. Inspired by these intricate assemblies, scientist have aspired not only to understand the underlying processes but replicate and create biomimetic constructs. These hierarchical assemblies are tailored to exhibit properties and functionalities similar to components found in nature.

Typically, the self-assembly of building blocks occurs through thermodynamic constraints, where chemical and structural compatibility is crucial. These weak noncovalent interactions are contributions from van der Waals and Coulombic interactions, hydrogen bonds, and hydrophobic interactions[10]. However, self-assembly processes governed by thermodynamic equilibrium may not necessarily be kinetically favorable. There is an essential need to engineer self-assembled structures by tuning their interactions[11] and finding pathways to overcome kinetic traps[12].

1.1.1. Terminal assemblies

Self-limiting self-assemblies are defined by systems composed of finite sizes and shapes. These structures, otherwise known as terminal assemblies, are prominent in biological systems, exemplified by viral capsids, exosomes, endosomes, and micelles. The realization of terminal assemblies for nanoparticles not only provides crucial insight into the self-assembly processes and interactions required to form these unique structures but ultimately leads to sophisticated designs paralleling biological components using facile and inexpensive precursors. In recent years, the advancement in nanoparticle design and assembly has led to new and exciting biomimetic structures that can replicate the chemical and/or structural properties of biological components.[2]

1.2 Supraparticles

The formation of high order nanostructures through the self-assembly of NPs present an opportunity to fabricate a new class of materials with desired physical, chemical, and optical properties, collective or synergistic of their NP constituents.[6] Advancement in the synthesis of uniform NPs with tunable size, controlled shape, and surface functionalization has led to the natural progression of self-assembled NPs into superstructures. These high order nanostructures, otherwise known as supraparticles (SPs), are mainly inspired by the complexity of the self-limiting self-assembly of diverse protein superstructures in biological systems.[3,13] SPs have been used in various applications ranging from photovoltaics[14], optics,[15] and drug delivery[16]. They are generally formed through the self-assembly of two or more subunits and are categorized into two types, inorganic or hybrid (inorganic-organic), based on the composition of their constituents. The formation of SPs typically occur through the self-organization of anisotropic interactions between

uniformly shaped NP building blocks (electrostatic/van der Waals) and with the environment (solvophobic/solvophillic interactions) (**Figure 1-1**).[17,18]

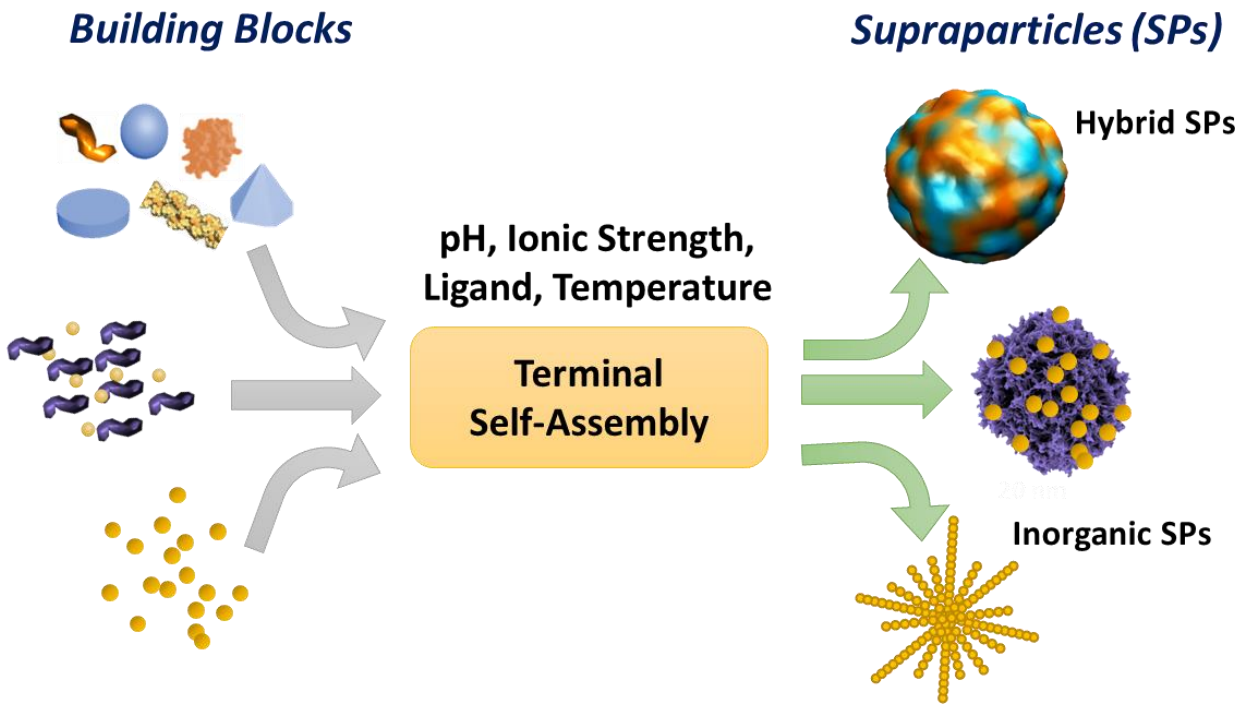

Figure 1-1. Building block components, composed of similar or different subunits, self-assembled into uniform terminal supraparticles assemblies under specific conditions.

Formation of SPs can be accomplished via two distinctive routes. For the first type, NP synthesis and self-assembly take place in two separate steps, while in the second type the NP nucleation, growth and self-assembly occurs continuously. In general, NP attachment can be influenced by different components in the dispersion media such as concentration, size, stabilizing ligands, solvent, ionic strength, pH, temperature, etc.[19] In this method of SP formation, NP of any composition may be combined as there is more freedom in adjusting the physio-chemical conditions (composition, concentration, temperature) under which the self-assembling process

takes place. The second method has some experimental restrictions as synthesis and assembly occur simultaneously. However, there are few examples of SP formation in NP synthesizing medium[3,20,21] which highlights the lack of attention for this process despite the fact that it is an intermediate stage in the formation of many nanocrystalline structures via crystallographic fusion.[22,23]

There has been considerable progress in developing a comprehensive understanding of the electrostatic interactions that govern the self-assembly of SPs.[3,4,15,24] The information gained through these studies allow for a better understanding and ease in the fabrication of SPs if general interactions are properly controlled within the system. Xia *et al.* showed the self-assembly of non-uniformly sized NPs into monodispersed core/shell SPs were governed by a balance between electrostatic repulsion and van der Waals attraction.[3] The strong electrostatic repulsion within the SPs produced a loosely packed core of larger particles while smaller particles packed on the outside. Cao *et al.* was able to take advantage of the solvophobicity interactions by controlling the ligand and reducing agent in solution to assist in the formation of aligned hexagonal close-packed structures composed of nanorods.[15]

The primary interactions between the NPs in the system are governed by a balance between van der Waals attraction and screened electrostatic repulsion[3]. Therefore, the potential energy between NPs can then we represented as equation (1-1):

$$U(r) = 4\varepsilon\left[\left(\frac{\sigma}{r}\right)^{12} - \left(\frac{\sigma}{r}\right)^{6}\right] + A\,\frac{\exp(-\frac{\kappa r}{\sigma})}{r/\sigma} \qquad (1\text{-}1)$$

where r is the center-center distance between two NPs, ε is the attraction strength, σ is the length scale, A is the strength of the electrostatic repulsion and κ is the inverse screening length. Here,

the first term of the equation represents the van der Waals attraction, while screened electrostatic repulsion is the latter portion.

1.2.1 Inorganic Supraparticles

Monodisperse inorganic SPs exhibit unique magnetic[25], optical,[15] and catalytic properties[9,26] owing to their well-defined shapes and topological structures.[6] For example, uniform CdS colloidal spheres (80-500nm) synthesized through a solvothermal technique were able to assemble into films, which exhibited characteristic stop bandgap of photonic crystals.[27] The formation of Fe_3O_4 SPs from 8 nm NPs achieved magnetic moments that were four orders of magnitude larger than the individual NPs.[28] While these unique properties due to the collective or synergistic effects of the building blocks have been observed, modulation and/or predictions of this collective nature has not been achieved. Therefore, a more thorough understanding of inorganic SP formation is required. The observations encountered in these assemblies provide sufficient information (i.e., on the fabrication and distinct properties of inorganic SPs) to expand these techniques into more complex systems, such as those which include organic components.

1.2.2 Hybrid (inorganic-organic) Supraparticles

The high selectivity and specificity of enzymes make them ideal catalysts. However, enzymes are sensitive to changes in the environment (i.e. pH, salt content, solvent, etc.) and thus have inherent drawbacks when used as catalysts. The incorporation of proteins into hybrid SPs is an attractive approach that make them favorable for catalysis owing to their inherent chemical and structural properties,[29] enabling them to perform specific functions. Additionally, interactions at the protein-NP interface suggest that the immobilization of proteins on the NP surface can not only increase

the stability of the protein against degradation, but also improve enzyme activity.[4,30,31] Thus, immobilization of protein via SPs offer a potential to increase the yield of the desired product and allow for easy separation from catalyst/support.

The underlying forces responsible for formation of hybrid terminal assemblies of similarly charge, cadmium telluride (CdTe) NPs and cytochrome C (CytC) protein was examined for the first time, to be due to the counterbalancing of electrostatic repulsion with intermolecular attractive interactions, including dipolar, hydrogen bonding, hydrophobic interactions, and van der Waals forces.[4] Therefore, only generic attractive-repulsive forces are required for the formation of the terminal SPs, and they can be made from a variety of NPs and proteins. Other examples of hybrid protein-NP clusters have been developed[32,33] and support the conclusion presented by Park *et al*.[4] The properties of these newly fabricated SP assemblies make them an attractive tool to potentially aid in developing and understanding complex biological systems, such as the cascade reaction involved in photosynthesis.

1.3 Heterogeneous Photocatalysts

A photocatalysts is a material that can adsorb solar energy and use it to drive reactions. Heterogeneous catalysis uses a catalyst material that is different from the reactants, most commonly these materials are transition metal oxides and semiconductors.

1.3.1 Semiconductors

Semiconductors are materials that absorbs photons with energy equal to or more than its band gap, exciting an electron to generate an electron-hole pair. An excited electron resides in the conduction band, while it leaves a hole in the valance band. The generation of an electron-hole pair, otherwise known as charge carriers, can drive oxidation and reduction reactions, through the formation of

radical species. Many wide-band-gap transitions metals are commonly used; however, they are limited to irradiation in the ultraviolet (UV) region. Therefore, to benefit from most of the solar irradiation, current research emphasizes the need for shifting photoactivity towards the visible (VIS) and even near infrared (NIR). This may be achieved through low-band-gap semiconductors and other photoactive materials (such as organic dyes, organic complexes, or metallic NPs). Additionally, taking advantage of the crystalline nanoscale heterojunctions formed by different types of semiconductors, shows improvements in photocatalytic activity and stability of the materials. This introduces an area of research that may be filled using the combination of components

1.3.2 Supraparticles as catalysts

Current catalysts are hindered by their lack of stability, which leads to leaching and or support dissolution.[7] The most common catalyst used in industrial applications are noble metal particles on oxide supports,[8] however, they are also plagued by instability. The leaching of active particles or degradation of the support material leads to eventual deactivation of the catalyst. To alleviate this problem, the development of mesoporous SPs were implemented as catalyst to address the issue of aggregation by separating metal particles from each other while keeping them immobilized in a tightly integrated structure.[7] In a proof of concept, Hu *et al.* showed an increase in the reaction rate for the reduction of hexacyanoferrate for their mesoporous SPs (88 %) versus Pt NPs (40 %), which may be attributed to a difference in the accessibility of surface area for each nanostructure.[7] This serves as supporting evidence that SPs can be high-performance catalyst with enhanced stability with further development.

The use of SPs as a catalyst has shown to enhance the overall activity of the reactions when compared to their NP components.[7–9,34] SPs used for catalysis are observed in both inorganic and hybrid superstructures, taking advantage of individual building blocks such as transition metal oxides, noble metals, and enzymes. Au-CeO_2 SPs presented by Chen *et al.* exhibited a 97.7 % (beginning at 40 °C) conversion of CO up to temperatures of 500 °C while the Au on bulk CeO_2 decreased from 97.4 % (beginning at 78 °C) to just 14 % at 415 °C.[8] Bionic SPs consisting of CdTe NPs and CytC showed a four-fold increase in the light-driven reduction of nitrate when nitrate reductase was incorporated within the SPs versus unaided.[4] SPs can be easily separated and removed from the reactor by mild centrifugation in most cases, and reused, making it a cost efficient and green catalyst. While SPs show a positive influence in catalysis, there is insufficient research on the subject, highlighting the main motivation to improve and better understand the engineering of SPs for utilization as catalysts.

1.3.3 Chiral Catalysis

Chirality is defined as an object or system that cannot be superimposed onto its mirror image. These chiral molecules and their mirror images are called enantiomers, L or D. Chirality plays a crucial role in biological systems as most cell components are composed of chiral molecules, such as amino acids and sugars. Most naturally occurring amino acids are L, while most sugars are D. A critical example of the importance of correct enantiomeric selectivity dates to post-World War II, when the sleep agent thalidomide was heavily used by pregnant women to treat morning sickness. Thousands of babies were born with teratogenicity, a birth defect resulting in missing or deformed limbs. Studies revealed that thalidomide was produced using a racemic mixture, where

(+) thalidomide was a sedative and (-) thalidomide was a teratogenic[35]. This stresses the important of developing enantioselective catalyst.

While there has been considerable research directed towards the development of enantioselective catalyst, with current catalyst including metal-organic frameworks, metal clusters, or metal oxides, there is still significant room for improvement in catalysts that yield preferential homochiral products. Current systems are limited due to leaching and decomposition, difficult synthesis methods, reproducibility, recycling, and crystallinity. Some of these problems can be addressed by using chiral inorganic NPs due to their high crystallinity, recyclability, improved surface area and chirality at various length scales.

Chapter 2

Supraparticle Nanoassemblies with Enzymes

Naomi S. Ramesar*, Gleiciani de Q. Silveira*, Trung D. Nguyen, Joong H. Bahng, Sharon C. Glotzer and Nicholas A. Kotov. *Chem. Mater. 2019, 31, 18, 7493–7500*

2.1 Abstract

Supraparticles are micelle-like self-limited assemblies from inorganic nanoparticles (NPs), whose size and morphology are determined by the equilibrium between short-range attraction and long-range repulsion forces. They can be spontaneously assembled from a variety of nanoscale components that are, in the majority of cases, the same NPs. Hybrid supraparticles made from inorganic and biological components are possible but hardly known. We report here the self-assembly of hybrid bioinorganic supraparticles, prepared from iron disulfide, cadmium telluride, and zinc oxide NPs as well as protease, cytochrome c, and formate dehydrogenase, in which the protein content can exceed that of NPs by 3:1. The resulting bioinorganic supraparticles are 70-150 nm in diameter and have a narrow size distribution. Five different permutations of inorganic and biological components indicate the generality of the observed phenomena. Coarse-grained molecular dynamics simulations confirmed that the formation of supraparticles depends on the interplay between attraction strengths and electrostatic repulsion. Enzymatic activity of the native protein is retained and is completely recovered from the assemblies, which suggests that the supraparticles can be utilized for encapsulation of biomolecules.

2.2 Introduction

The self-assembly of terminal structures, such as viral capsids[36], endosomes[37], membrane-less compartments, and micelles, play quintessential roles in all biological systems being responsible for encapsulation of cargo[36], signaling[38], optical interactions[39], catalysis[40], and many other functions. Thus, considerable effort has been placed on fabricating biomimetic assemblies to improve the understanding of terminal self-assembled structures in biology.[1,2,41–43] Although it might seem counter-intuitive, inorganic nanoparticles (NPs) presents a favorable choice because of their tunable size, shape, charge, surface functionality, and amazing simplicity with which they form terminal assemblies,[6] known as supraparticles (SPs).[3,13] One of the fundamental advantage of SPs is the possibility to combine nanoscale components with different properties, which, besides the fundamental importance for property engineering, opens the door for a variety of applications ranging from photovoltaics[14] and optics,[15] to drug delivery.[16]

SPs formed through the self-assembly of two or more subunits may be categorized into two types, inorganic or hybrid (inorganic–organic), based on the composition of their constituents. The formation of SPs typically occurs through the interplay between repulsive and attractive forces exemplified by electrostatic and supramolecular interactions that can also be complemented by solvophobic/solvophillic interactions.[17,18]

There has been considerable progress in developing a comprehensive understanding of the interactions that govern the self-assembly of SPs.[3,4,15,24,44] The information gained through these studies allow for better understanding and ease in the fabrication of SPs if general interactions are properly controlled within the system. Xia et al. showed that the self-assembly of nonuniform-sized NPs into monodispersed core/shell SPs were governed by a balance between electrostatic

repulsion and vdW attraction.[3] The strong electrostatic repulsion within the SPs produced a loosely packed core of larger particles, whereas smaller particles packed at the SP outer layers. Cao et al. were able to take advantage of the solvophobic interactions by controlling the ligand and reducing agent in a solution to assist in the formation of aligned hexagonal close-packed structures composed of nanorods.[15] The formation of hybrid terminal SPs of similarly charge, cadmium telluride (CdTe) NPs and cytochrome C (CytC) protein, was thoroughly explored in 2014[4] and the underlying forces responsible for this SP formation was found to be the counterbalancing of electrostatic repulsion with intermolecular attractive interaction, including dipolar, hydrogen bonding, and hydrophobic interactions. It was concluded that nonspecific attractive-repulsive forces are required for the formation of the hybrid SPs, suggesting they can be made from a variety of NPs and proteins. Other examples of hybrid protein-NP clusters have been developed[32,33,43,45,46] and support the conclusion presented by Park *et al*.[4] Simultaneously, it was observed that some proteins, for instance, streptavidin, prevents self-assembly of CdTe NPs.[47]

Considering the biological role or many terminal assemblies, SPs can be utilized to protect their biological components from degradation. Enzymes are sensitive to changes in the environment (i.e., pH, salt content, solvent, etc.), which is the central limitation for their production and applications.[48] The high cost of isolation and purification of enzymes makes their recovery and reuse a challenging process.[49] Several benefits can be achieved through utilizing hybrid SPs as a tool for enzyme encapsulation, as interactions at the protein/NP interface suggest that the immobilization of proteins on the NP surface can not only increase the stability of the protein against degradation, but also improve enzyme activity.[4,30,31] SPs can prevent enzymes' contact with other particles, proteins, surfactants, and surfaces that can cause their inactivation. Also, they can stabilize the enzymes under unfavorable conditions, such as high temperature (70 °C), ionic

strengths and pH.[4] Furthermore, SPs may also show improved catalytic properties over their individual NP constituents.[6]

In this work, we present five variations of hybrid SPs, self-assembled from proteins and NPs of various shapes. Iron disulfide (FeS_2) NPs stabilized with thioglycolic acid (TGA) and zinc oxide (ZnO) NPs of various shapes (plates, spheres, and pyramids) were combined with protease, and CdTe NPs stabilized with 2-(dimethylamino)ethanethiol (DMAET) were assembled with two proteins, CytC and formate dehydrogenase (FADH). A prominent feature of this work is to highlight the engineering of stable and tunable hybrid assemblies that can be applied as a class of nano-tools for a range of applications, specifically biomolecule encapsulation and recovery. The properties of these newly fabricated SP assemblies also make them an attractive tool to potentially aid in the development and understanding of complex biological systems.

2.3 Experimental Method

Synthesis of FeS_2 nanoparticles (NPs): TGA-FeS_2 NPs were obtained by combination of two different methods described in the literature.[50,51] In a typical synthesis, 90 mL of DMSO was heated to 180 °C in a three-neck flask (150 mL) fitted with a valve and degassed by bubbling nitrogen under magnetic stirring for 1h. Thioglycolic acid (10 mmol; 0.69 mL) was injected and after 1 h the $FeCl_2.4H_2O$ (1.3 mmol; 259 mg) was quickly added to the flask avoiding air entry into the flask. After refluxing for more 1h at 180 °C the pH of media was ajusted to 9.0. A solution consisting of sulfur (11.7 mL; 0.374 mg) in diphenyl ether (8 mL) degassed at 70°C for 1 h was added to the reaction mixture and immediately the solution became black and was kept at 180°C for 3 h. The reaction was stopped with a room temperature water bath. The NPs were washed by centrifugation with chloroform/ethanol mixtures at 4400 rpm for 5 min. Subsequent addition to

choroform followed by centrifugation were carried out. The black precipitate can be stored in pure ethanol, methanol, deionized water, or dry under vacuum. The average diameter of the synthesized NPs was 3.4 ± 0.7 nm.

Synthesis of ZnO nanoparticles (NPs): ZnO nanoparticles were synthesized as previously reported.[52] Briefly, plates were synthesized by dissolving 5.5 g $Zn(Ac)_2 \cdot 2H_2O$ in 100 mL anhydrous methanol and refluxed for 1 h, followed by addition of 1 g KOH dissolved in 10 mL deionized water and refluxed for 14 h. Sphere synthesis was similar but the KOH was dissolved in anhydrous methanol rather than water. Pyramids were synthesized by first mixing 0.2 g KOH with the 5.5 g $Zn(Ac)_2 \cdot 2H_2O$ followed by addition of anhydrous methanol and refluxed for 48 h.

Assembly of FeS_2/Protease and ZnO/protease SPs: Typically, 28 nmols of protease aqueous solution (60 µl) were added to the FeS_2 NPs (1.68 nmols) or ZnO NPs dispersion (0.1 mg in 1 mL of water pH 11.0), the pH was adjusted by the addition of 0.1M NaOH and the mix was stored for 72 h. The assembly medium contained desired concentrations (0.5, 1.0, 2.0 and 5.0 M) of NaCl, or it was stored at different temperatures (4, 20, 35, 55, 70 °C). Typically, samples for TEM/SEM studies were diluted about 10 times before imaging. Prior to characterization the excess protein from dispersion was removed and the SPs were redispersed in 1 ml of water at pH 11. The final ratio between FeS_2 NPs and protease was determined by UV-Vis spectroscopy to be 1:3.

CdTe NPs and CdTe Supraparticles: CdTe NPs stabilized by 2-(dimethylamino) ethanetiol (DMAET) was prepared as described in the literature.[53] A 1 mL dispersion of CdTe NPs (pH 5.5) was combined with 20 µL of 300 µM CytC (pH 7.0) for 72 h at 4 C, followed by the addition of

20 µL of FADH (pH 7.0), and stored for 24 h to form the CdTe/CytC/FADH SPs. The resulting assembly was characterized using transmission electron microscopy (TEM), ultraviolet-visible spectroscopy (UV), circular dichroism (CD), and dynamic light scattering (DLS).

Catalytic assay for protease activity: Aliquots of SPs dispersion (1.0 ml) were added to casein solution (5 mL; 6.5 mg/mL) in a desired pH medium (7.5) and kept at specific temperatures (37) for 10 min. The reaction was stopped by addition of trichloroacetic acid (5mL), incubed for 30 min and filtered (0.45 µm polyethersulfone syringe filter). Subsequently, Folin & Ciocalateus Phenol (1 mL) was mix to the filtered (2mL), and then the free tyrosine, released from casein digest process, produce a blue colored chromophore which was measured as a absorbance value at 660 nm on UV-Vis.

Statistical Methods: Error bars in all experiments are calculated based on standard deviation of experimental values obtained in multiple (at least three) measurements following an identical experimental procedure outlined above.

Simulation Model and Method

In our coarse-grained model used for the phase diagram (**Figure 2-4c-e**), the pairwise interaction between the nanoparticles and protein particles is represented by:

$$U(r) = 4\epsilon\left[\left(\frac{\sigma}{r-\Delta}\right)^{12} - \left(\frac{\sigma}{r-\Delta}\right)^{6}\right] + A\exp[-\kappa r] \qquad (2\text{-}1)$$

,

where the first term is the shifted Lennard-Jones 12-6 potential used to model the excluded volume and short-ranged attraction between two particles i and j with different diameters, and the second term is the Yukawa potential used to capture the screened Coulombic potential in an ionic solution. Here r is the center-to-center distance between two particles, and Δ is the shift to the center-to-center distance: $\Delta = (\sigma_i + \sigma_j)/2 - \sigma$. For the LJ potential, ε and σ are the attraction strength and length scale, respectively. Meanwhile, for the Yukawa potential, A and κ are the repulsion strength and inverse screening length, respectively. A, which is in energy unit, is proportional to the particle charges and inversely proportional to the relative permittivity of the solution. κ is proportional to the ionic strength of the solution: increasing the ionic strength decreases the screening length, thus increasing κ. The inverse screening length is $\kappa = 0.1/\sigma$ unless otherwise stated. The attraction strengths between protein-NP, ε_{P-NP}, and protein-protein particles, ε_{P-P}, are varied independently, whereas that between the NPs is fixed. Solvent molecules and counterions are incorporated implicitly using interaction parameters and the thermostat.

For each state point (ε_{P-NP}, ε_{P-P}), the simulated system consists of N particles, and was equilibrated in the canonical ensemble (i.e., at constant volume and temperature) using the Langevin thermostat. At each time step, the thermostat exerts on each particle random and viscous forces to mimic the coupling between the system with a heat bath at the set temperature. The dimensionless temperature is chosen as $T^* = \frac{k_B T}{\varepsilon} = 1$, where $\varepsilon = \varepsilon_{NP-NP}$. The timestep used for time integration is $\Delta t = 0.005\tau$, where the time unit is defined as $\tau = \sigma\sqrt{m/\varepsilon}$, where the unit mass, m, is the NP mass. We considered different system sizes, i.e., the total number of NPs and protein particles, N = 2048, 16000 and 55296 to ensure that the overall shape of the assembled SPs is not biased by the system size and that our results are not biased by initial configurations. Our simulations were performed using LAMMPS software package[54] with GPU acceleration[55].

To estimate the boundaries between the assembled structures in **Figure 2-4c**, we performed parallel tempering simulations, where we simulate 16 replicas concurrently, each with a temperature $0.7 < T < 1.3$ with incremental of $\Delta T = 0.1$. Swaps in the temperature of the replicas are periodically attempted every 10000 timesteps and accepted with the standard Metropolis criterion used for parallel tempering. By doing so, we can detect the transitions between segregation and aggregation, and between NP-protein aggregation and protein-only aggregates (i.e., protein-NP phase separation). The system size in the parallel tempering simulations is N =

2048. Similarly, for **Figure 2-4f**, we also performed parallel tempering simulations for 16 temperature values. The goal here is to equilibrate the assembled SP formed with strong attraction strengths between the NPs and proteins using configurations accessible at lower attraction strengths.

2.4 Results and Discussion

Supraparticle Formation: An overview of hybrid SP formation from NPs (FeS_2, CdTe, ZnO) and proteins (protease, CytC, FADH) is presented in **Figure 2-1**. The selection of FeS2 and ZnO NPs was dictated by a number of advantages, such as biocompatibility, low cost, easy preparation method, and high stability. Protein selection was determined by usefulness in applications and chemical properties. Proteases are mostly utilized for the hydrolysis of peptide bonds,[56] whereas CytC is a well-known electron transport protein[57], and FADH is responsible for reducing CO_2 to formic acid[58]. None of these proteins show any tendency to self-assemble on their own under assembly conditions. However, CdTe NPs are known to self-assemble into nanosheets when in solution[59] and FeS_2 NPs has shown a tendency to aggregate into nanosheets and nanowires.[51] The successful formation of hybrid SPs was achieved by judiciously tuning the surface properties, such as the charge and solution pH of both NPs and proteins (**Table 2-2**).

The structure and composition of SPs were investigated using different molar ratios of NPs and protein. For example, for FeS2 and protease, when using a 1:1 ratio, or when the NP concentration was greater than the protein concentration, macroscale aggregates were observed instead of separate SPs (**Figure 2-7a-c**). When the protein was the prevailing component, the aggregates became less dense (**Figure 2-7d-e**), and the tendency to form SPs gradually emerged when the initial molar ratio was 1:16 (NP: protease) (**Figure 2-7f-g**). Note that the resulting molar ratio between NPs and protease in resulting SPs was 1:3 (**Figure 2-8**). The intermediate stages of the self-assembly process were monitored by transmission electron microscopy (TEM) from 2 h

to 72 h of assembly (**Figure 2-9**) and (DLS). Both techniques show that the size and intensity of aggregates progressively decreased with the formation of SPs. Thereby, and after 72 h of assembly, only one peak at approximately 141 nm was observed (**Figure 2-10**).

Investigation by electron microscopy show defined size and shape representations of individual NPs (**Figure 2-2a, f, k, Figure 2-11a, c**) and SPs, with all protein/NP combinations resulting in near spherical SP assemblies. FeS_2 and ZnO NP dispersions at pH 11 were mixed with aqueous protease at pH 7 and within 72 h, a stable FeS_2 or ZnO NP/protease SP dispersion was spontaneously formed. Spherical SPs with a narrow size distribution was determined by scanning electron microscopy (SEM) and TEM for FeS_2/protease (**Figure 2-2b-c**). Irrespective of individual ZnO NP shapes (pyramid, plates, and spheres), resulting SP assemblies of ZnO/protease were also near-spherical (**Figure 2-2l-m, Figure 2-11b, d)**, which was somewhat surprising because the interactions of Zn nanoplatelets and nanopyramids are expected to be more anisotropic than those of nanospheres. CdTe NPs in pH 5.5 were mixed with CytC at pH 7, stored at 4 C for 72 h, followed by addition of FADH at pH 7 and within 24 h final SPs are formed. The spherical shape and size of assembled SPs were confirmed by TEM (90 ± 10 nm) and SEM (**Figure 2-2g-h**). Overall, the size of CdTe/CytC/FADH SPs increased 23 nm compared to CdTe/CytC SPs, indicating that indeed, FADH is incorporated into the final SP (**Figure 2-12**). TEM shows monodispersed spherical SPs for all NP/protein combination regardless of shape, suggesting that formation of spherical terminal assemblies is thermodynamically stable. It is important to highlight that the presence of proteins promotes the assembly of SP rather than FeS2 aggregates or CdTe sheets. DLS was also performed to confirm that SP assemblies occur in solution and is not a result of drying (**Table 2-1**). The difference observed between d_{TEM} and d_{DLS} can be associated to the removal of water molecules incorporated in the SPs, a process commonly observed in many

proteins and their assemblies.[60] A notable difference is observed in SP sizes (**Figure 2-2d, i, n**), which can be correlated to the size of constituent NPs. Both FeS_2 NP (d = 4.7±0.6 nm, h = 1.5± 0.1 nm) and ZnO pyramids (ZnOpy) (*base* = 15 ± 1.8 nm, *side* = 18 ± 3 nm) were assembled with protease; however, as seen in Table 1, ZnOpy/protease SPs are approximately 20 nm larger, corresponding with the bigger ZnOpy NPs. The NP size dependence was explored further with FeS_2/protease assemblies, showing that the diameter of SPs increases monotonously with the diameter of NPs (**Table 2-3; Figure 2-13**). This dependence may be attributed to an increase of surface area available for protease interaction with the surface of FeS_2.

To confirm protein incorporation in SPs, CD spectra was obtained and shown for all SPs (**Figure 2-2e, j, o** and **Figure 2-14**). After formation, all SP assemblies were washed to ensure the removal of excess free protein that may contribute to the CD signal. There was no CD contribution from NPs (**Figure 2-2e, j, o);** therefore, any CD spectra observed should be attributed to the proteins. As seen in **Figure 2-2e**, the CD spectra of protease (red) and 1:3 mixture of FeS_2/protease SPs (blue) have very similar curve shape. The negative peak at 207 nm matches that of the CD spectra of free tyrosine and is equivalent to a mixture of β-sheet and random coil conformation. Importantly, the CD spectra confirms that the folded secondary structures of all proteins were largely preserved. The slight red shift indicates some conformational change in the protein globules[61]

Similar tendencies are shown for ZnO and CdTe assemblies. For brevity, the remaining part of this paper will focus on the FeS_2/protease SPs assemblies expecting that the properties of the FeS_2/protease SPs are transferable to other assemblies discussed above.

Spectroscopic studies were performed to investigate whether the protein structures in the FeS2 assemblies were affected by the assembly process. Absorbance spectra of SPs dispersed in

water at pH 11 show a band for protease at 283 nm, associated to the π–π* transition in the tryptophan and tyrosine amino acid residues, and a broad featureless shoulder with a maximum centered at 350 nm, assigned to the FeS2 NPs. No shift in protease absorbance band was observed, which indicates that the proteins retain their conformation within the SPs (**Figure 2-15**). The fluorescence spectra of SPs at different temperatures display a maximum at 353 nm, similar to that of native protease, again revealing that the protein in the SPs does not suffer denaturation, as a typical spectrum of unfolded proteins would exhibit either a spectral shift in the peak fluorescence or a peak splitting.[62].

High-resolution TEM (HRTEM) of FeS2/protease SPs shows the electron-transparent and electron-dense areas (**Figure 2-3a**) with the dark regions corresponding to FeS2 NPs and the light areas to the protease-rich regions. For individual NPs inside the SP, a lattice spacing of 0.26 nm was observed, which is the (200) lattice plane of the cubic pyrite phase of FeS2 (**Figure 2-3b**).[51] Scanning TEM was utilized to show the interconnectivity between NPs and proteins in the SPs (**Figure 2-3c-d**). In these high-angle annular dark field images (HAADF), the darker regions are representative of the proteins, whereas the brighter areas represent FeS2 NPs. It is evident that within the SPs the NPs and proteins are highly interconnected, allowing for optimal immobilization and encapsulation of the proteins.

The attractive interactions in the assembly of NPs and proteins are represented by vdW forces, hydrogen, coordination, and supramolecular bonds. The repulsive interactions are primarily electrostatic in nature. Despite conceptual limitations for nanoscale particles related to nonadditivity of interparticle interactions at the nanoscale,[63] carrying out the Derjaguin, Ladau, Verwey, and Overbeek (DLVO) calculations are instructive for the first-order approximation for interaction potentials between FeS2 NPs and proteases. As such, one can note a repulsive

maximum (V ≈ 0.3 kBT) for the pair-wise NP/protein interactions, which may be easily overcome by Brownian motion. Therefore, initial mixtures of FeS2 NP and the proteases in the aqueous suspension easily self-assemble Figure 2-4. Self-limiting assembly of NPs and protein resulting in hybrid supraparticles. (a) Pair potential between FeS_2 NPs and protease according to DLVO theory (b) ζ-potential values for the assembly of FeS_2 NPs with protease at different time intervals (0, 2, 8, 24, 48, 60 and 72 h). Error bars indicate the standard deviation values from multiple measurements. (c) Phase diagram obtained from computer simulation. Circular dots represent the simulated state points in our study. The regimes are sketched based on the obtained structures at the state points. Here $\varepsilon_{P\text{-}NP}$ and $\varepsilon_{P\text{-}P}$ are the attraction strength of the protein-NP and protein-protein interactions, respectively. (d) Representative snapshot of an assembled SP containing both NPs (blue) and proteins (yellow). (e) Pair correlation functions between protein-protein and NP-NP in (d). (f) Cross-section of a SP formed by NPs (inset) and protein particles represented by discoids and spheres, respectively Figure 2-4. Self-limiting assembly of NPs and protein resulting in hybrid supraparticles. (a) Pair potential between FeS_2 NPs and protease according to DLVO theory (b) ζ-potential values for the assembly of FeS_2 NPs with protease at different time intervals (0, 2, 8, 24, 48, 60 and 72 h). Error bars indicate the standard deviation values from multiple measurements. (c) Phase diagram obtained from computer simulation. Circular dots represent the simulated state points in our study. The regimes are sketched based on the obtained structures at the state points. Here $\varepsilon_{P\text{-}NP}$ and $\varepsilon_{P\text{-}P}$ are the attraction strength of the protein-NP and protein-protein interactions, respectively. (d) Representative snapshot of an assembled SP containing both NPs (blue) and proteins (yellow). (e) Pair correlation functions between protein-protein and NP-NP in (d). (f) Cross-section of a SP formed by NPs (inset) and protein particles represented by discoids and spheres, respectively (**Figure 2-4a**). The changes in the electrokinetic potential (ζ) over the courses

of the SP formation reflect the self-limited growth of these SPs complex particles. Prior to the assembly, the ζ value of the FeS2 NPs and the proteases were measured to be −48.1 and −10.8 mV, respectively (**Figure 2-16**). The ζ value of the NP/protease dispersion was −32.4 mV at the initial stage and increased to −17.6 mV after 8 h. Further increase in the assembly time is accompanied by continued increase in the overall zeta-potential, indicating continued growth of the SPs. Within 72 h, ζ reached a constant value of −15 mV, indicating that an equilibrium or a steady state was achieved (**Figure 2-4b)**. Indeed, the growth of the SPs terminated when its diameter reached 141 ± 14.2 nm, as determined by DLS. At that stage, high zeta-potential and size enlargement were expected to exert further attractive interactions. However, stronger and longer-ranged electrostatic interaction concomitantly increase with size until its repulsive potential enforces a barrier for further self-assembly.

Computer simulations were performed to further investigate how the NPs and proteins assemble into SPs. In this study, we focus mainly on the local packing of the SPs; the self-limiting behavior of the assembly process that gives rise to SPs with similar sizes can be explained by the renormalized repulsion between the building blocks as in our previous studies.[4,64] The NPs and proteins are modeled as spherical particles with a size ratio of 1:1.7, similar to the relative average sizes of FeS2 and protease. The effective interaction between the NPs and protease is modeled by the empirical Lennard-Jones and Yukawa potentials (**Simulation Method**). The former captures excluded volume/steric interactions and short-ranged attractions between the building blocks, for example, induced by vdW forces and hydrogen bonding. The latter captures the repulsion between the particles induced by their screened electrostatic interaction in ionic solutions. The use and parametrization of these potentials were validated based on multiple prior studies of CdTe NPs by the groups of Kotov, Glotzer, and coworkers. We have simulated a 1:3 molar ratio mixture of NPs

and proteins at different attraction strengths between the NPs and protease, $\varepsilon_{P/NP}$, and between protease, $\varepsilon_{P/P}$, to explore the conditions at which the assembly occurs. Parallel tempering simulations were also performed to identify the morphology of the SPs and the local packing of the NPs and proteins within individual SPs.

The simulated state points for the 1:3 NP/protein mixture are summarized in **Figure 2-4c**, where the region of NP/protein aggregation corresponds to the conditions observed in our experiments. Our simulations indicate that the effective NP/protein attraction should be sufficiently stronger than the attraction between the proteins to lead to the formation of the SPs as experimentally observed. The transition where NPs and proteins start to aggregate into SPs depends on the relative attraction strengths, $\varepsilon P/NP$ and $\varepsilon P/P$. At the transition point, for example, $\varepsilon P/NP/kBT = 5.0$ and $\varepsilon P/P/kBT = 4.0$, the SPs are in equilibrium with the proteins in solution (**Figure 2-4d**), as observed in the experiment. The simulated assembled SPs have an almost spherical shape, within which the NPs and proteins pack randomly, as revealed by the pair correlation functions (**Figure 2-4e**). To examine the role of the shapes of the NPs on the local packing of the building blocks within a SP and the overall geometry of the SPs, we modeled individual NPs as rigid bodies each composed of 207 beads rigidly linked together (**Figure 2-4f, inset**). The model NPs have shape and aspect ratio similar to the FeS2 NPs in experiment. The proteins are modeled as spheres with a size similar to the NP. To facilitate the formation of a spherical aggregate, we first equilibrated the 1:3 mixture of the NPs and protein in a spherical cavity, and subsequently removed the cavity. Parallel tempering simulations were then performed to explore the possible packing inside the SP and the SP geometry that are energetically favored (**Simulation Method**). **Figure 2-4f** shows the cross section of a representative SP after equilibration at sufficiently strong NP/protein attractions displaying random packing within SPs.

We further examined the formation of SPs when prepared in different solvents, ionic strengths, and temperatures. Methanol and ethanol media resulted in elongation of the SP shape; the size of SPs prepared in isopropanol, ethanol, and methanol were 188 ± 16, 210 ± 21, and 245 ± 23 nm, respectively (**Figure 2-5a-d**). Meanwhile, the increase of temperature led to a slight increase in the average SP diameter (**Figure 2-5e-h**; **Table 2-4**), and may be associated to a slight decrease in van der Waals resulting in SPs that are not as tightly integrated. Lastly, as the ionic strength was increased, the average size of SPs was increased because of reduced electrostatic screening. However, when the NaCl concentration was greater than 2.0 M, aggregation of the SPs was observed, which was accompanied by reduction in ζ (**Figure 2-5i-l**; **Table 2-5**).

Protein Recovery and Activity

To determine if protease within the SPs maintains its catalytic functionality, an enzyme activity assay was performed. During the assay, casein was degraded by protease via hydrolysis, releasing tyrosine along with other amino acids and peptide fragments. The undigested casein was made insoluble by treatment with trichloroacetic acid; subsequently, Folin's reagent reacted with free tyrosine to produce a blue-colored chromophore. The UV−Vis peak intensity of free tyrosine was measured at 660 nm to generate a catalytic activity profile **(Figure 2-17**).[65] Protease was released from the SPs by controlling the environmental conditions and ultimately displacing the charge interactions, causing SPs to disassemble. FeS2/protease SPs were introduced into a pH 5.5 solution and after 2 h the formation of large polydisperse aggregates of FeS2 was observed under TEM (**Figure 2-6a**). Similar aggregates of FeS_2 were formed in both neutral and alkaline environments when protease was not present (**Figure 2-18**) indicating the release of protease from SPs. Centrifugation separated the large FeS2 aggregates from the recovered protease in the supernatant.

Supernatant and disassembled SPs were characterized by CD spectroscopy (**Figure 2-6b**), where a change in the spectra for the recovered protease was observed. Although there may be some conformational change in the protein spectra, it is apparent from the results that the active sites on protease were not compromised, and the activity of the recovered protease was comparable to that of native protease at pH 5.5 (**Figure 2-6c**).

To verify the activity of protease within SPs, we assessed the performance of native protease versus protease within SPs at pH 7.5 and 8.5. Over a time period of 60 min, the activity of protease within SPs was identical within the experimental error to the activity of native protease (**Figure 2-19**). When the effect of temperature was explored (**Figure 2-20**), SPs outperform native proteases at lower temperatures of 4 °C and 20 °C, while at 42 °C the native protease activity becomes higher, as the optimal conditions for serine proteases are high temperatures and pH.[66] These results indicate that SPs help maintain or promote the activity of the protein under unfavorable conditions. It also confirms that while we see some conformational changes in CD, the active sites of protease are unchanged and active in SPs, not only when recovered. Therefore, immobilization of proteins via SPs allows for facile recovery and reuse of active enzymes. We also examined the stability of SPs under UV irradiation at 260 and 350 nm. TEM images show that SPs remains intact after 10 min of illumination; however, at 15 min, we observed a deformation in the spherical shape of the SPs, indicating the onset of instability (**Figure 2-21**). Thereby, SPs have limited stability in UV environment.

2.5 Conclusions

Hybrid SPs composed of FeS2, ZnO, and CdTe NPs with protease, CytC, and FADH were self-assembled into monodispersed spherical assemblies despite variation in the shapes of constituent

NPs. SPs are simple to prepare, can be used in a variety of solvents, and remain stable under high ionic strength, and temperature, when native enzymes denature. We have also demonstrated that SPs retain protein activity that may be utilized for their encapsulation for the needs of biotechnology and catalysis.

2.6 Figures and Tables

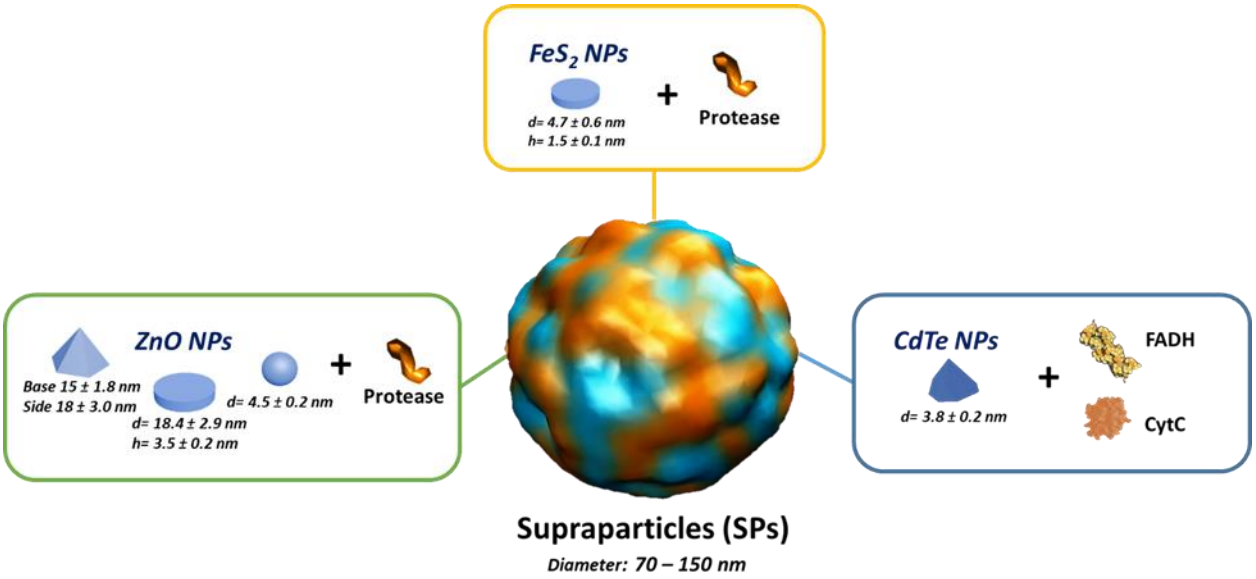

Figure 2-1. Formation of diverse hybrid SPs from inorganic NPs made from FeS_2, ZnO, and CdTe NPs with proteins represented by protease, CytC, and FADH.

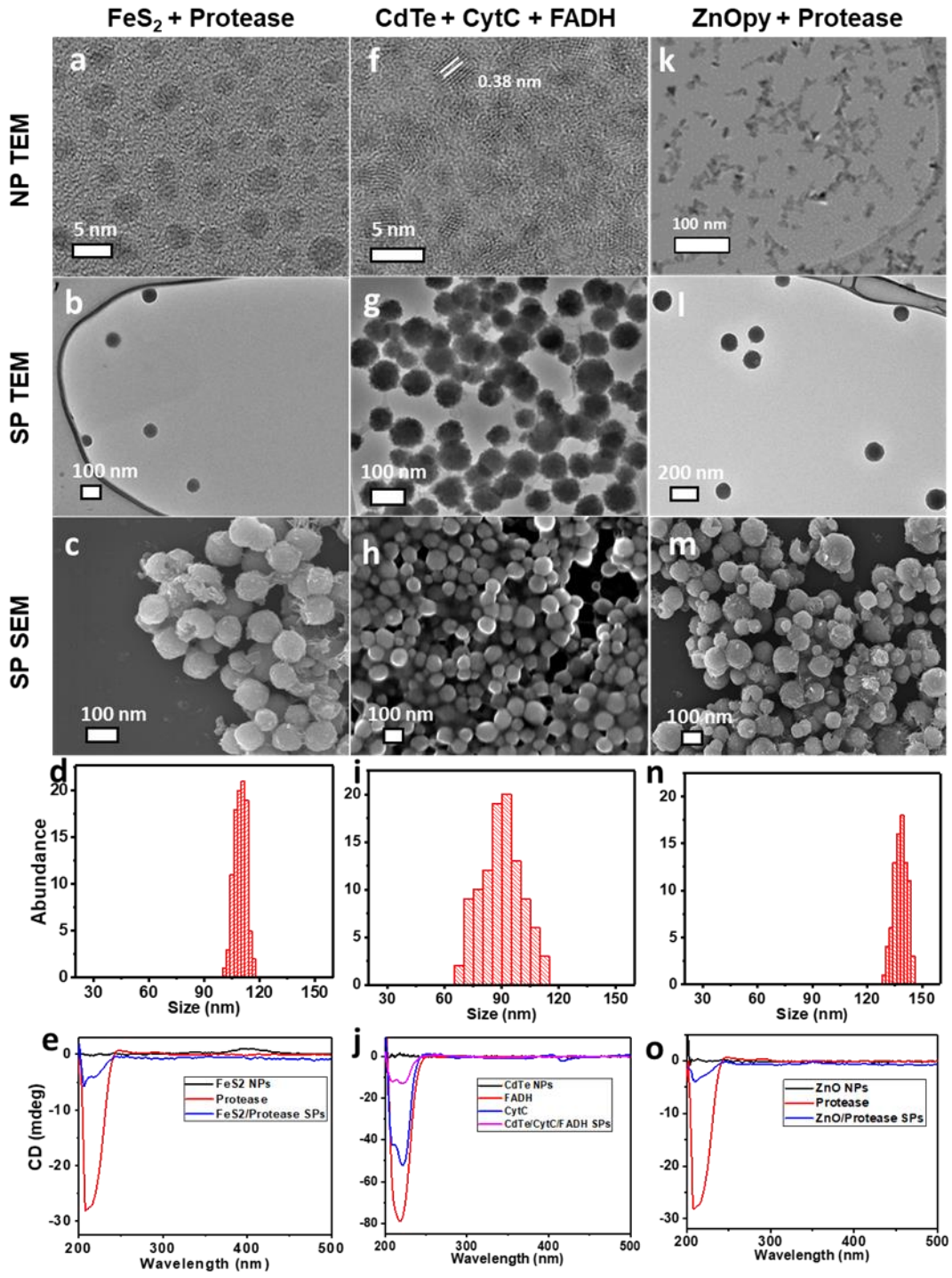

Figure 2-2. Hybrid supraparticles from inorganic nanoparticles and proteins. TEM of (a) FeS_2 NPs, (b) FeS_2/protease SPs, (c) SEM of FeS_2/protease SPs, (d) size distribution of FeS_2 SPs, (e) Circular dichroism (CD) of FeS_2, protease, and FeS_2 SPs. (f-j) show the same order of images for CdTe/CytC/FADH SPs, and (k-o) show the same order for ZnOpyramid/protease SPs.

Table 2-1. SP diameter determined by DLS and TEM

Hybrid SP	Diameter of SPs by DLS d_{DLS}(nm)	Diameter of SPs by TEM d_{TEM}(nm)
FeS_2/Protease	141 ± 14.2	110 ± 3.3
CdTe/CytC	106 ± 6.6	67 ± 11
CdTe/CytC/FADH	125 ± 14.0	90 ± 10
ZnO sphere/Protease	155 ± 19.1	120 ± 10.6
ZnO plate /Protease	157.1 ± 7.3	144 ± 19
ZnO pyramid/Protease	187.5 ± 15.6	139 ± 3.5
Statistic errors were calculated from 100+ measurements on TEM grids and by DLS.		

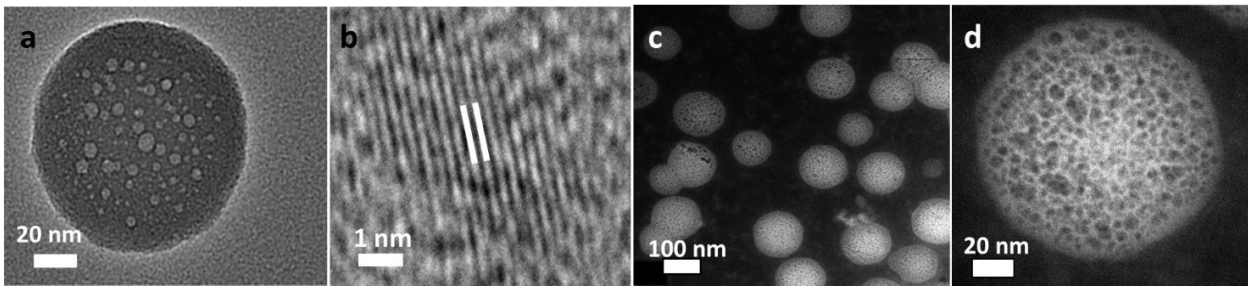

Figure 2-3. Structural characterization of FeS_2/protease SPs. (a) TEM image of individual FeS_2/protease SPs. (b) High resolution transmission electron microscopy (HRTEM) image of individual NP inside a SP in a demonstrating lattice spacing of 0.26 nm that corresponds to (200) of the cubic pyrite phase of FeS_2. (c) STEM-ADF image of FeS_2/protease SPs, (d) STEM-ADF view of single SP.

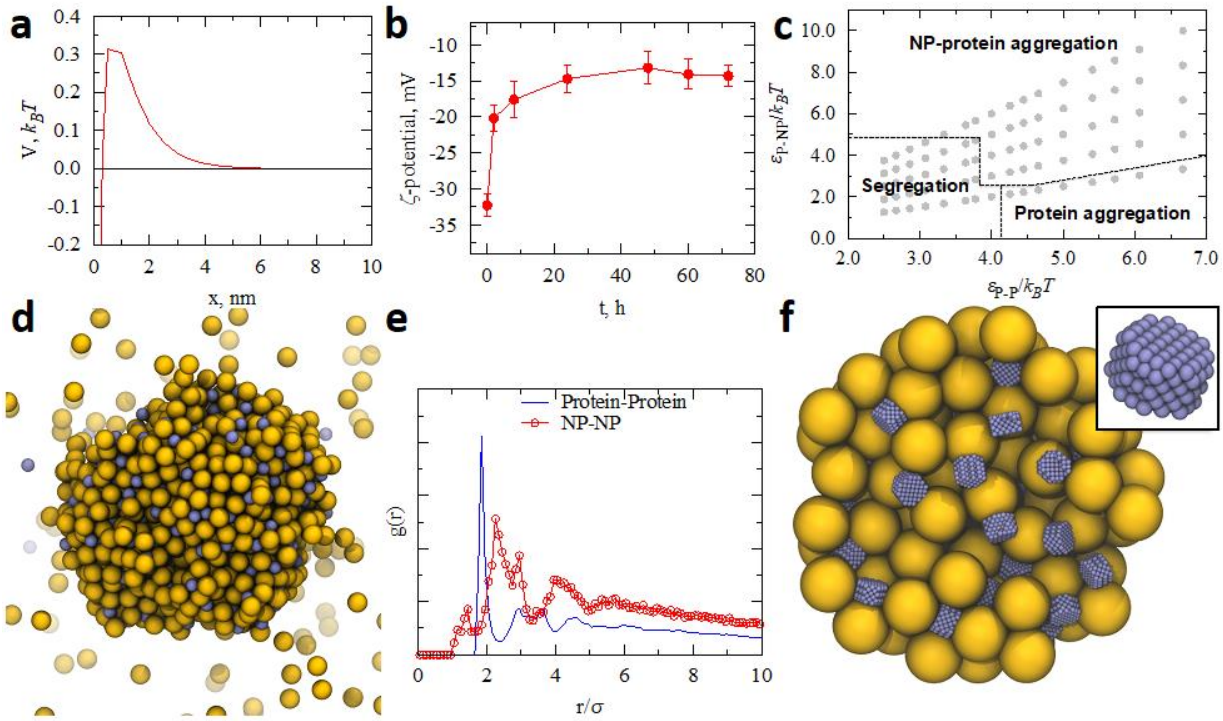

Figure 2-4. Self-limiting assembly of NPs and protein resulting in hybrid supraparticles. (a) Pair potential between FeS_2 NPs and protease according to DLVO theory (b) ζ-potential values for the assembly of FeS_2 NPs with protease at different time intervals (0, 2, 8, 24, 48, 60 and 72 h). Error bars indicate the standard deviation values from multiple measurements. (c) Phase diagram obtained from computer simulation. Circular dots represent the simulated state points in our study. The regimes are sketched based on the obtained structures at the state points. Here $\varepsilon_{P\text{-}NP}$ and $\varepsilon_{P\text{-}P}$ are the attraction strength of the protein-NP and protein-protein interactions, respectively. (d) Representative snapshot of an assembled SP containing both NPs (blue) and proteins (yellow). (e) Pair correlation functions between protein-protein and NP-NP in (d). (f) Cross-section of a SP formed by NPs (inset) and protein particles represented by discoids and spheres, respectively

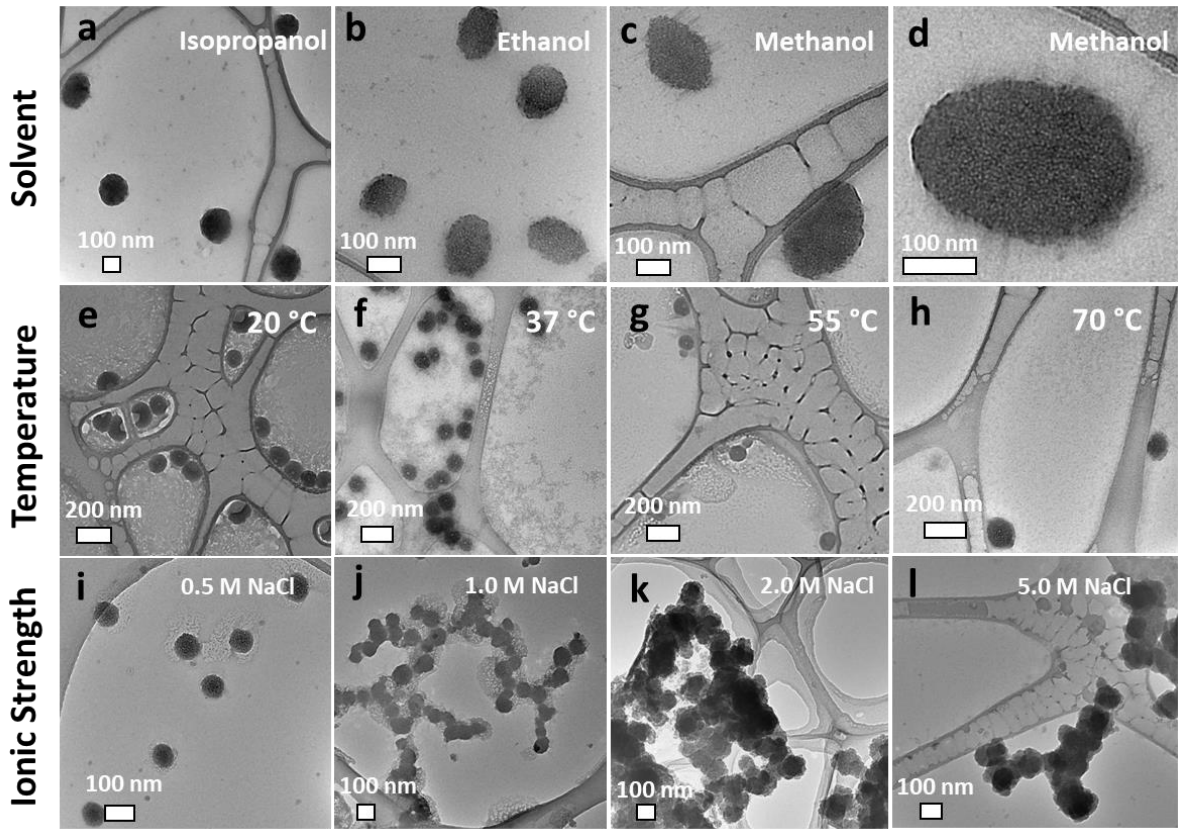

Figure 2-5. Effect of solvent, temperature, and ionic strength on stability of SPs. TEM images of FeS_2/Protease SPs stored at 4°C in (a) isopropanol, (b) ethanol, and (c) methanol (d) closer view of elongation in methanol. TEM images of FeS_2/Protease SPs prepared in aqueous solution at pH 11 and stored at (e) 20°C, (f) 37°C, (g) 55°C, and (h) 70°C. TEM of FeS_2/Protease SPs formed in different concentrations of NaCl (i) 0.5 M, (j) 1.0 M, (k) 2.0 M and (l) 5.0 M. Scale bars are 100 nm (a-d, i-l) and 200 nm (e-h).

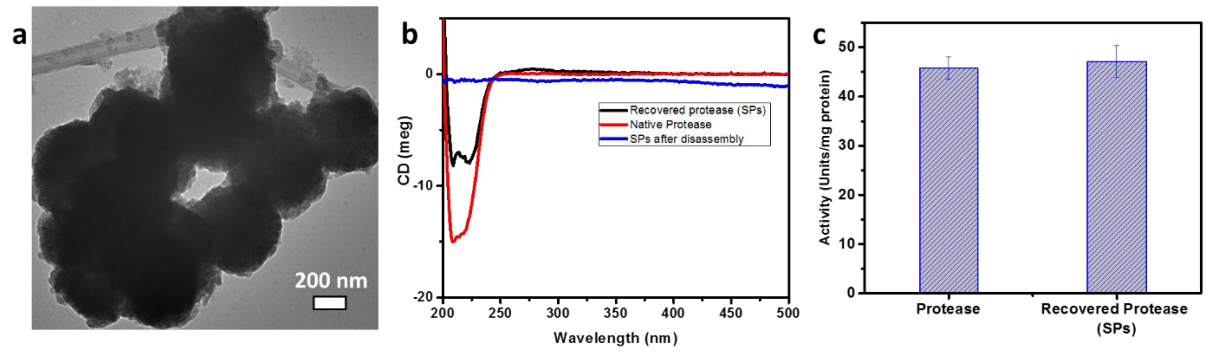

Figure 2-6. Protein recovery and activity. (a) FeS_2 aggregates after SP disassembly, (b) CD data of SPs after disassembly (blue), native protease (red), and protease recovered from SPs (black), and (c) activity of native and recovered protease.

Supplementary Figures:

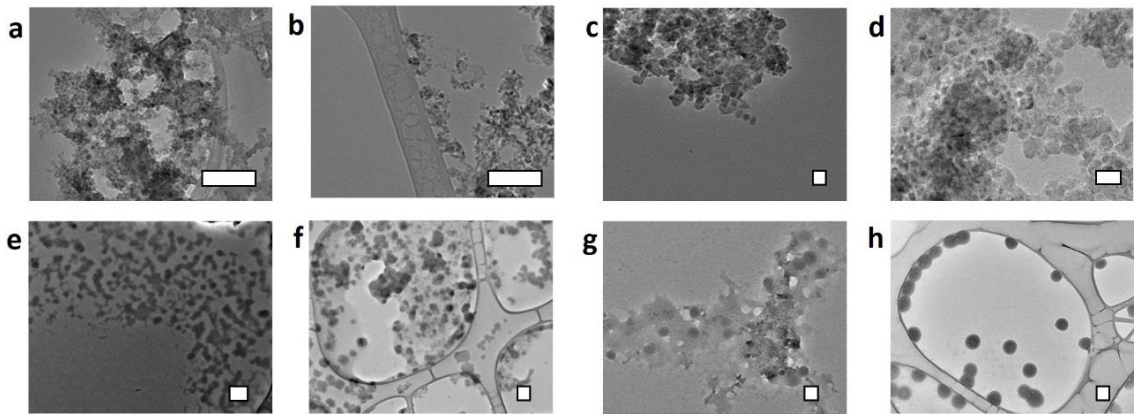

Figure 2-7. Assembly of FeS_2 NPs and protease. Transmission electron microscopy (TEM) images of the mixtures of FeS_2 NPs at pH 11 and protease with a molar ratio of (a)1:1, (b) 2:1, (c) 5:1, (d) 1:2, (e) 1:5, (f) 1:7, (g) 1:10, and (h) 1:16 - before removing the excess of protein. Scale bars are 100 nm (a,b,e-h) and 20 nm (c,d).

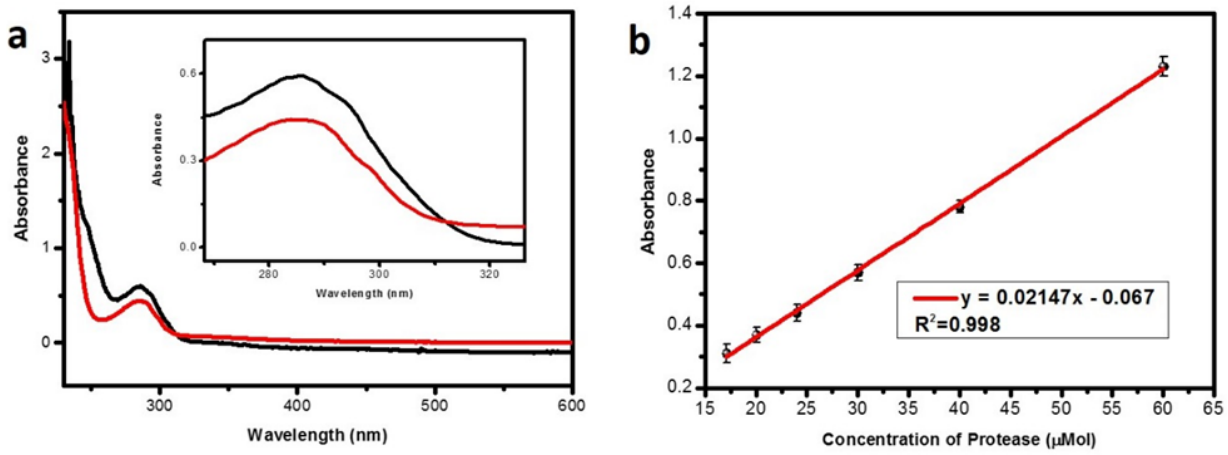

Figure 2-8. Calculation of ratio between FeS_2 NPs and protease in the SPs after removing the protein excess (a) UV-Vis spectrum immediately after mixture of FeS_2 NPs and protease with ratio 1:16 (black), UV-Vis spectrum of supernatant after 72 h of mixture (red). The amount of protein into SPs was calculated from the difference between the initial concentration of protease and the concentration of protease in the supernatant obtained by centrifugation, after 72 h of assembly. The subtraction of protease concentration of red curve from black curve showed only 21.3% of protein initially added were used to form the SPs. Therefore, SPs are formed with 1:3 molar ratio of the FeS_2 NPs/protease. (b**) Standard addition curve of protease used to estimate the loading efficiency of protease into the SPs.**

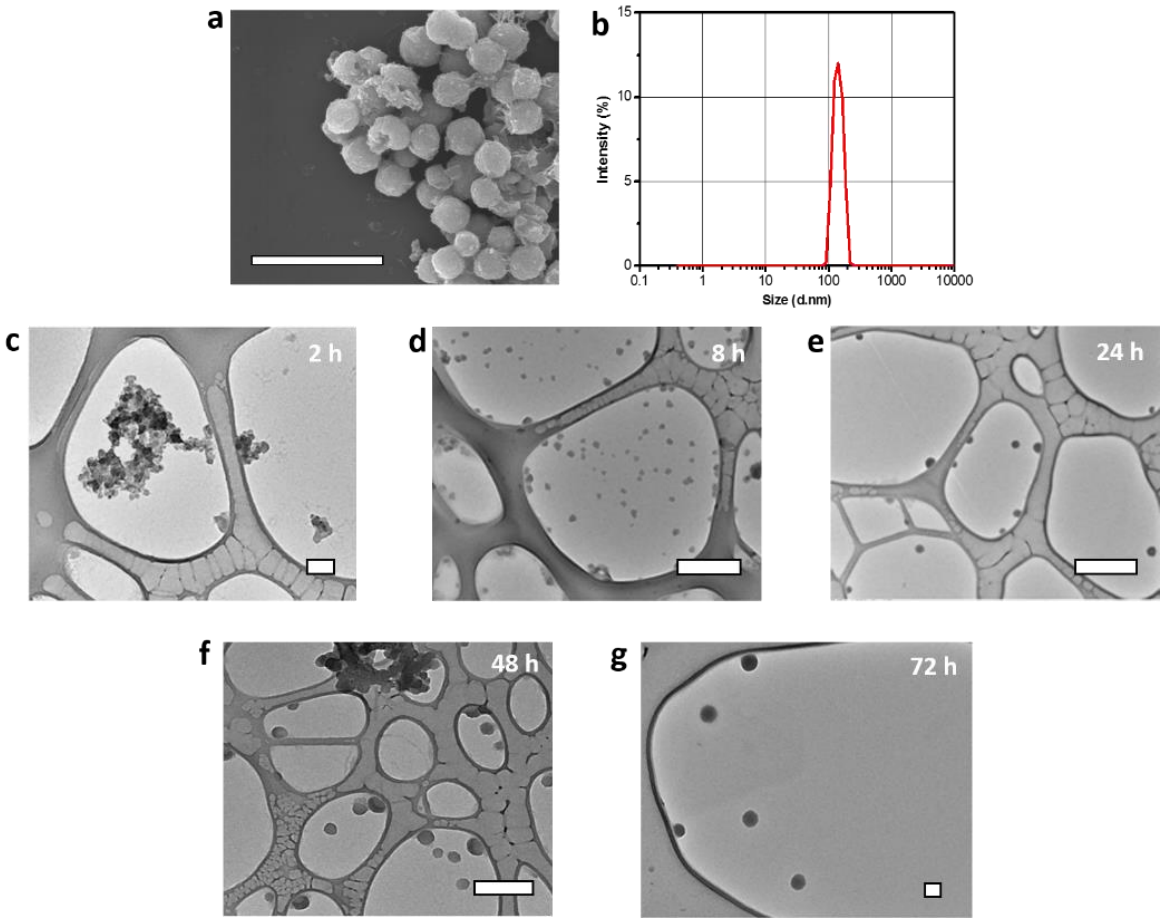

Figure 2-9. **Self-assembly of FeS_2 NPs and protease. (a) Scanning electron microscopy (SEM) image of FeS_2 NP-protease SPs after 72 h of assembly, stored at 4°C. (**b**) Size distribution of the self-assembled SPs by dynamic light scattering (DLS). (**d-g**) TEM study of morphological changes in FeS_2/Protease SPs during the assembly (time interval between 2 h and 72 h). Scale bars are 100 nm (**d,h**) and 500 nm (**a,e,f,g**).**

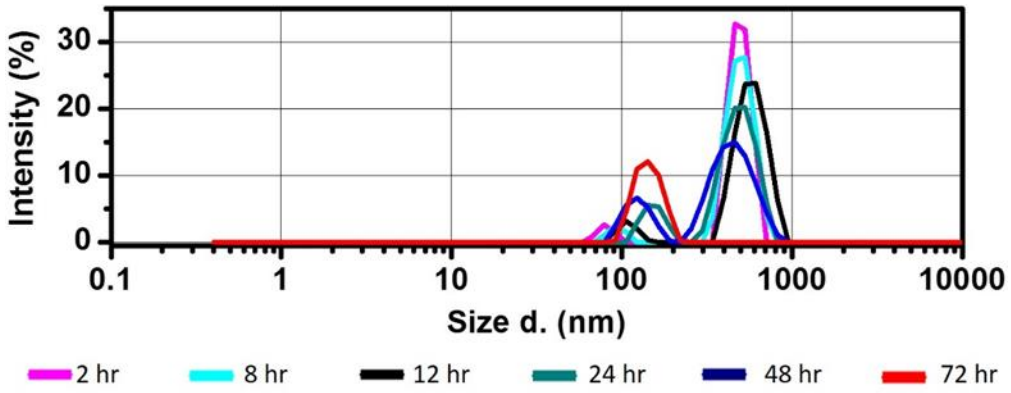

Figure 2-10. **Dynamic light scattering study of the particle size distribution for different times of self-assembly process between FeS_2 and protease. The intermediate stages of the self-organization process shows the appearance of particles with d_{DLS}= 79 ± 8.0, 92 ± 9.6, 108 ± 13.1, 179 ± 12.5, 135 ± 17.4 and 152 ± 13.2 nm at 2, 8, 12, 24, 48, and 72 h, respectively.**

Note 1: The diameter of SPs obtained from DLS curve corroborate with those obtained from SEM/TEM data. The difference between d_{DLS} and d_{TEM} indicates incorporation of water molecules in the SPs, as is observed in many proteins and their assemblies.

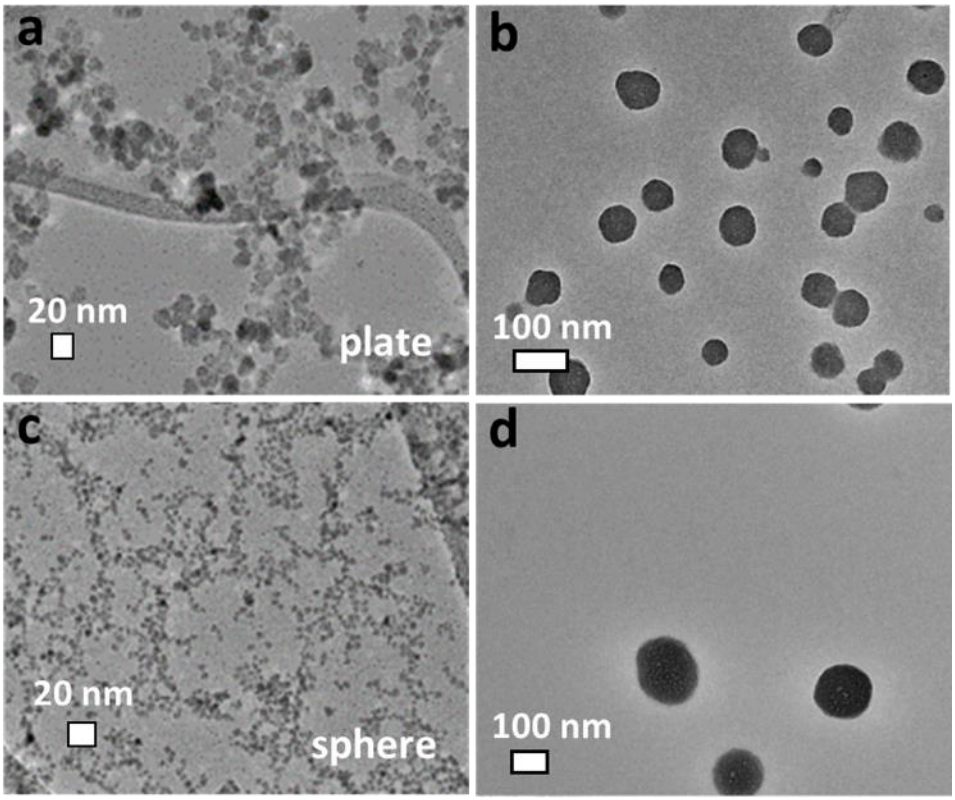

Figure 2-11. TEM of (a) ZnO nanoplates, (b) ZnOpl/protease SPs, (c) ZnO sphere NP, and (d) ZnOsp/protease SP.

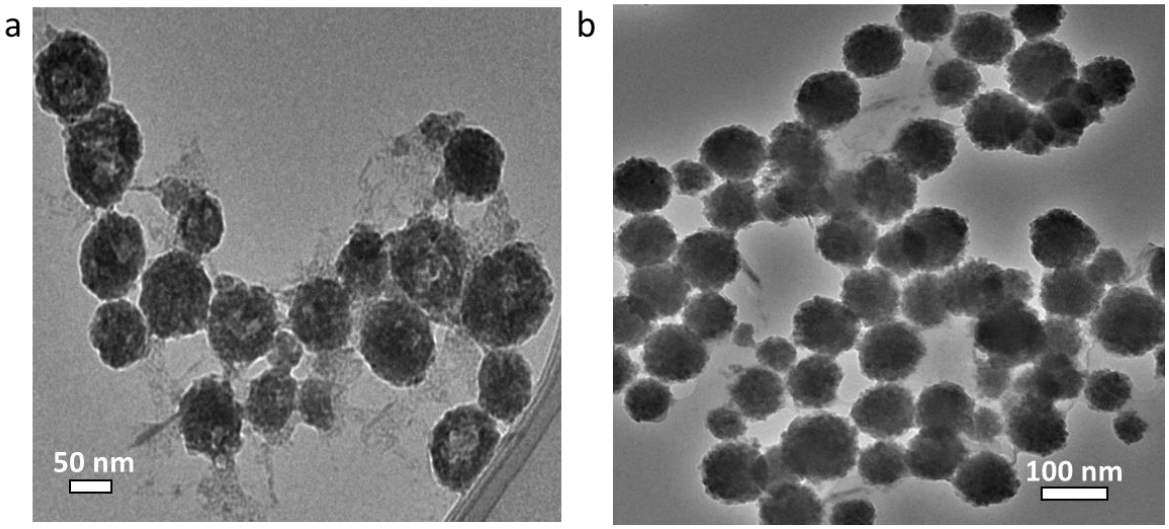

Figure 2-12. CdTe SPs. (a) CdTe/CytC SPs, and (b) CdTe/CytC/FADH SPs.

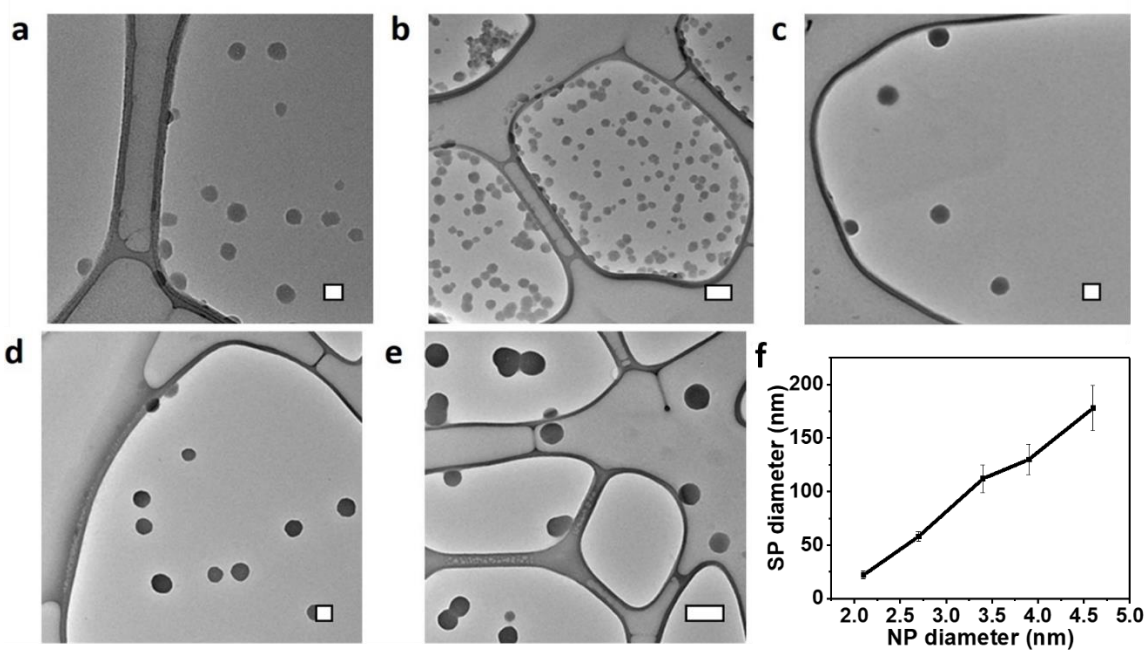

Figure 2-13. Dependence of SP diameter on the NP diameter. Transmission electron microscopy (TEM) images of FeS_2 NPs/protease SPs formed from FeS_2 NPs with diameter of (a) 2.1 ± 1.3, (b) 2.7 ± 0.9, (c) 3.4 ± 0.7, (d) 3.9 ± 1.2, (e) 4.6 ± 0.5 nm, and (f) plot of SP diameter dependence on NP size. Scale bars are 20 nm (a), 50 nm (b), 100 nm (c,d), and 200 nm (e).

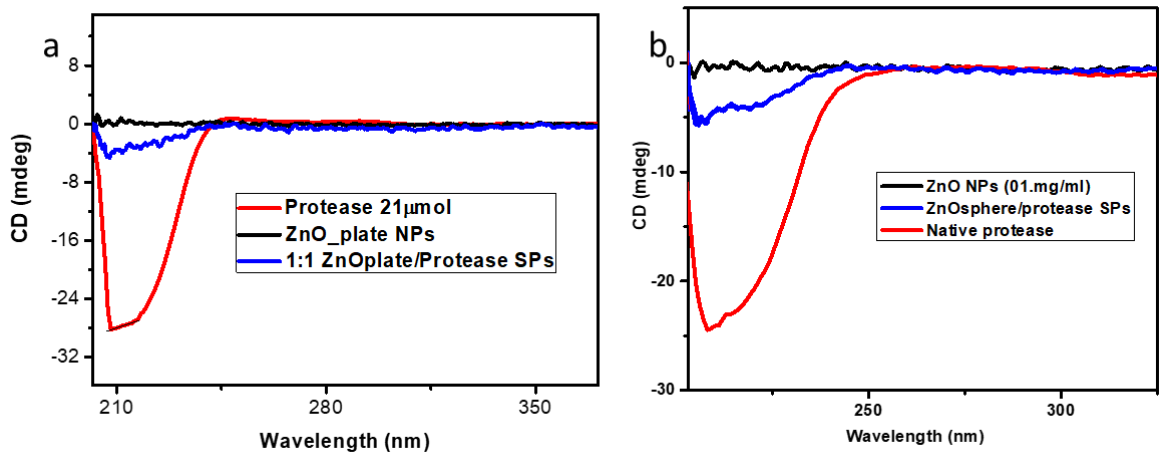

Figure 2-14. Circular dichroism spectra of (a) ZnOplate/protease and (b) ZnO sphere/protease.

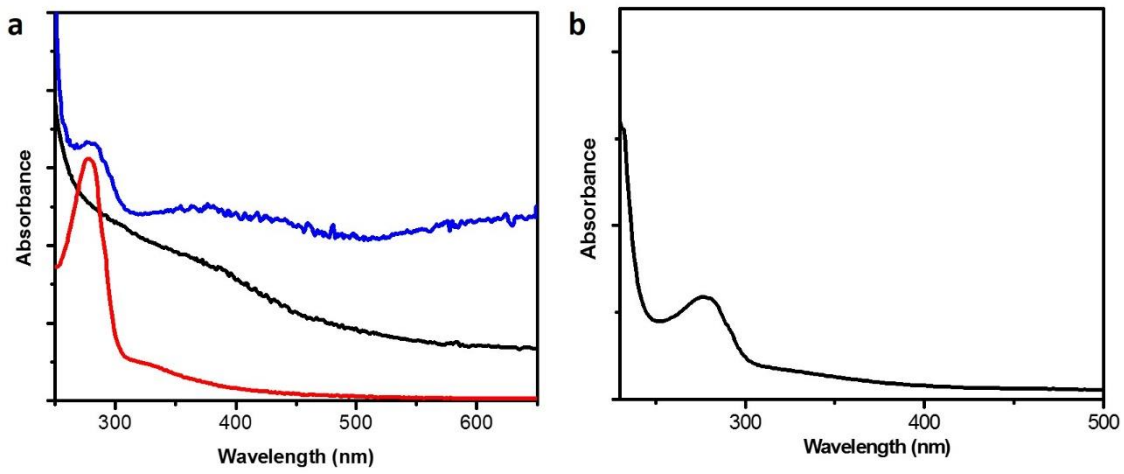

Figure 2-15. Characterization spectroscopy of protease, FeS_2 NPs and FeS_2 NPs/protease SP (a) UV-Vis spectra of protease (red, 28 µM), freely dispersed FeS_2 NPs (black) and SPs (blue, 1:3 FeS_2/Protease, after 72h of assembly). (b) Control experiment: UV-Vis spectrum of a mixture of $FeCl_3$ and protease under the same conditions as in (a). The spectrum of protease in presence of Fe^{2+} is identical to that without it.

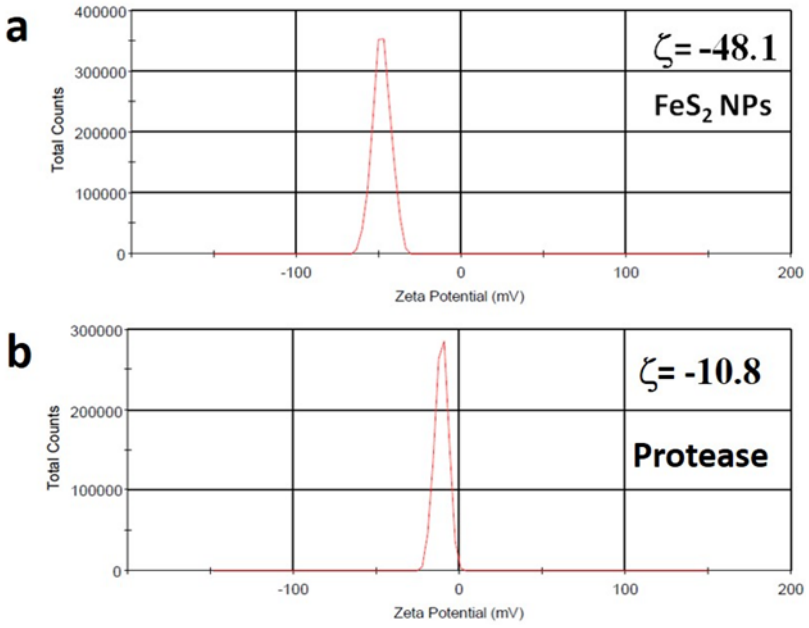

Figure 2-16. Electrokinetic ζ-potential measurements at pH 11 of (a) TGA-FeS_2 NPs, and (b) Protease.

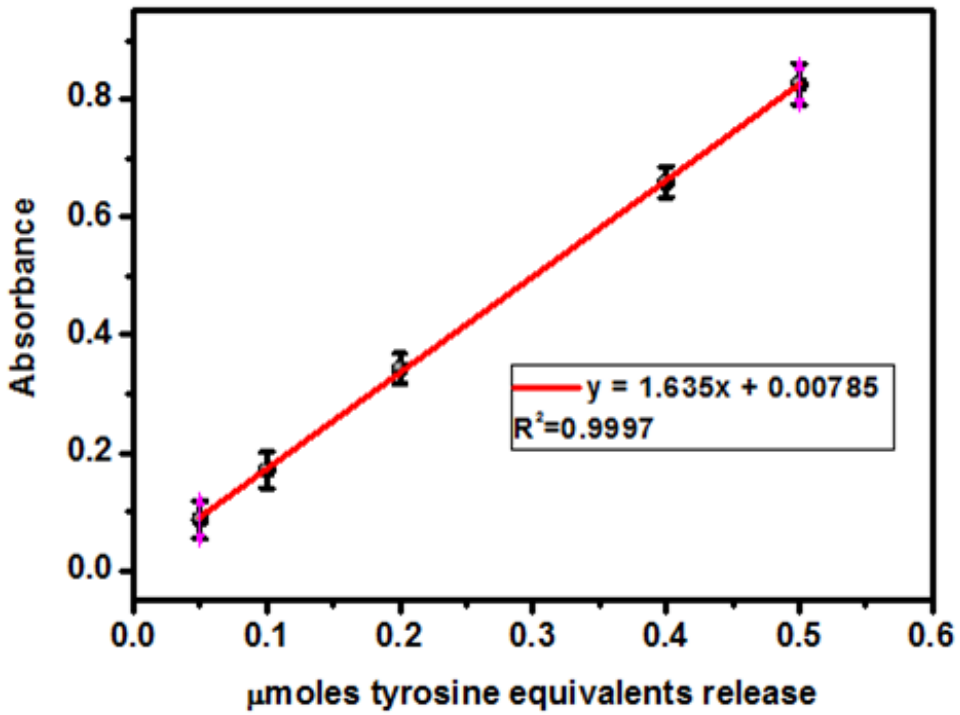

Figure 2-17. Standard analytical curve for UV-vis absorption at 660 nm obtained from different concentrations of tyrosine.

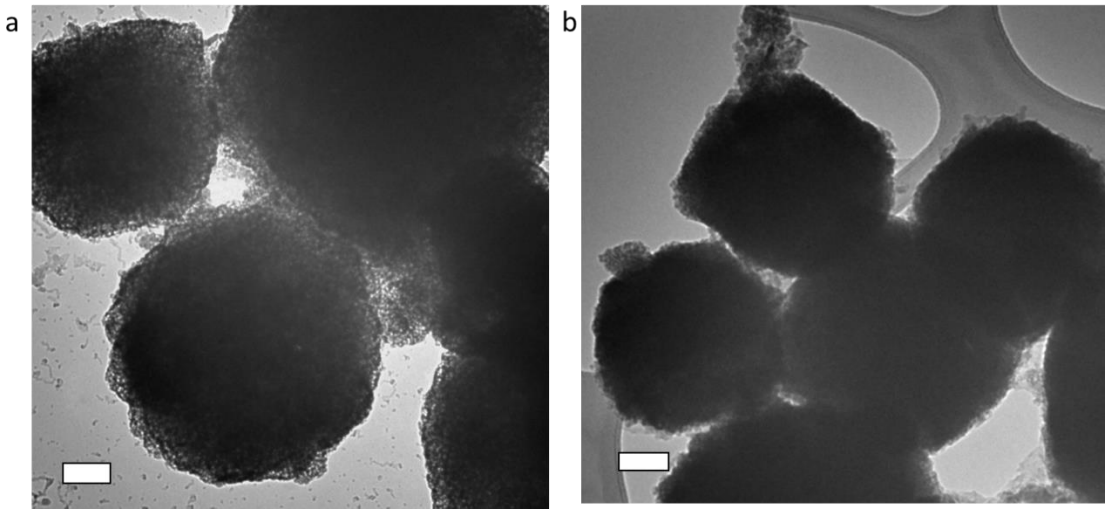

Figure 2-18. FeS_2 particles have a tendency to aggregate into large polydisperse clusters. (a) pH 7.0 and (b) pH 11.0 when alone in solution. Scale bars = 200 nm

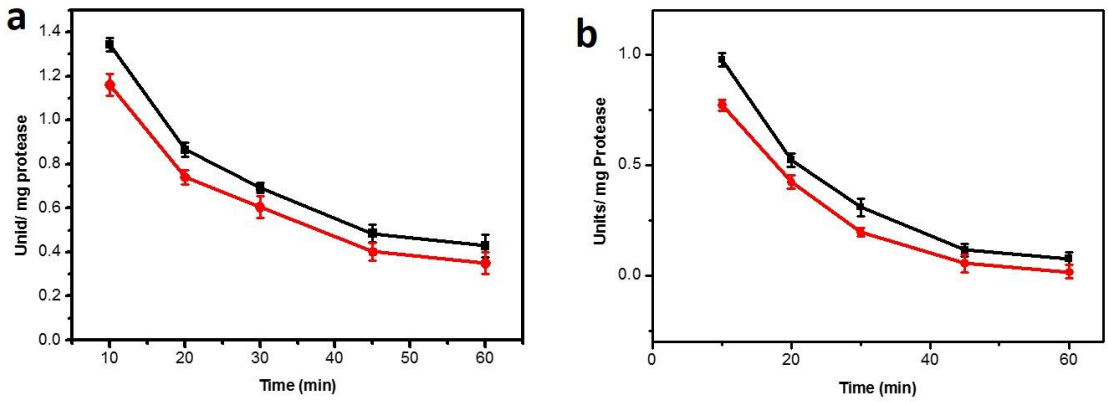

Figure 2-19. Catalytic assay of FeS_2/protease SPs and protease at 37°C. Catalytic assay of FeS_2/protease SPs (red curve) and of protease (black curve) at (a) **pH 7.5 and** (b) **pH 8.5.**

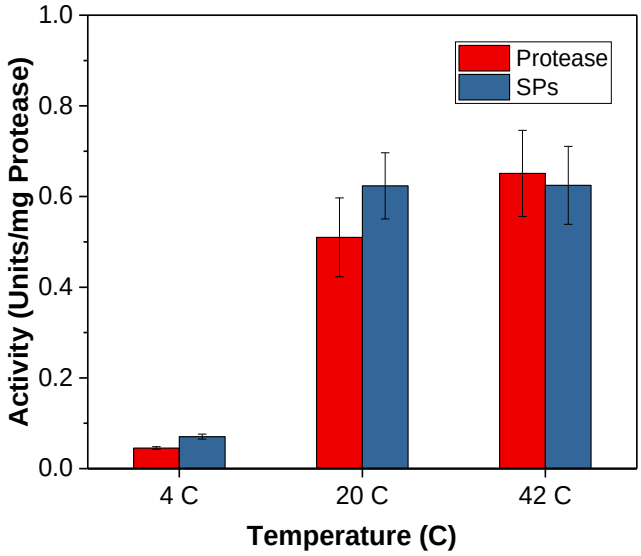

Figure 2-20. Catalytic activity of native protease vs. FeS_2/protease SPs at 4 °C, 20 °C, and 42 °C after 20 minutes of exposure time.

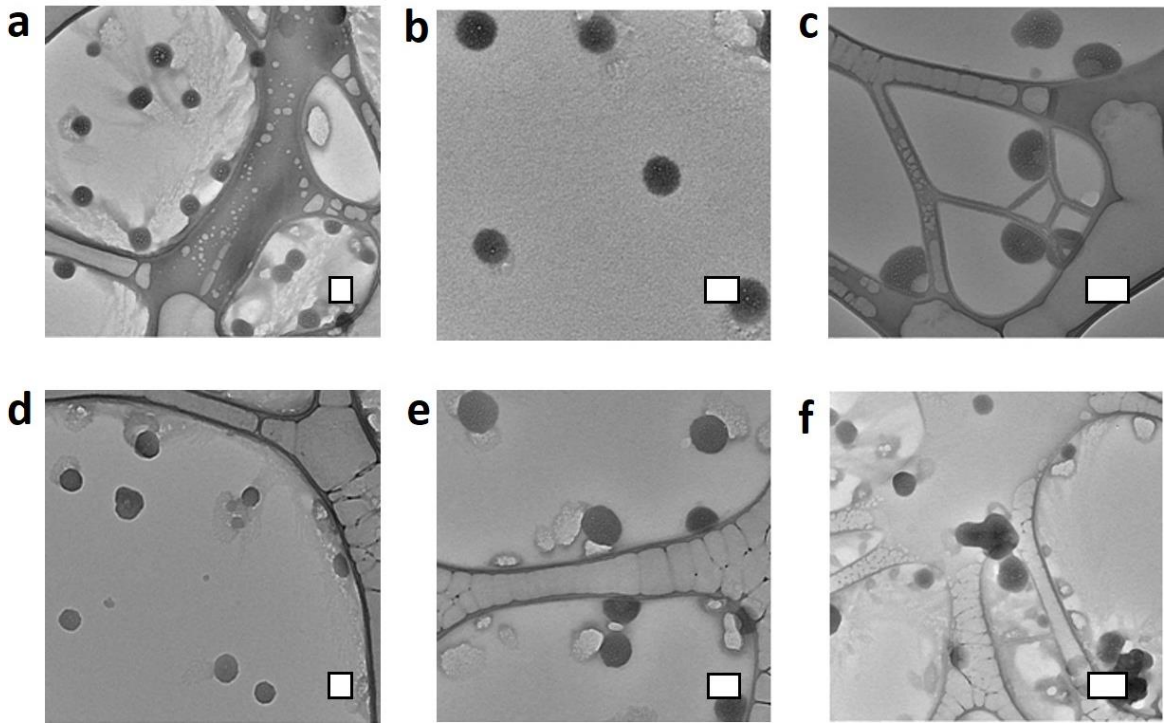

Figure 2-21. Stability of FeS_2/Protease SPs under illumination TEM images of SPs illuminated at (a) 260 nm for 5 min, (b) 260 nm for 10 min, (c) 260 nm for 15 min (d) 350 nm for 5 min, (e) 350 nm for 10 min, and (f) 350 nm for 15 min. All samples were illuminated with slit width for excitation at 20 nm. Scale bars are 100 nm (a,b,d,e) and 200 nm (c,f).

Table 2-2. Zeta potential of all constituents at corresponding solution pH

Hybrid SP	Constituents	Zeta potential (mV)	Isoelectric point	Solution pH
FeS_2/protease	FeS_2 NPs	-48.1		pH 11
	Protease	-10.8	5.5	pH 11
CdTe/CytC/FADH	CdTe	+26		pH 5.5
	CytC	+7.0	11.0	pH 7.0
	FADH	+12.6	7.0	pH 6.5
ZnO/Protease	ZnOpy	-38.6		pH 11
	ZnOsp	-40.2		pH 11
	ZnOpl	-40		pH 11
	Protease	-10.8	5.5	pH 11

Table 2-3. Dependence of SP diameter on the constitutive NP diameter.

Diameter of TGA-FeS_2 NPs (nm)	Diameter of SPs by DLS d_{DLS}(nm)	Diameter of SPs by TEM d_{TEM}(nm)
2.1 ± 1.3	**35 ± 4.3**	**22 ± 3.5**
2.7 ± 0.9	**70 ± 6.9**	**58 ± 4.6**
3.4 ± 0.7	**141 ± 14.2**	**112 ± 13.0**
3.9 ± 1.2	**155 ± 19.1**	**130 ± 14.2**
4.6 ± 0.5	**187 ± 24.2**	**178 ± 21.3**

Statistic errors were calculated from multiple measurements on TEM grids and by DLS.

Table 2-4. Dependence of SP diameter on the temperature.

Temperature °C	Diameter of SPs by DLS d_{DLS}(nm)	Diameter of SPs by TEM d_{TEM}(nm)
4	141 ± 14.2	112 ± 13.0
20	162 ± 12.5	118 ± 7.1
30	175 ± 19.0	123 ± 10.4
55	197 ± 21.8	128 ± 9.6
70	204 ± 18.6	142 ± 9.8

Statistic errors were calculated from multiple measurements on TEM grids and by DLS.

Table 2-5. Dependence of SP diameter on ionic strength.

Concentration of NaCl (M)	DLS Diameter of SPs d_{DLS} (nm)	TEM Diameter of SPs d_{TEM} (nm)
0.5	134 ± 18.3	108 ± 9.2
1.0	137 ± 22.4	102 ± 11.4
2.0	144 ± 26.5	aggregated
5.0	152 ± 23.8	aggregated

Statistic errors were calculated from multiple measurements on TEM grids and by DLS.

Chapter 3

Single- and Multi- Component Chiral Supraparticles as Modular Enantioselective Catalysts

Si Li, Juan Liu, Naomi S. Ramesar, Hendrik Heinz, Liguang Xu, Chuanlai Xu, Nicholas A. Kotov. *Nature Communications volume 10, Article number: 4826 (2019)*

3.1 Abstract

Nanoscale biological assemblies exemplified by exosomes, endosomes and capsids, play crucial roles in all living systems. Supraparticles (SP) from inorganic nanoparticles (NPs) replicate structural characteristics of these bioassemblies, but it is unknown whether they can mimic their biochemical functions. Here, we show that chiral ZnS NPs self-assemble into 70–100 nm SPs that display sub-nanoscale porosity associated with interstitial spaces between constituent NPs. Similarly, to photosynthetic bacterial organelles, these SPs can serve as photocatalysts, enantioselectively converting L- or D-tyrosine (Tyr) into dityrosine (diTyr). Experimental data and molecular dynamic simulations indicate that the chiral bias of the photocatalytic reaction is associated with the chiral environment of interstitial spaces and preferential partitioning of enantiomers into SPs, which can be further enhanced by co-assembling ZnS with Au NPs. Besides replicating a specific function of biological nanoassemblies, these findings establish a path to enantioselective oxidative coupling of phenols for biomedical and other needs.

3.2 Introduction

Nanoscale biological assemblies are composed of a diverse spectrum of (bio)organic components,[67,68] which are common in all living systems.[69,70] They have characteristic dimensions ranging from 50 to 500 nm and are exemplified by viral capsids,[36] endosomes,[37] exosomes, carboxysomes,[71] azurophilic granules,[72] cellular vesicles,[73] intralumenal vesicles, and stress granules,[74–77] as well as a wide spectrum of intracellular membraneless compartments.[78,79] These self-contained biological units, chemically related to micelles, are responsible for numerous intracellular and extracellular functions, including high efficiency site-specific transport,[70,73] cargo protection,[36] signalling,[38] catalysis,[40] light absorption,[39,80] biomolecular filters, autophagy,[74] and protein folding.[81,82] Engineered nanocatalysts with chemically similar functions are needed for different technological areas, exemplified by drug delivery, personalized medicine, biotechnology, solar fuels, and CO_2 reduction, which stimulated extensive research in different scientific and engineering fields. Starting with micelles and vesicles from artificial surfactants, bioinspired nanoscale assemblies can be produced from human-made components, including recombinant proteins and amphiphilic biomacromolecules.[41,42,83–87] Similar spheroidal structures can also be made using DNA nanotechnology.[88–90] However, the ex-vivo use of all these nanoassemblies requires the negotiation of both the benefits and problems related to their structural dynamics and instability. The latter problem strongly affects nanoscale bioorganic components such as catalytic proteins,[91] RNA,[92] and DNA.[93] Since inorganic nanoparticles (NPs) have essentially the same ability to spontaneously assemble into complex superstructures,[94] it would be attractive to recreate some of these assemblies and functions from purely inorganic components that are robust and

inexpensive.[95] In this study, we explored this possibility and its associated advantages and disadvantages.

Inorganic constructs that are conceptually similar to nanoscale assemblies from (bio)organic subunits are represented by supraparticles (SPs), formed from 50–500 individual NPs.[6,19,45,96] Similar to micelles, they self-assemble because of the interplay between various attractive forces and electrostatic repulsion associated with the surface charges on NPs that serve here as building blocks, or unimers.[96,97] Gradually increased electrostatic charges of SPs terminates the attachment of new NPs when a certain threshold is reached; this leads to self-limited growth and thus size uniformity. SPs display sizes, uniformity, and geometries reminiscent of nanoscale assemblies found in biology, and can adopt a range of morphologies from fairly simple structures, such as nanospheres[3] or nanoshells[98] to fairly sophisticated left- and right-handed helices.[3,98,99] SPs made of NPs are structurally flexible, enabling their modular engineering from different constitutive units, which are evidenced by the inclusion of biological nanoscale components into the structures of SPs.[4]

Among the many known functions of biological nanoassemblies, transport and catalysis are perhaps the most common. Chiral catalysis takes place in many of these ‘nanoscale organs’, including chloroplasts,[100] endoplasmic reticulum,[101] and endosomes.[37] Following marked advances in this field related to the discovery of 2,2'- binaphthyl-based homogeneous chiral catalysts,[102] research in this area is re-emerging due to the ever-growing demand for chiral intermediates.[103] Although still in the early stages of development, heterogeneous chiral catalysts utilizing inorganic nanostructures provide alternatives to chiral coordination compounds.[104–106] Several recent studies on inorganic NPs used as heterogeneous chiral catalysts have demonstrated their synthetic simplicity and chemical stability.[107–110] However, the chiral bias in these nanoscale

catalytic systems is imparted by complex metalorganic ligands with stereo-selective centers, which leads to their vulnerability of ligand replacement, oxidation, and cross-linking. Conversely, individual NPs with chiral ligands that are short and simple, fail to display observable enantioselectively.[111]

SPs are especially desirable as chiral catalysts because they can potentially mitigate the aforementioned problems. Furthermore, SPs can be flexibly constructed from metal, ceramic, and semiconductor NPs,[112–116] integrating different components into one structural unit optimized for specific reactions and energy sources; this offers the possibility of engineering catalytic systems from nanoscale modules. Here we show that SPs constructed from chiral NPs display catalytic activity and enantioselectivity for the photoinduced oxidation of tyrosine (Tyr), used as a model chiral substrate. The catalytic functions in these assemblies can be engineered and optimized by taking advantage of SP modularity, combining NPs with different chemical and optical properties.

3.3 Methods

Reagents. $Zn(ClO_4)_2 \cdot 6H_2O$, thioacetamide, hydrogen tetrachloroaurate (III) trihydrate ($HAuCl_4 \cdot 3H_2O$), glutathione, and *D*- and *L*- tyrosine (Tyr) were purchased from Sigma-Aldrich. All chemicals were used as received. Milli-Q-deionized water was used for all the experiments.

Characterization methods and instruments. Assemblies were characterized using a JEOL 3011 HRTEM instrument (JEOL USA, Inc.), and a JEOL2100F was employed for HAADF and BF imaging in STEM mode. Elemental analysis was performed using an EDAX accessory linked to the JEOL 2100F instrument (JEOL USA, Inc.), equipped with a UVL-56 lamp without a filter (115 V, 50/60 Hz, 0.16 A).

UV-Vis absorbance spectra were acquired using an Agilent 89090A instrument (Agilent Technologies, Santa Clara, CA, USA). Circular dichroism analysis was performed using a JASCO J-815 instrument. The ζ-potential and size distribution were measured with a Nano ZS Zetasizer instrument (Malvern Instruments, Malvern, Worcestershire, UK). For ζ-potential, each sample was equilibrated for 2 min before measurement; all experiments were performed in triplicate, each measurement included 50 cycles, and a 15 s pause was included between runs.

MS analysis was performed on an Agilent 6520 Accurate-Mass Quadrupole Time-of-Flight (Q-TOF) LC-MS instrument (Agilent Technologies, Santa Clara, CA, USA) operating in ESI^+ ion mode. The nebulization gas was set to 500 L/h at a temperature of 332 °C, the cone gas was set to 5 L min^{-1}, and the nebulizer gas pressure was 45 psi. The capillary voltage was set to 3500 V. Internal reference ion masses $[M + H]^+$ at 121.05 Da and 922.01 Da were enabled, and a detection window of 200 ppm with a minimum height of 1000 counts was used. The results shown in **Fig. 5C** were obtained using an InfinityLab Poroshell 120 HILIC-Z HPLC column (2.1 × 50 mm, 2.7 μm internal diameter).

Synthesis of chiral ZnS SPs. For chiral SPs, 1.36×10^{-3} mol of *L*-, *D*-, or *rac*- penicillamine (Pen) and 1.7×10^{-4} mol $Zn(ClO_4)_2 \cdot 6H_2O$ were dissolved in 86 mL water, the pH was adjusted to 8.5 by adding NaOH, and the solution was degassed by argon bubbling for 30 min. A 1 mL sample of 0.2 M thioacetamide was quickly injected under vigorous stirring and the mixture was incubated at 95 °C in a reflux column system. Samples were taken at different times for measurement and characterization. Pen-stabilized SPs were obtained after 3 h of heating.

Synthesis of chiral gold NPs. Briefly, 50 mL of 4.8 mM glutathione (GSH) solution was mixed with 300 μL 0.5 M $HAuCl_4$ under vigorous stirring. The mixture was heated at 95 °C in an oil bath to obtain chiral gold NPs. The synthesized GSH-Au NPs were purified by placing in a centrifuge at 13000 rpm to remove large aggregates after reaction. The supernatant was further purified by adjusting the solution to pH 3.5, adding 1 volume of ethanol (gold NPs solution : ethanol = 1:1), isolated using a centrifuge at 4000 rpm for 5 min, and the supernatant was discarded. Precipitates were resuspended in 20 mL water.

Synthesis of chiral ZnS-Au SPs. For chiral ZnS-Au SPs, 13.6×10^{-4} mol of *L*-Pen and 1.7×10^{-4} mol of $Zn(ClO_4)_2 \cdot 6H_2O$ were dissolved in water and the pH was adjusted to 8.5. The solution was degassed by argon bubbling for 30 min. Under vigorous stirring, 1.6×10^{-4} mol thioacetamide dissolved in water was added and then degassed for 30 min by argon bubbling. After that, the solution was heated for 30 min at 95 °C, 6 mL of a concentrated dispersion of Au NPs was added and the volume brought to 100 mL. The pH value of the concentrated Au NPs must be adjusted to 8.5 before mixing. The resulting mixture was heated to reflux at 95 °C under flowing argon, and the final Au-ZnS SPs were obtained after 4 h of heating.

Photocatalysis with chiral ZnS SPs and ZnS-Au SPs. Solutions of *L*-Tyr and *D*-Tyr (0.4 mg/mL) were prepared, and synthesized ZnS SPs and ZnS-Au SPs were washed three times with deionized water, and then dispersed in water. Solutions of *L*-ZnS SPs, *D*-ZnS SPs, and *L*-ZnS-Au SPs, assembled with the same concentration of ZnS NPs, were mixed with the same volume of 0.4 mg/mL *L*-Tyr or *D*-Tyr. Control samples were prepared by mixing the same amount of water with *L*-Tyr or *D*-Tyr. Samples of *L*-Tyr, *D*-Tyr, *L*-ZnS-SPs with *L*-Tyr, *D*-ZnS-SPs with *D*-Tyr, *L*-ZnS-SPs with *D*-Tyr, *D*-ZnS-SPs with *L*-Tyr, *L*-ZnS-Au-SPs with *L*-Tyr, and *L*-ZnS-Au-SPs with *D*-

Tyr were mixed thoroughly and the pH was adjusted to 4.7 or 8.0 before illumination. The prepared samples were illuminated with a mercury lamp for the desired time. Catalytic samples were continually stirred during illumination. SPs and solutions were separated by ultra-filtration, and filtered solutions were used for fluorescence and MS analyses. HPLC-MS measurements were performed using a 20 µL injection volume, at testing *m/z* 405.10, 383.12, 361.14, 242.04, 226.05, 220.06, 204.06, 198.08, and 182.08 that corresponded to diTyr-Na + Na^+, diTyr + Na^+, diTyr + H^+, DOPA-Na + Na^+, Tyr-Na + Na^+, DOPA + Na^+, Tyr + Na^+, DOPA + H^+, and Tyr + H^+, respectively.

Enantioselectivity of chiral SPs for *rac*-Tyr. *L*-ZnS, *D*-ZnS, *rac*-ZnS, and *L*-ZnS-Au SPs were incubated with 0.4 mg/mL *rac*-Tyr for 6 h with stirring. Sodium chloride was then added to obtain a concentration of 0.5 M in order to cause the sedimentation of SPs. As the SPs settled to the bottom, no centrifugation was needed. The supernatant from the top part of the vial was diluted with ultrapure water to avoid saturation of the detectors. The diluted samples of the supernatant were used for absorbance and CD measurements.

Construction of molecular models and simulation setup. All-atom models of the ZnS NP, (*L*)-Pen, (*D*)-Pen, (*L*)-Tyr, (*D*)-Tyr, and water were built using Materials Studio. A nanoparticle model of 3 nm size ($Zn_{369}S_{348}S(Ligand)_{54}$) was created from a multiple of the unit cell of sphalerite (ZnS) and application of a spherical cutoff. Atomic charges were assigned with charge increments of ± 0.25 e per bonded neighbor, corresponding to an atomic charge of +1.0 e for Zn and -1.0 e for S in bulk ZnS, and accordingly reduced charges on the surface. 54 (*L* or *D*)-Pen ligands were bound via thiol linkages to the surface and randomly spread (packing density ~1.9 per nm^2).[117] The

protonation states of carboxylic acid groups and amine groups in (*L* or *D*)-Pen and (*L* or *D*)-Tyr were adjusted to COO^- and NH_3^+ to represent neutral conditions of pH ≃7 as in experiment.

Simulations were performed for four systems, including (1) *L*-Pen-ZnS-*L*-Tyr, (2) *L*-Pen-ZnS-*D*-Tyr, (3) *D*-Pen-ZnS-*L*-Tyr, and (4) *D*-Pen-ZnS-*D*-Tyr. The dimensions for each box was the same, about 70 × 70 × 70 $Å^3$, and all simulation systems were overall charge-neutral. The complete start structures consisted of one ZnS NP modified with (*D*) or (*L*) Pen, 8 (*D*) or (*L*) Tyr molecules in solution, and 10229 water molecules. The Tyr molecules were evenly placed in the box with ~10 Å distance from the Pen-ZnS NP.

Force Field. We employed the CHARMM-Interface force field (CHARMM-IFF) including new parameters for ZnS (Table 1)[118] and existing CHARMM36[119] parameters for (*L* or *D*)-Pen and (*L* or *D*)-Tyr. The new force field parameters for ZnS describe the expected amount of covalent and ionic bonding[119,120] and reproduce the lattice parameters (5.4093 Å) and density (4.09 g/cm^3) from XRD data (**Figure 3-17**) with 0.2% deviation (5.394 Å) and 0.7% deviation (4.12 g/cm^3), respectively, at 298.15 K and 1 atm. The Lennard-Jones parameters approximated surface and interfacial energies of ZnS (not tested in detail).[121]

Table 3-1. Forcefield parameters for ZnS (sphalerite)

I. Nonbond	**Charge (e)**	σ (pm)	ε (kcal·mol^{-1})
Zn	+1.00	185	0.05
S	-1.00	448	0.5
II. Bond	r_0 **(pm)**		k_r **(kcal·mol^{-1}·$Å^{-2}$)**
Zn-S	2.41		525
Zn-S (ligand)	2.41		525
III. Angles	θ_0 **(°)**		k_θ **(kcal·mol^{-1}·rad^{-2})**
Zn-S-Zn	109.5		200
S-Zn-S	109.5		200

S-Zn-S (ligand)	109.5	200
Zn-S-C (ligand)	100.0	0

Note: No dihedral potentials were necessary for bonds inside the ZnS NP (zero).

Simulation Protocol. Each system was initially subjected to 1000-time steps energy minimization to remove atomic close contacts. The configurations were then subjected to an initial 2 ns equilibration period of molecular dynamics simulation in the NPT ensemble at 298.15 K and 1.013 MPa using the Nanoscale Molecular Dynamics program (NAMD),[122] followed by longer simulation times of 50 ns to thoroughly sample conformations and thermodynamic averages. All atoms were flexible during the simulations, the time step was 1 fs, temperature controlled by the Langevin thermostat, and a damping coefficient of 1 ps^{-1}. Van-der-Waals interactions were treated with a spherical cutoff of 12 Å in the summation of pairwise Lennard-Jones interactions, and the summation of Coulomb interactions was carried out using the Particle Mesh Ewald (PME) method with a high accuracy of 10^{-6} kcal/mol throughout the equilibration and production runs.

Analysis and calculation of binding frequency. The conformations and dynamics were visually analyzed using the Visual Molecular Dynamics (VMD) program.[123] Binding was defined as uninterrupted proximity of tyrosine molecules to the Pen-ZnS nanoparticle within 5 Å for 100 ps or more. The binding frequency was calculated from the number count of binding frames, that is, the sum of the number n_i of Tyr molecules bound in each frame i over all frames N, relative to the total number of frames N and 8 Tyr molecules:

$$Binding\ \ frequency = \frac{\sum_{i=1}^{N} n_i}{8 \cdot N} \qquad \textbf{(3-1)}$$

Uncertainties are given using block averages of the binding frequency over major portions of the total simulation time.

3.4 Results and Discussion

Key problems of nanoassemblies for chiral catalysis. While numerous chiral NPs and their assemblies have been reported over the last two decades, these studies were primarily focused on understanding and maximizing chiroptical activity [109–111,124,125] When designing NP assemblies to display chiral bias, one encounters the fundamental problem of the mismatch in scales between the chiral geometries characteristic of small molecules needed for pharmaceuticals, liquid crystals, chiral polymers, and other needs versus the chiral shapes of NPs. For example, in the classical case of tartrate, only five atoms constitute the chiral atomic group with a dimension of only a few angstroms, whereas the number of atoms in chiral NPs and constructs thereof can exceed tens of thousands, with dimensions from a few nanometers to 100 nm. Additionally, NPs always have structural imperfections and variability in their atomic and molecular scales that inevitably lead to difficulties with the realization of fine angstrom-scale stereochemical control typically expected for chiral catalysts, albeit this may not be always needed.

We addressed these problems using SPs formed from semiconductor NPs as the basic structural modules.[98] The interstitial spaces between NPs in these nanospheroids are subnanometer in width and are comparable to the dimensions of small molecules serving as catalytic substrates. However, there is a tendency for NPs to form assemblies with nearly epitaxial merging of crystal lattices.[126–128] While useful in electronics[129] and energy storage applications,[130] this is detrimental to chiral catalysis because it eliminates the SP's chirality in the nanoscale pores. Therefore, NPs

with relatively high recrystallization energies and interatomic bonds with fairly strong covalent character are preferred.

Assembly of chiral supraparticles. Assembly of chiral SPs can be accomplished by assembling ZnS NPs with an average diameter, d_{TEM} = 3 ± 0.7 nm, stabilized by *L*- or *D*-penicillamine (Pen) (**Figure 3-1a**); when needed, the *rac*-form of Pen was also utilized, resulting in NPs of similar size and polydispersity. The synthesized chiral SPs will be referred to as *L*-, *D*-, or *rac*-SPs, depending on the chirality of the surface ligand tethered to the NPs. Unlike optical centers formed by sp^3 hybridized carbon atoms, chiral NPs and their assemblies have multiple scales of mirror asymmetry.[103] Thus, *L*-, *D*-, or *rac*-notations refer *only* to the preparative methods rather than to geometrical attributes of the nanoassemblies.

Pen-ZnS NPs were synthesized and assembled into SPs by incubation at 95 °C for 3–6 hours (see Methods). The individual ZnS NPs exhibited irregular morphology as seen from the high-resolution transmission electron microscopy (HR-TEM) images (**Figure 3-7**). Association of NPs is accompanied by the concomitant increase of the absolute value of electro-kinetic zeta-potential (ζ) (**Figure 3-8**). The point where it reaches a plateau corresponds to the formation of SPs, and for Pen-ZnS NPs, this occurs in three hours, when ζ reaches -47 mV. The resulting SPs displayed a spherical morphology with diameters determined by transmission electron microscopy (TEM) and dynamic light scattering (DLS) of d_{TEM} = 100 ± 3 nm and d_{DLS} = 105 ± 10 nm, respectively (**Figure 3-1b–d**, **Figure 3-9** **Figure 3-10)** They also showed high monodispersity with standard deviation <6%, which indicates the quasi-equilibrium state of the SPs. Elemental mapping confirmed the composition of SPs, indicating the presence of ZnS and Pen (**Figure 3-1e**). The presence of Pen ligands in ZnS SPs was also confirmed by the Fourier-transform infrared

spectroscopy (FTIR) and Raman spectra (**Figure 3-11 -Figure** 3-12). The typical peaks at 3000–3300 cm^{-1} are attributed to the stretching vibration of N-H of Pen attached to the surface of ZnS NPs. The peaks at 1450–1700 cm^{-1} and 2200–2450 cm^{-1} are attributed to C-H bending and S-H stretching vibrations of Pen. The peaks associated with S-H bonds could not be observed for Pen-ZnS SPs as expected, due to the formation of S-ZnS bonds.

Individual NPs could be identified in the assembled SPs by high-angle annular dark-field scanning transmission electron microscopy (HAADF-STEM) images and high-resolution STEM images (**Figure 3-1b, Figure 3-13Figure 3-14Figure 3-15**). The pore size of the SPs are below 2 nm (**Figure 3-16b**), which are comparable with the sizes of reactive centers on many enzymes.[131] The X-ray diffraction (XRD) spectra for SPs revealed [0036], [110], [1136], [1211] peaks of ZnS in SPs (**Figure 3-17**).

Chirality of assembled supraparticles. ZnS NPs with L- and D-Pen as surface ligands displayed circular dichroism (CD) peaks at 215 and 240 nm (**Figure 3-2a, b**). Compared with the CD spectra of Pen alone (**Figure 3-18**), a new CD peak appeared from 240 to 300 nm; this may be attributed primarily to electronic hybridization between the molecular orbitals of NPs and those of chiral ligands. The local distortions of the ZnS surface due to attachment of Pen ligands may contribute to the CD spectra, too.

Assemblies of individual NPs into ordered structures may exhibit CD signatures of the chiral geometries of NPs that may or may not possess a distinctively chiral shape, such as a helix. Unlike the individual NPs, the chiroptical activity of the prepared SPs included an additional band in the 280–340 nm region. Note that the energies of electronic state developing as a result of hybridization of chiral states from amino acid residues attached to the NP surface are dependent

on the environment. They are different for the individual NPs and that in the interstitial spaces and thus are located at longer wavelengths. One can also expect that CD peak for such electronic states will be broad as they are, indeed, in **Figure 3-2d**.

Assembly of multi-component chiral supraparticles. Similar to other terminal assemblies, SPs can be made from several different NPs so that they may offer a combination of different functionalities. For instance, the co-assembly of NPs from metals and semiconductors is a simple process that results in the combination of NPs with plasmonic and excitonic properties, which should facilitate photocatalytic processes. Gold NPs carrying glutathione (GSH) units as surface ligands were chosen as complementary unimers to the Pen-stabilized ZnS NPs for the assembly of plasmon–exciton SPs because of their similarity in size. When GSH-Au NPs with diameters of 2 ± 0.3 nm (**Figure 3-19**) were added to a dispersion of ZnS SPs and incubated for 3 h at 95 °C, hybrid ZnS–Au SPs containing both types of constituent blocks were obtained (**Figure 3-3a**). The ζ-potential of the multi-component SPs stabilized at a high value of ~−44 mV after 4 h of incubation, indicating the successful formation of SPs (**Figure 3-20**). Note that the ζ-potential characteristic of the completed self-assembly process is nearly identical to that found for ZnS nanospheroids (**Figure 3-8**). The average diameter of ZnS–Au SPs was $d_{TEM} = 75 \pm 3$ nm (**Fig. 3b; Figure 3-21**), which was about 25% smaller than the diameter of single-component nanoassemblies. Elemental mapping confirmed the presence of gold NPs in these SPs (**Figure 3-3c**). ZnS–Au SPs displayed CD signals from 200 to 550 nm (**Figure 3-3d**). The polarity of chiroptical activity at 220 nm for L-ZnS–Au, that is, those where ZnS NPs were made with L-Pen, was opposite compared with the CD spectra of single-component ZnS SPs (**Figure 3-2d**) and GSH-Au NPs (**Figure 3-19b**). The polarity reversal may have multiple physical origins and likely

represents a convolution of various effects. It may be attributed to both strong chemical (such as hydrogen bonding between the surface ligands) and physical (such as plasmon–exciton hybridization) interactions between ZnS and Au NPs in the nanoassemblies.

Supraparticles as modular photo-catalysts. The chirality of SPs can potentially endow them with enantioselectivity in catalysis. Realization of enantioselective photocatalysts would be particularly promising because the photoinduced reactions require both optical activity and robustness of inorganic NPs to prevent their photodecomposition. The conversion of the amino acid Tyr, which can be monitored using its strong photoluminescence (PL) peak at 306 nm, was used as a chiral catalytic substrate. Furthermore, Tyr can be photo-oxidized to dityrosine (diTyr)[132–136] or dihydroxy phenylalanine (DOPA),[134] with characteristic PL peaks at 414 nm and 320 nm **(Figure 3-22)**, respectively. The realization of asymmetric photo-oxidative coupling of Tyr to diTyr would be particularly impactful from the standpoints of both chiral catalysis and pharmaceutical intermediates because enantioselectivity for such reactions was so far challenging to realize.[137–139]

Chiral Photocatalysis by ZnS Supraparticles: The photocatalytic reactions in all experimental series were initiated by illumination at pH 8.0 with UV light at 315−400 nm, which was efficiently absorbed by ZnS and ZnS–Au SPs **(Figure 3-2c and Figure** 3-3**d)**. Illumination of Tyr without SPs yielded a nearly negligible change in PL spectra (**Figure 3-4a, b**). When ZnS SPs were added to the Tyr solution, a strong increase in PL intensity was observed at 414 nm, which is characteristic of the accumulation of diTyr (**Figure 3-4c–f**)[133,135] DiTyr formation was accompanied by a decrease of PL intensity at 306 nm as expected considering the consumption of Tyr. While diTyr was the main product of the photocatalytic conversion of Tyr, the formation of

DOPA may also be expected, which explained the red-shift of the emission peak at 306 nm in **Figure 3-4** as the photolysis proceeded.

Analysis of temporal profiles of diTyr emission, $I_{414}(t)$, allowed us to evaluate the chiral preferences of the SP catalysts. ZnS SPs carrying *L*-Pen preferentially catalyzed *L*-Tyr, while SPs made from *D*-Pen preferentially catalyzed *D*-Tyr (**Figure 3-4g**). The degree of enantioselectivity can be associated with preferential partitioning of enantiomers of Tyr into the SPs, which was confirmed by an enantioselective adsorption of Tyr enantiomers after exposure of *rac*-Tyr solution to *L*- or *D*-ZnS SPs. The effect of preferential adsorption of enantiomers on chiral substrates and phases was observed for some other systems,[124,140–142] but, to the best of our knowledge, not for SPs or any other nanoscale assemblies of NPs. Calibration of the CD spectra with respect to the total concentrations of each enantiomer (**Figure 3-23Figure 3-24**) yields preferential partitioning of L-Tyr and D-Tyr into L- and D-ZnS-SPs as 38.4 ± 1.8% and 36.3 ± 2.4% over the other isomer, respectively, while that of L- and D-ZnS NPs was 11.5% ± 3.1% and 15.1% ± 3.4% over the other isomer. Thus, the enantioselective recognition was vividly enhanced via assembling chiral NPs into SPs. The chiral preferences of SP–substrate interactions match those observed in photocatalysis, which is consistent with the enantioselective physisorption of substrates with NPs and SPs **(Figure 3-4g**). The individual ZnS NPs with L- or D-ligands did not show obvious catalytic preference for enantiomeric Tyr, and the catalytic activity is also lower than that of the SPs (**Figure 3-25**). Both the ZnS NPs and ZnS SPs retain excellent stability in the course of photocatalysis (**Figure 3-26 Figure 3-27**). Importantly, the photochemical stability of chiral ligands on SPs is markedly better than that on NPs. In fact, no decomposition of Pen was observed in SPs after intense illumination for 36 h (**Figure 3-4h**).

When Tyr was illuminated in the presence of ZnS–Au SPs, the fluorescence intensity of the 306 nm band decreased dramatically during the illumination **(Figure 3-5a-b**), which indicated a large enhancement of the efficiency of photocatalytic conversion of Tyr after incorporation of Au NPs. Note, however, that the rise of the 414 nm peak associated with diTyr was smaller in ZnS–Au than in ZnS SPs (**Figure 3-4c–f and Figure** 3-5**a-b**), pointing to the simultaneous enhancement of diTyr conversion into non-luminescent products.

As a result of the higher catalytic activity of ZnS–Au SPs, weaker PL signature of diTyr, and greater complexity of the products than in single-component SPs, the chemical composition of products of photocatalysis were investigated using additional analytical techniques. High-performance liquid chromatography–mass spectrometry (HPLC-MS) confirmed the efficiency of the photoinduced oxidative coupling of Tyr by ZnS–Au SPs. The peaks in extracted ion chromatography (EIC) provided spectra tracings that concomitantly verified the conversion of Tyr to diTyr and DOPA (**(Figure 3-5c**). The gradual stabilization of the EIC peaks corresponding to diTyr and DOPA for the reaction time from 18 to 32 h confirmed the ability of multi-component SPs to subsequently oxidize diTyr and DOPA, which was not the case for single-component SPs..

Similar to ZnS SPs, the temporal dependence of PL intensity at 306 nm revealed that L-ZnS–Au SPs preferentially catalyzed the photo-oxidation of L-Tyr over D-Tyr (**(Figure 3-5d).** The association of enantioselectivity of the photocatalysis with preferential partitioning of a specific enantiomer was confirmed for the multi-component SPs. When incubated with rac-Tyr, L-ZnS–Au SPs prefer to adsorb L-Tyr in the amount $44.2 \pm 1.7\%$ greater than that for D-Tyr (**Figure 3-24 and Figure 3-28**). Selective adsorption of Tyr enantiomers in ZnS and ZnS–Au SPs indicates that ZnS NPs with Pen surface ligands are primarily responsible for the chiral bias of the photo-oxidation process. The improved catalytic performance of Au–ZnS SPs can be attributed to

more facile separation of photogenerated electrons and holes and the reduced band gap of ZnS. The photogenerated electrons prefer Au surface rather than ZnS. The holes, however, will mainly stay on the ZnS nanoparticles, which will reduce the recombination of the electron-hole pairs and enhance the catalytic efficiency.

The photochemical stability of chiral ligands on Au–ZnS SPs was shown to exceed those in the dispersion of individual ZnS and Au NPs (**(Figure 3-5e**). No degradation of Pen and GSH was observed for illumination for 60 h whereas marked reduction of CD intensity of the peaks corresponding to both peptides was observed for free NPs over the same time.

There are several chemical mechanisms why the stability of the ligands would increase in SPs compared to chiral photocatalysts based on single NPs or traditional organometallic compounds. First, SPs afford utilization of short and robust chiral ligands, such as individual amino acids as molecular structures responsible for enantioselectivity, as opposed to complex and sensitive high molecular weight constructs. The higher the molecular weight of the surface ligands, the greater number of conformational degrees of freedom, and the greater the possibility of chemical damage due to photonically or thermally initiated reactions. Second, the light in SP is absorbed by a subset of NPs. These can be the NPs in the surface or Au NPs in ZnS or Zn-S–Au SPs, respectively. Unlike single NPs or the traditional chiral photocatalysts, the excitation can be efficiently transferred between several NPs due to their closeness in the SP assemblies. The resonance coupling of the excited states in SPs is advantageous for the stability of the chiral photocatalysts because on chiral ligands on the internal NPs are better protected against damage than those on the SP surface. Third, SPs represent a self-assembled hybrid composite where ZnS cores and organic ligands on their surface constitute the mineral and organic components, respectively. Multiple experimental data indicate that the organic molecules in the composite display increased resilience

to oxidation, thermal decomposition, or hydrolysis.[143–145] This property represents the fundamental structural advantage of SPs as chiral photocatalysts.

Molecular dynamics simulation. Molecular dynamics simulation can be a powerful tool for investigation of the atomic scale dynamics and molecular recognition properties at NP surfaces, and was applied here to obtain insight into the recognition of (L or D)-Tyr in aqueous solution on (L or D)-Pen-ZnS NPs (**Figure 3-6**). The enantioselectivity of Pen-ZnS surfaces were evaluated using the binding frequency of Tyr enantiomers to the Pen ligands on single NPs and model nanoassemblies from four NPs (**Figure 3-29**) during 50 ns and 20 ns, respectively, molecular dynamics simulations in explicit water at pH 7.0 (**Figure 3-6**). Binding for both single- and four-NP systems decreases in the order D-Pen/D-Tyr > L-Pen/L-Tyr > L-Pen/D-Tyr > D-Pen-L-Tyr, which matches with the reaction rate for Tyr consumption and diTyr formation (**Figure 3-4g from measurements**). The most preferable binding interactions occur between –COO− ions in Pen and –NH3+ groups in Tyr, as well as between –NH3+ groups in Pen and –COO− groups in Tyr in all four systems (**Figure 3-6b**). The binding involves ion pairing and hydrogen bonds. Once two binding contacts simultaneously form between a Pen ligand and Tyr, Tyr will remain bound in excess of 10 ns. When only one of the binding contacts forms, the binding status is more dynamic and lasts only 1–2 ns. As the aromatic side group of Tyr approaches the bare ZnS NP surface, the –OH group may temporarily bind to the ZnS surface and disengage binding to Pen via ion pairing. Differences in binding properties for different chirality combinations of ligands and Tyr molecules are related to distinct relative orientations of the carboxylate and ammonium groups of Pen on the particle surface (inward/outward depending on D/L), as well as specific interactions between neighbor ligands. Tyr binds selectively to these chiral ligand surfaces and experiences some geometry differences in match depending on (D) or (L) configuration. In addition, the binding

competition between the charged groups in Tyr (–NH3+ and –COO−) with Pen ligands and the aromatic side groups in Tyr with uncovered areas of the ZnS NP surface demonstrates that the pH value and the density of surface ligands can affect the binding affinity. Diffusion rate of L-Tyr in the center of four-NP assembly was found to be 0.22±0.05 and 0.34±0.12 A/ns for D- and L-Pen-ZnS models, respectively. Concurrently, the diffusion rates of L-Tyr on the sides of the nanoassembly were much faster - 2.2±0.6 and 1.8±0.5 A/ns for the same models. This observation supports the attribution of experimentally observed enhancement of both catalytic activity and enantioselectivity in SPs vs. NPs to extended residence time of substrate inside the catalytic particle.

3.5 Conclusions

Single- and multi-component SPs with size and uniformity comparable to biological nanoassemblies were assembled from chiral semiconductor and metallic NPs mimicking both structure and functions of their biological analogs, for instance photosynthetic organelles of bacteria and, to a lesser extent, redox reactions in azurophilic granules. SPs showed efficient photocatalysis of Tyr with enantioselectivity determined by the chiral preferences of L- and D-Tyr to interact with individual NPs and penetrate into the interstitial spaces between them. It needs to be pointed out that enantioselectivity of oxidative phenol coupling, which is Tyr–Tyr dimerization is representative of, is both difficult[137,138] due to low chiral bias and significant due to variety of biomedical needs41. The problems with enantioselectivity are particularly noticeable for low molecular weight phenols as opposed to large molecular[139] weight polycyclic aryls[146]. As such, optical purity of just a few percent is typically achieved even with complex metalorganic catalysts for diverse catalytic substrates[139]. In the majority of cases, however, no enantioselectivity was

reported[137,138] and poor enantioselectivity of these reactions was pointed out even for sophisticated biomimetic catalysts[139].

Incorporation of Au NPs to realize multicomponent SPs further enhanced photocatalytic conversion of the substrates. Besides improved electron-hole separation, more efficient light absorption by the assemblies via plasmonic effects and the formation of the NP junctions can facilitate both the electron transport, while retaining enantioselectivity. Concomitantly, photodecomposition under light is an essential problem of the chiral catalysts of any chemical type. Improving the resilience of chiral photocatalysts against photodegradation is an important advancement in the field that facilitates their practical implementation.

One can expect SPs to be a convenient platform for engineering catalysts using different NPs as functional modules. SPs provide a new approach to design a family of chiral catalysts conceptually different from those considered before in the field of homogeneous and heterogeneous chiral catalysts. Permutations of different NPs that can be combined in modular SPs is nearly endless. The development of more specific and sophisticated SPs that can replicate multiple other functions of biological nanoassemblies is anticipated.

3.6 Figures

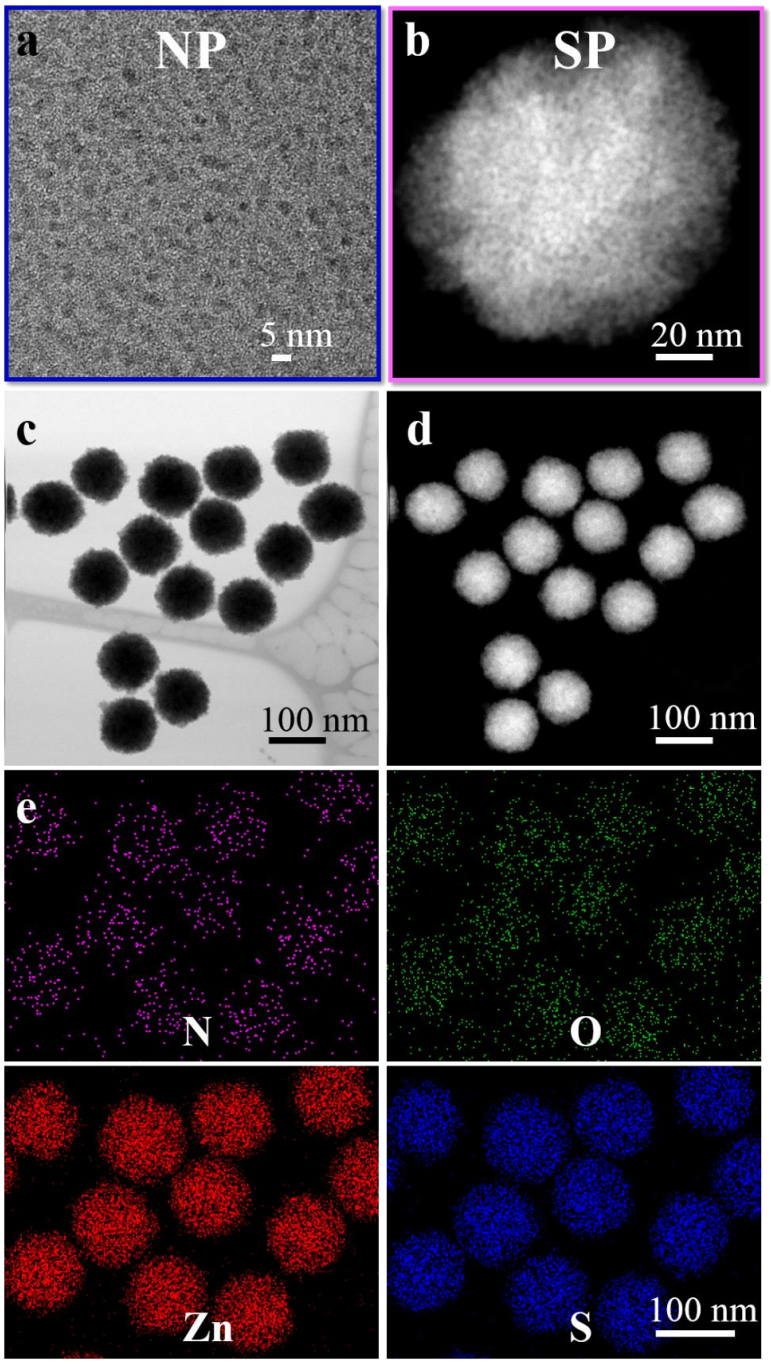

Figure 3-1. Pen-stabilized chiral NPs and SPs. (a) TEM image of L-Pen-stabilized ZnS NPs. (b) Magnified HAADF-STEM image of L-ZnS SPs that assembled from the chiral NPs shown in a. (c) HAADF-STEM image and (d) Bright-field-STEM image of L-ZnS SPs (100 ± 4 nm) with large scale. (e) Elemental mapping images of nitrogen, oxygen, zinc, and sulfur ZnS SPs

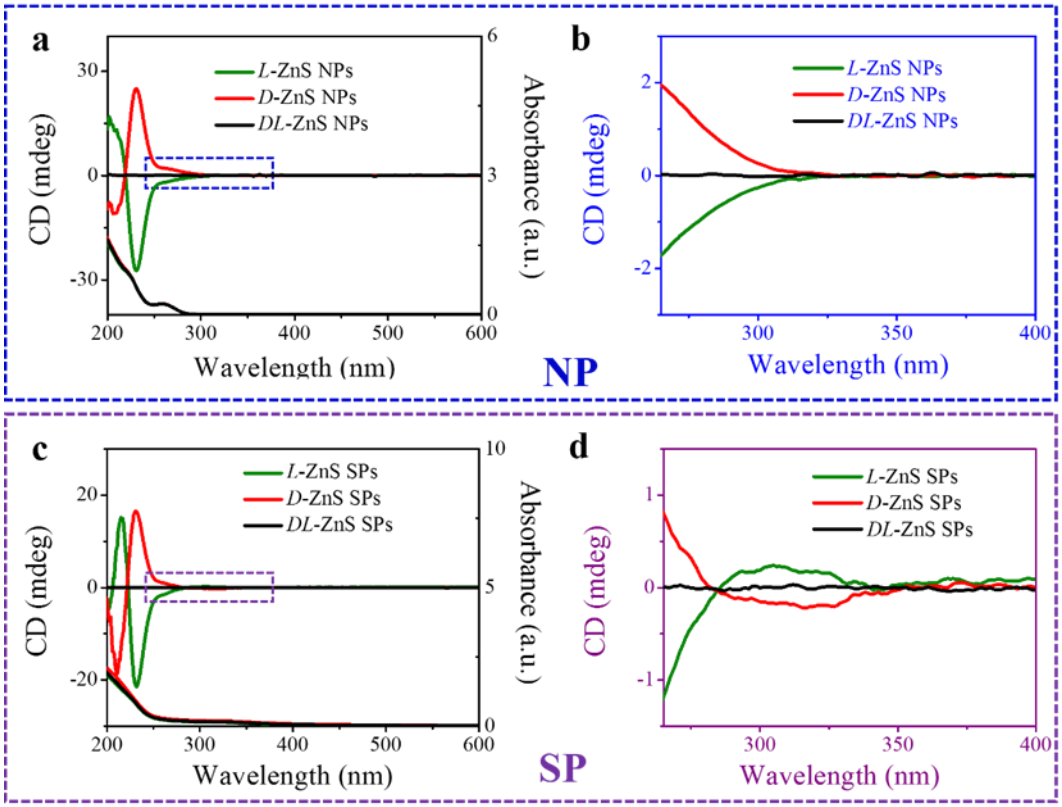

Figure 3-2. (a) **CD spectra and UV spectra of ZnS NPs with Pen surface ligands of different chirality.** (b) **Enlarged CD spectra of ZnS NPs from 265 to 400 nm.** (c) **CD spectra and UV spectra of ZnS SPs with Pen surface ligands of different chirality.** (d) **Enlarged CD spectra of ZnS SPs from 265 to 400 nm.**

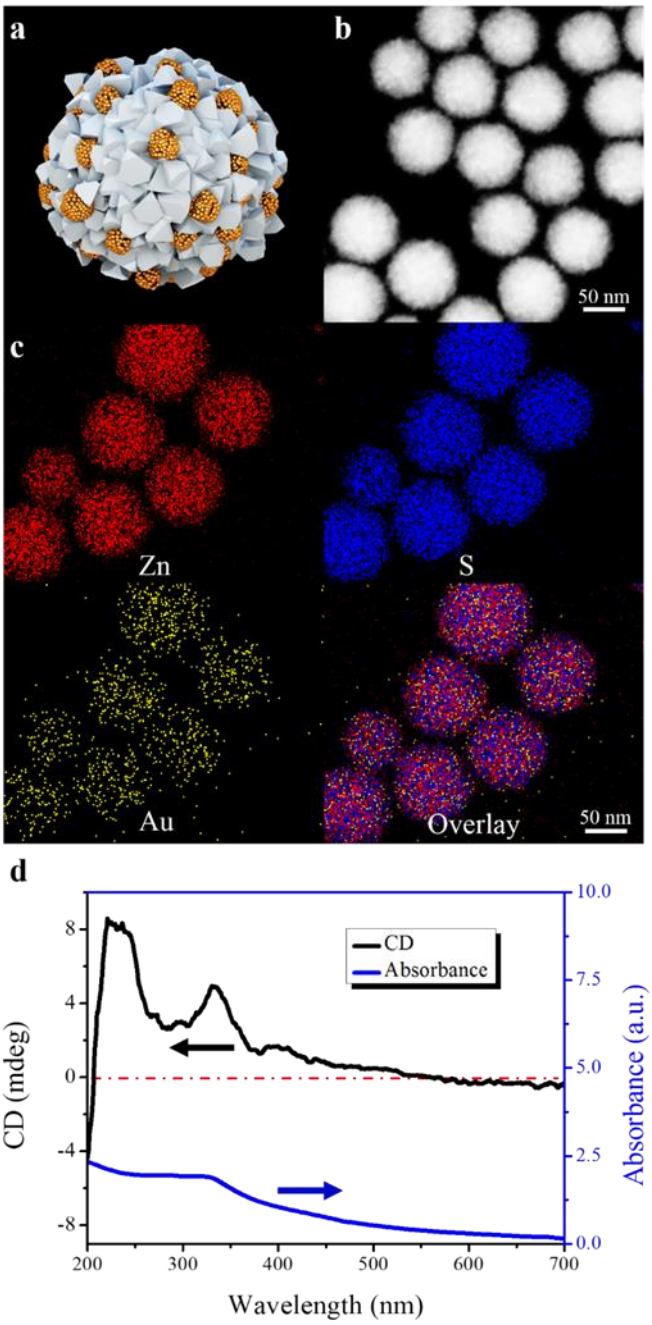

Figure 3-3. (a) **Model of multi-component *L*-ZnS-Au SPs.** (b) **HAADF-STEM images of multi-component *L*-ZnS-Au SPs.** (c) **Elemental mapping of *L*-ZnS-Au SPs of zinc, gold, and sulfur, respectively.** (d) **CD and UV spectra of multi-component *L*-ZnS-Au SPs.**

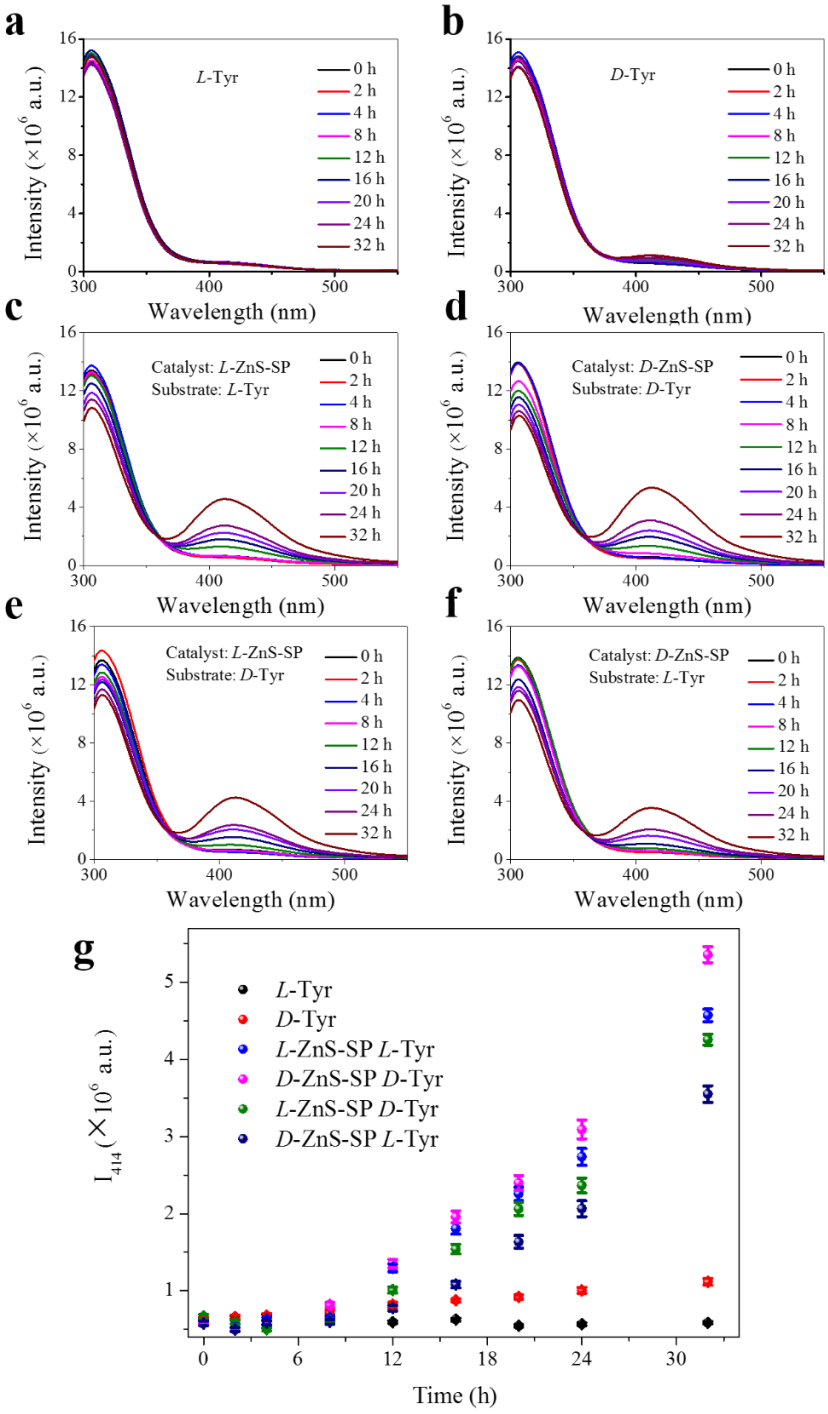

Figure 3-4. Fluorescence spectra of *L*-Tyr or *D*-Tyr after being illuminated with different periods of time in the absence or presence of ZnS SPs. (a) *L*-Tyr. (b) *D*-Tyr. (c) *L*-Tyr with *L*-ZnS SPs. (d) *D*-Tyr with *D*-ZnS SPs. (e) *L*-Tyr with *D*-ZnS SPs. (f) *D*-Tyr with *L*-ZnS SPs. (g) The dependence of PL intensity at 414 nm on the time of photocatalytic reaction with ZnS SPs of different chirality of the catalyst and the substrate.

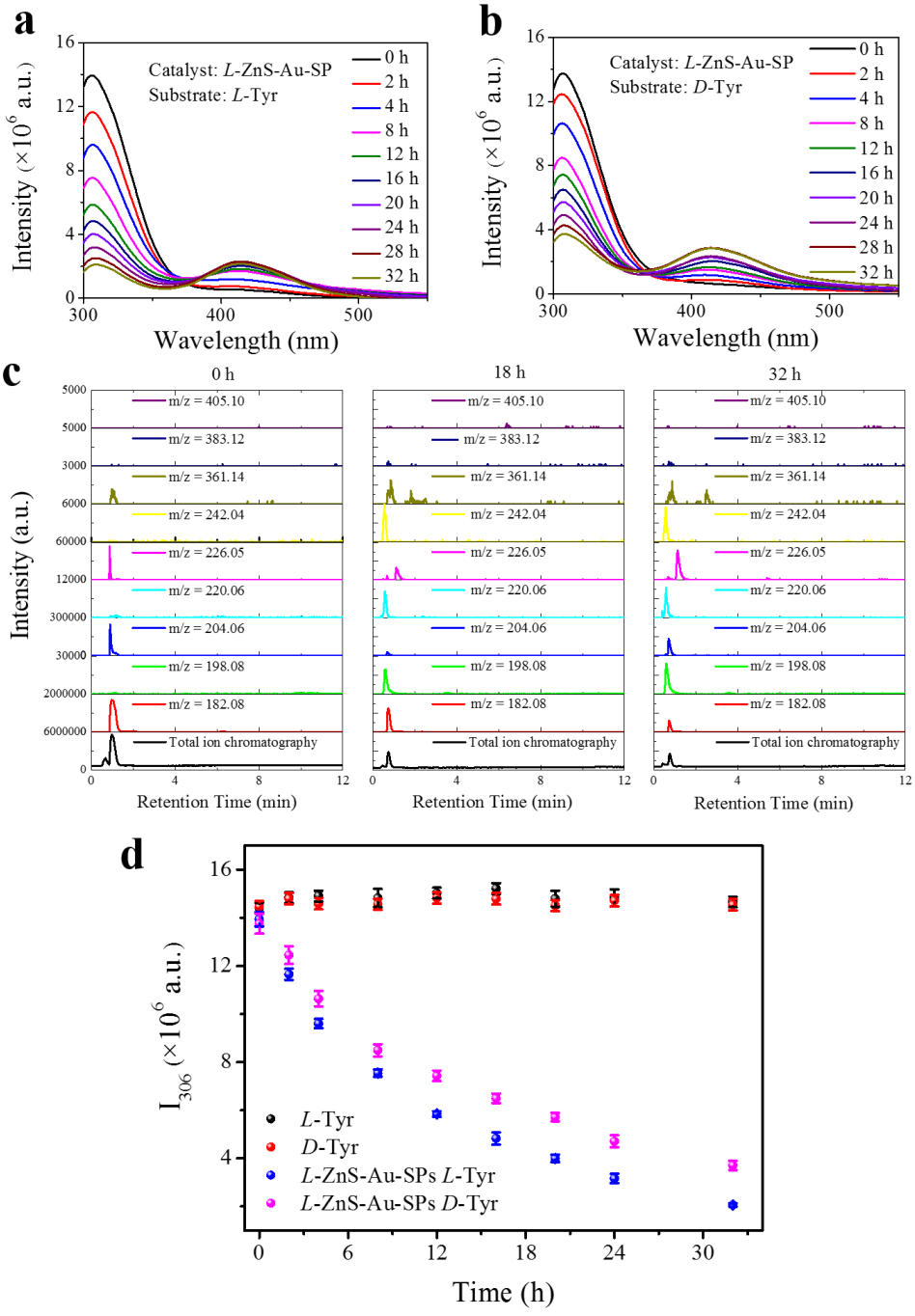

Figure 3-5. Fluorescence spectra of L-Tyr or D-Tyr after being illuminated with different period of time in the presence of ZnS-Au SPs. (a) L-Tyr with L-ZnS-Au SPs. (b) D-Tyr with L-ZnS-Au SPs. (c) Extracted ion chromatography (EIC) of L-Tyr and Tyr related products of L-ZnS-Au SP L-Tyr samples obtained at 0, 18, and 32 hours, m/z = 405.10, 383.12, and 361.14, and m/z = 242.04, 220.06, and 198.08 are attributed to DOPA-Na + Na+, DOPA + Na+, and DOPA + H+ and diTyr-Na + Na+, diTyr + Na+ and diTyr + H+, respectively. (d) The dependence of PL intensity at 306 nm on photocatalytic reaction time with L-ZnS-Au SPs of different chirality of the substrate.

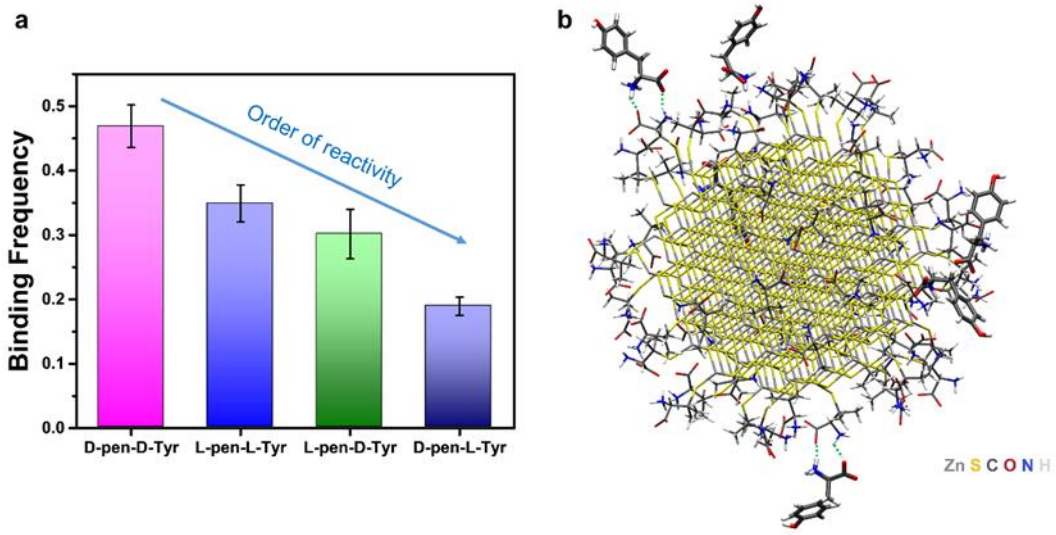

Figure 3-6. Adsorption of (*L* or *D*)-Tyr on (*L* or *D*)-Pen-ZnS NPs of 3 nm diameter from MD simulations. (a) The binding frequency decreases in the order from *D*-Pen-*D*-Tyr, *L*-Pen-*L*-Tyr, L-Pen-*D*-Tyr, to *D*-Pen-*L*-Tyr. Error bars indicate the standard error from 5 ns block averages during 50 ns MD simulations. (b) Snapshot of *D*-Tyr binding on the *D*-Pen-ZnS NP surface. *D*-Tyr molecules are represented in "Licorice" style with thicker bonds. The 3 nm *D*-Pen-ZnS NP is represented in "Licorice" style with thinner bonds. Binding sites are highlighted with green dotted lines and water molecules omitted for clarity.

3.7 Supplementary Information

Calculation of Enantioselective Partitioning of Tyr Enantiomers into Supraparticles. The concentration of Tyr in the supernatant denoted as CTyr1, was calculated from the UV-Vis absorbance spectra in Supplementary Fig. 17b and 22b using the equation IA = 18.200 CTyr1 - 0.0273 (Supplementary Fig. 18b). The amount of Tyr (CTyr2) partitioned into SPs, which lead to the appearance of a CD signal of the supernatant solution, was calculated with the calibration equation ICD = 128.505 CTyr2 - 0.0244 (Supplementary Fig. 18d) based on the data in Supplementary Fig. 17b and 22b. The enantiomer selectivity for SP partitioning was calculated using the equation Vselectivity = CTyr2 / CTyr1.

Supplementary Figures

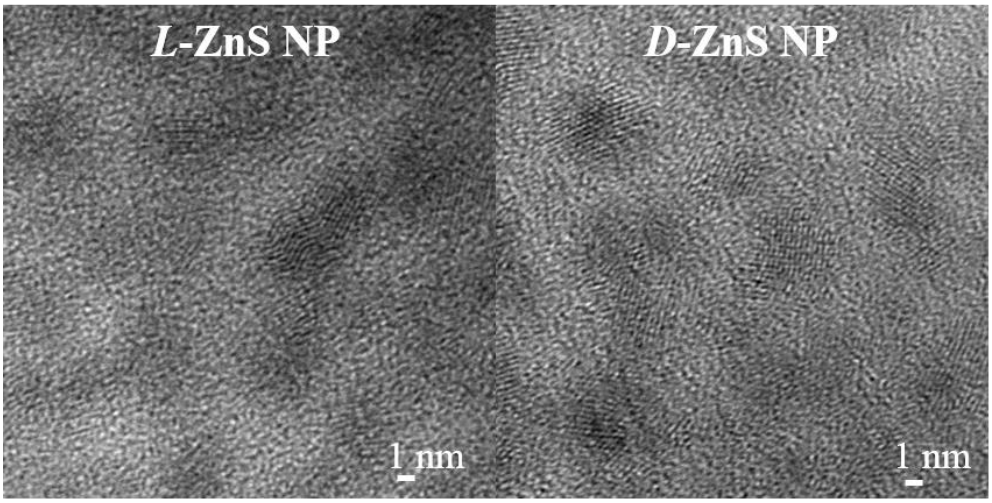

Figure 3-7. HR-TEM images of *L*- and *D*- ZnS NPs.

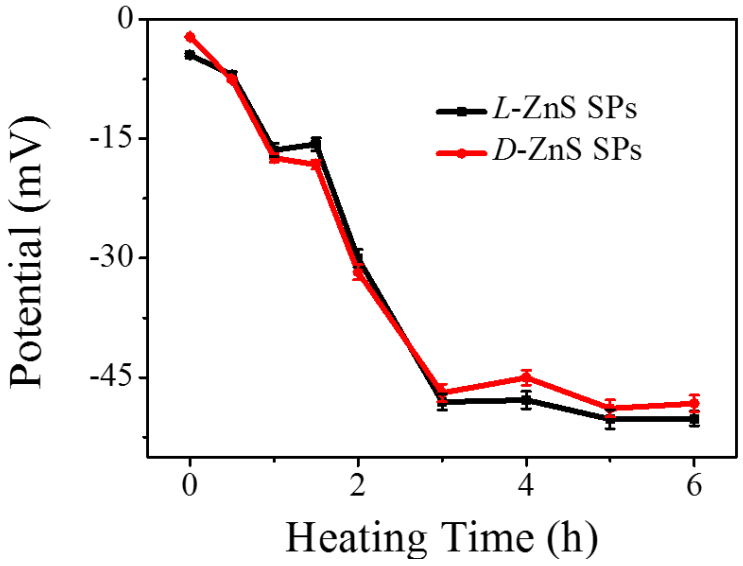

Figure 3-8. Temporal profile of ζ-potential for the assembly of *L*- and *D*-ZnS NPs. The error bars represent the standard deviation of sample measurements.

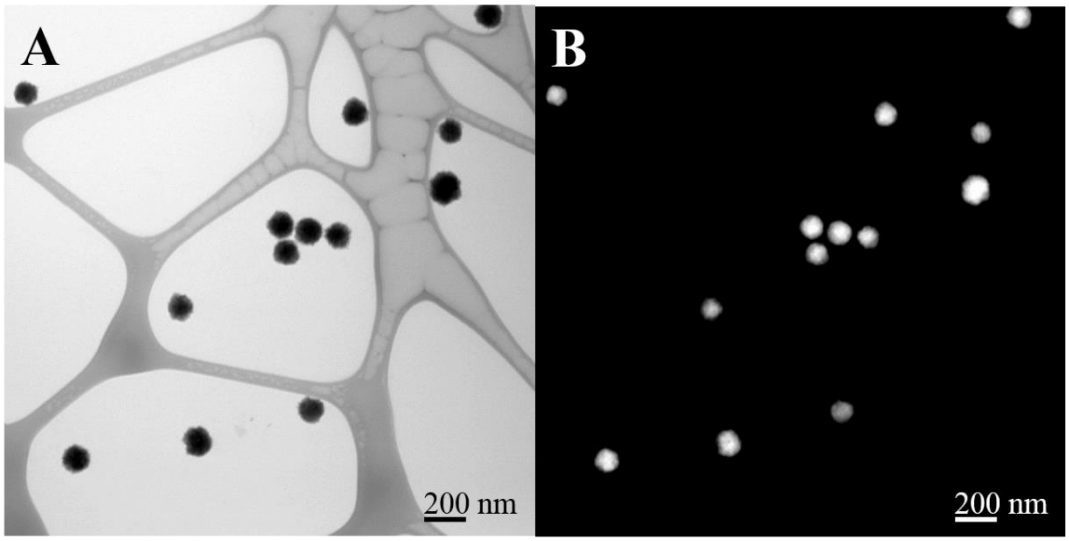

Figure 3-9. (a) Bright field- and (b) HAADF-STEM images of *D*-ZnS SPs.

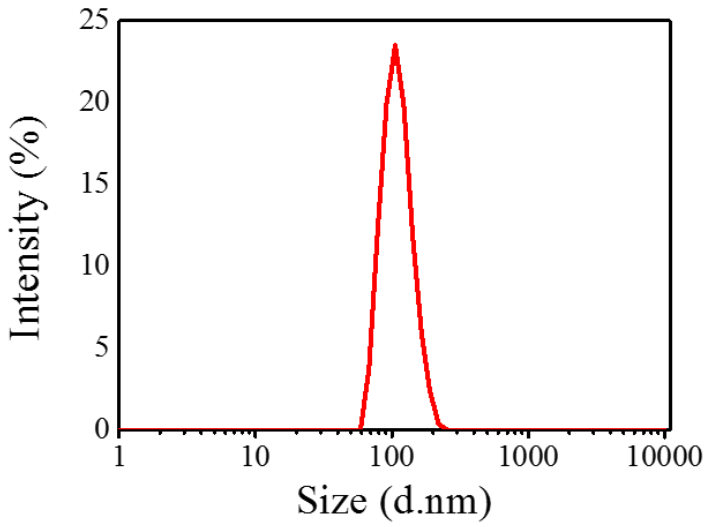

Figure 3-10. Size distribution of the self-assembled ZnS SPs by dynamic light scattering (DLS).

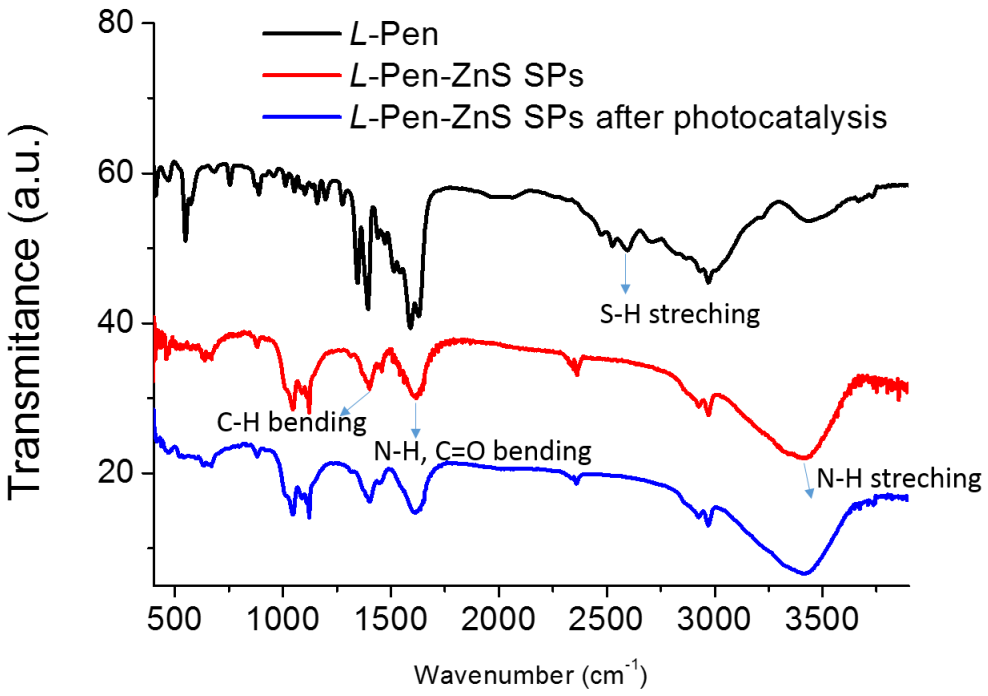

Figure 3-11. FTIR spectra (400-3900 cm^{-1}) of *L*-Pen, *L*-Pen-ZnS SPs, and *L*-Pen-ZnS SPs after photocatalysis.

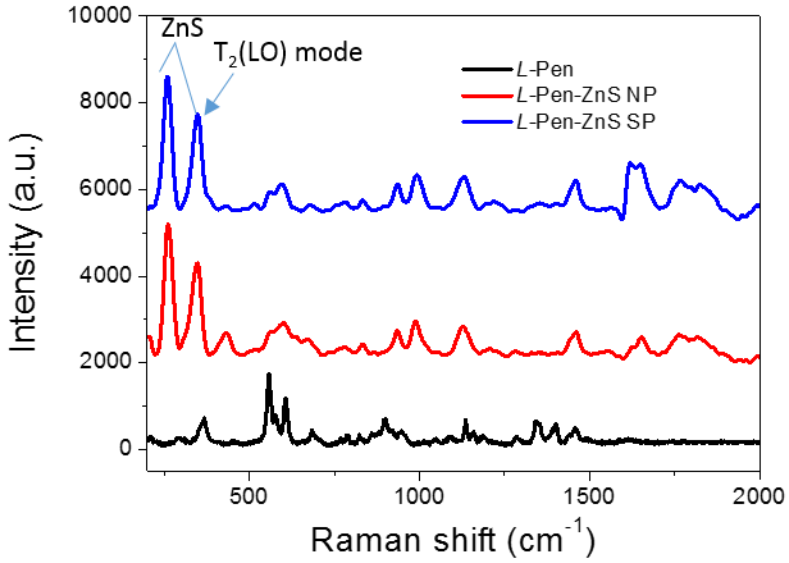

Figure 3-12. Raman spectra of *L*-Pen, *L*-Pen-ZnS NPs, and *L*-Pen-ZnS SPs.

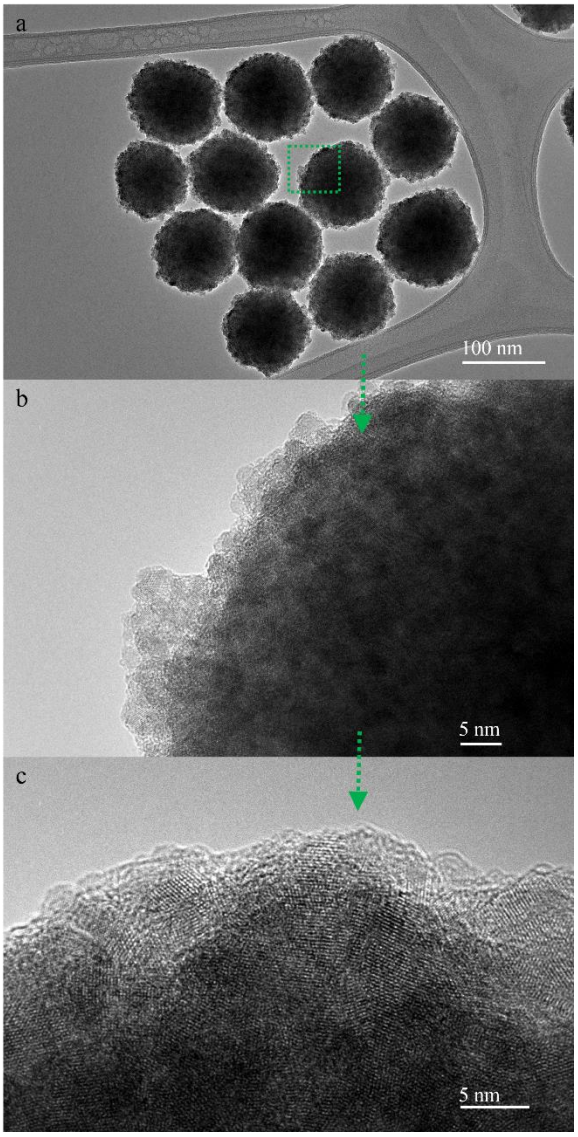

Figure 3-13. (a) TEM image of *L*-Pen-ZnS SPs. (b) Magnified TEM image (marked with dashed green square in Fig. S7a) of *L*-Pen-ZnS SP. (c) High resolution TEM image of the edge of *L*-Pen-ZnS SP.

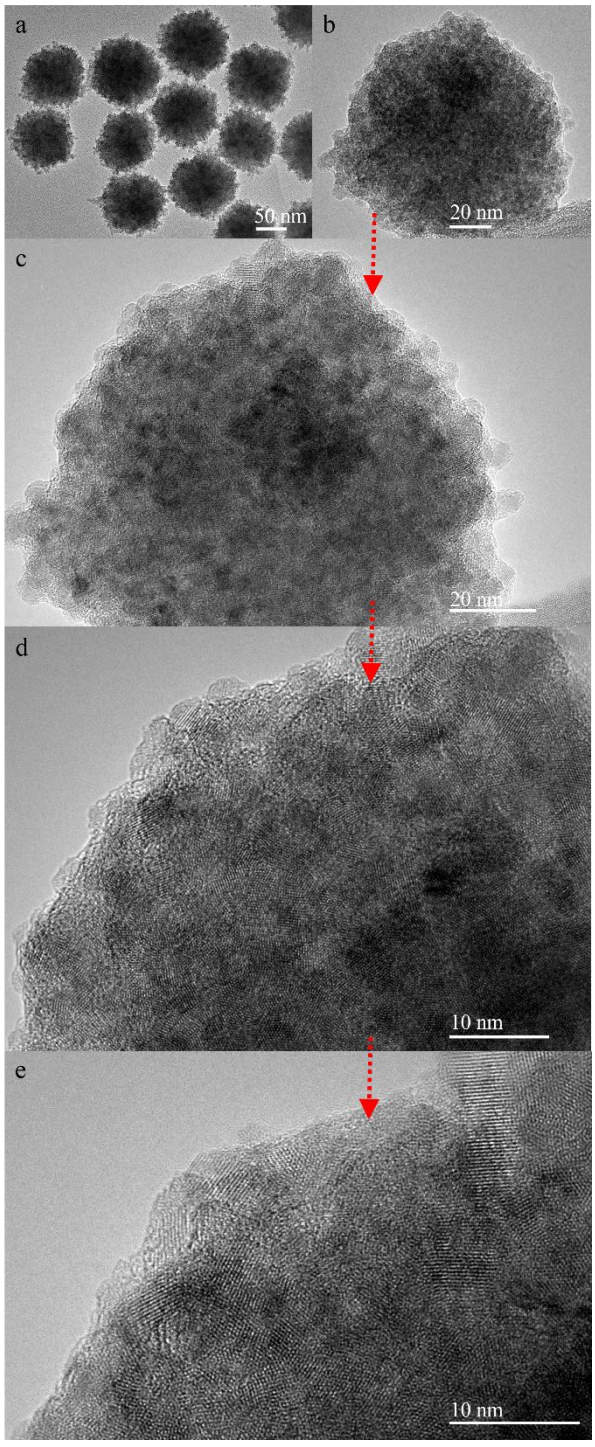

Figure 3-14. (a) TEM image of *D*-Pen-ZnS SPs. (b) TEM image of individual *D*-Pen-ZnS SPs. (c) High resolution TEM images of *D*-Pen-ZnS SPs. (d) and (e) Magnified TEM images of the edge of *D*-Pen-ZnS SP.

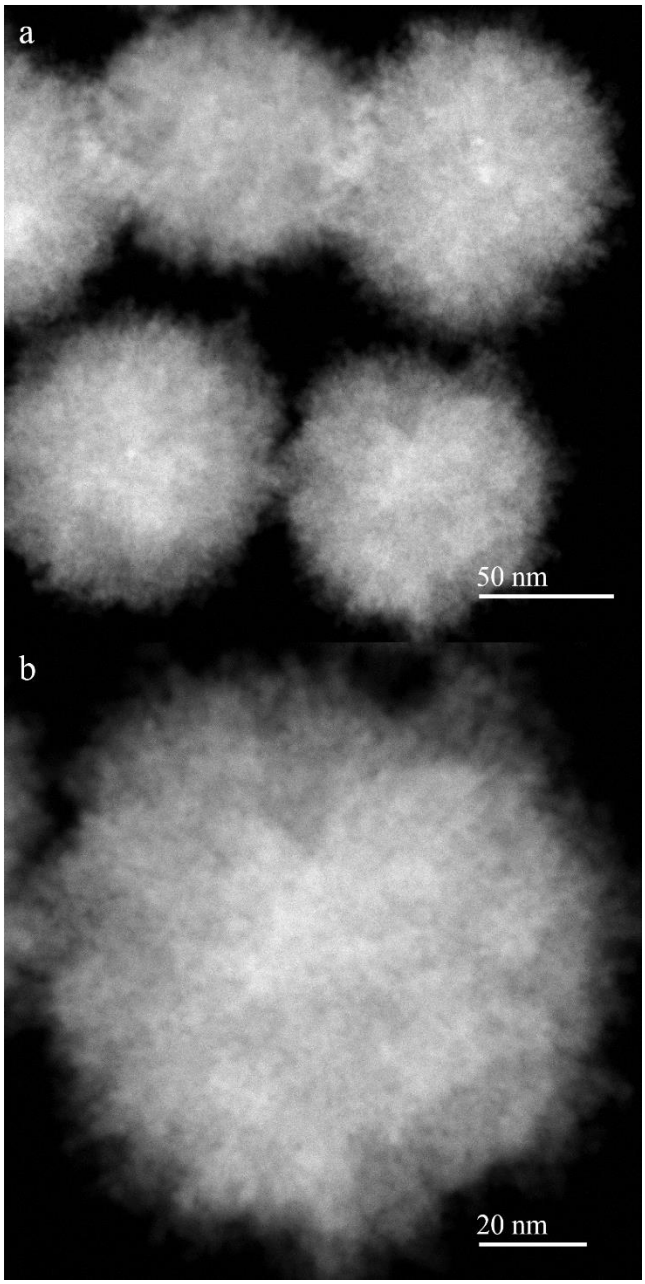

Figure 3-15. (a) HAADF-STEM images of *L*-Pen-ZnS SPs. (b) Magnified HAADF-STEM image of *L*-Pen-ZnS SP.

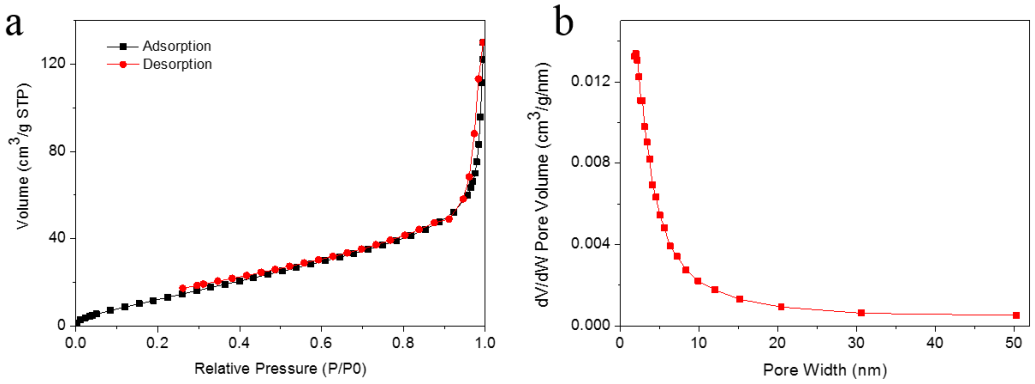

Figure 3-16. (a) N_2 adsorption-desorption isotherm and (b) corresponding pore size distribution of the *L*-Pen-ZnS SPs.

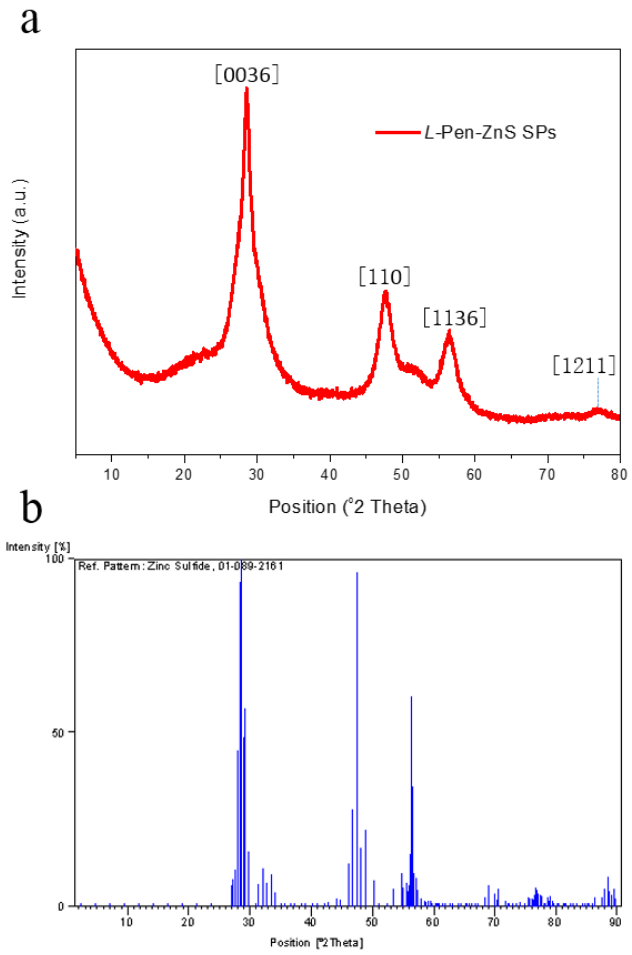

Figure 3-17 (a) XRD patterns of *L*-Pen-ZnS SPs. (b) The standard XRD spectra of ZnS with the PDF number of 01-089-2161.

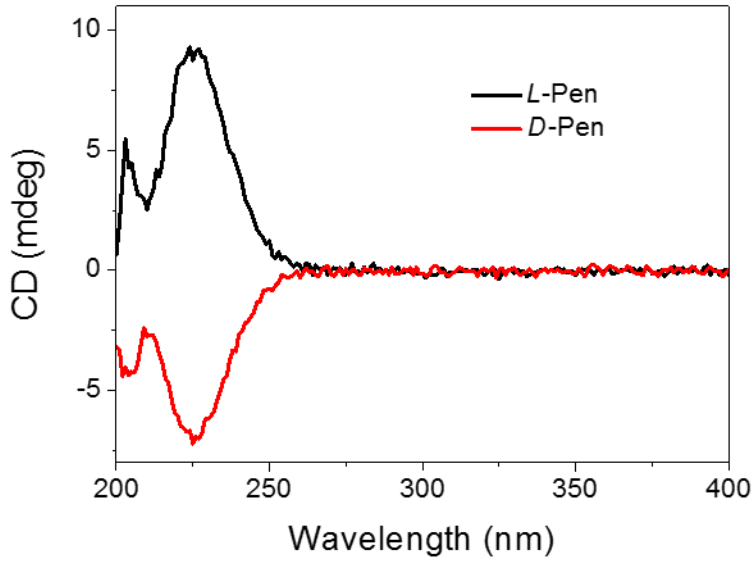

Figure 3-18. CD spectra of *L*- and *D*- Pen molecules.

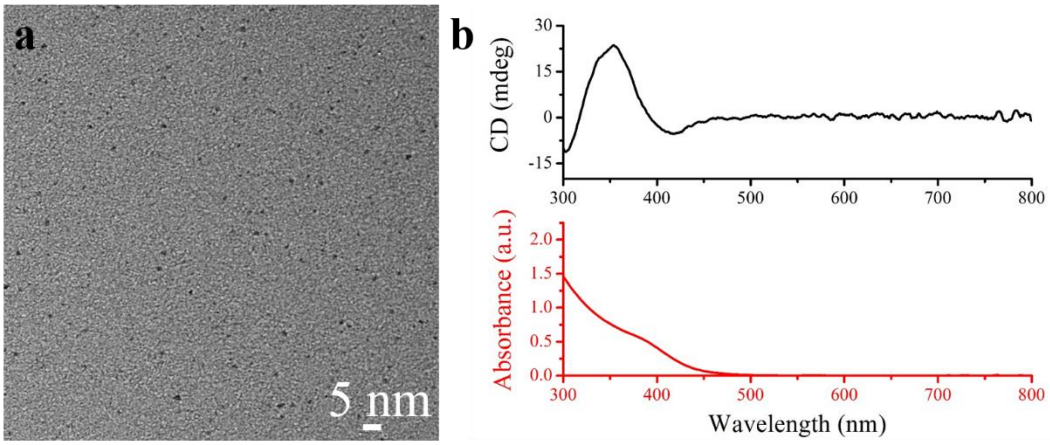

Figure 3-19. (a) TEM image and (b) CD and UV-Vis spectra of *L*-GSH-stabilized Au NPs.

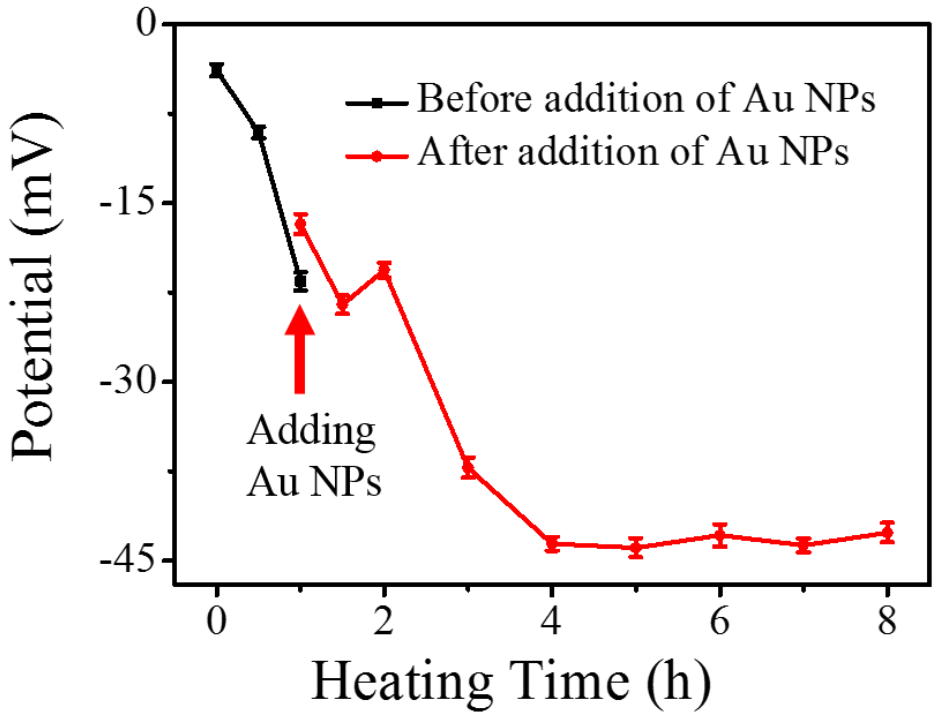

Figure 3-20. Temporal profile of ζ-potential for the assembly of chiral ZnS-Au SPs. NPs were added into the ZnS NP dispersion at 1 h heating time. The error bars represent the standard deviation of sample measurements.

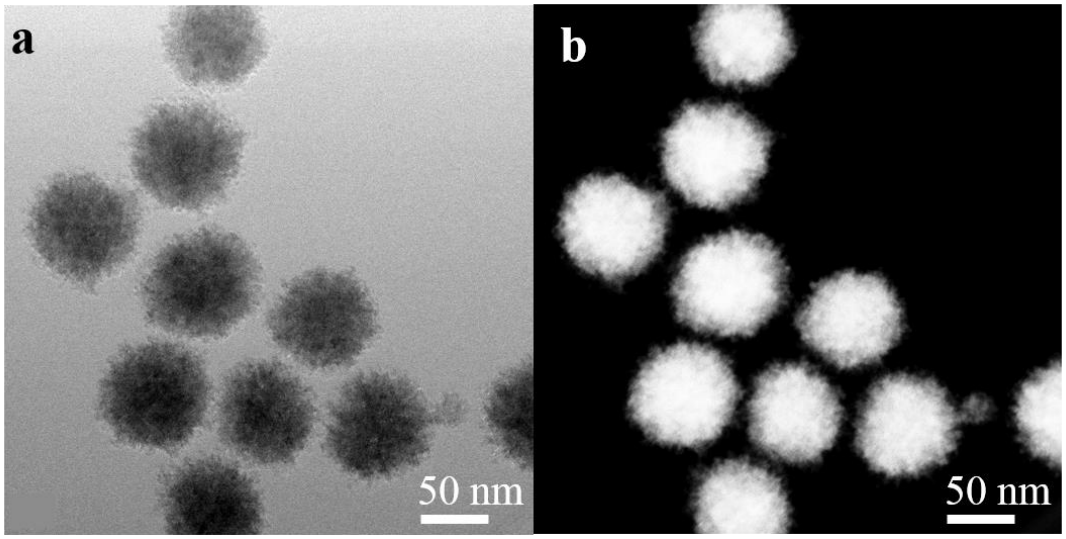

Figure 3-21. (a) Bright field- and (b) HAADF-STEM images of *L*-ZnS-Au SPs.

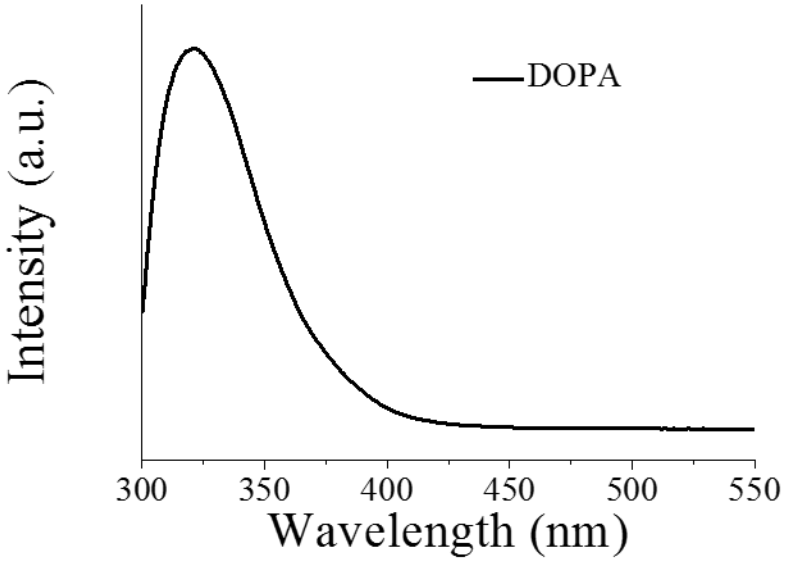

Figure 3-22 The fluorescence spectrum of DOPA.

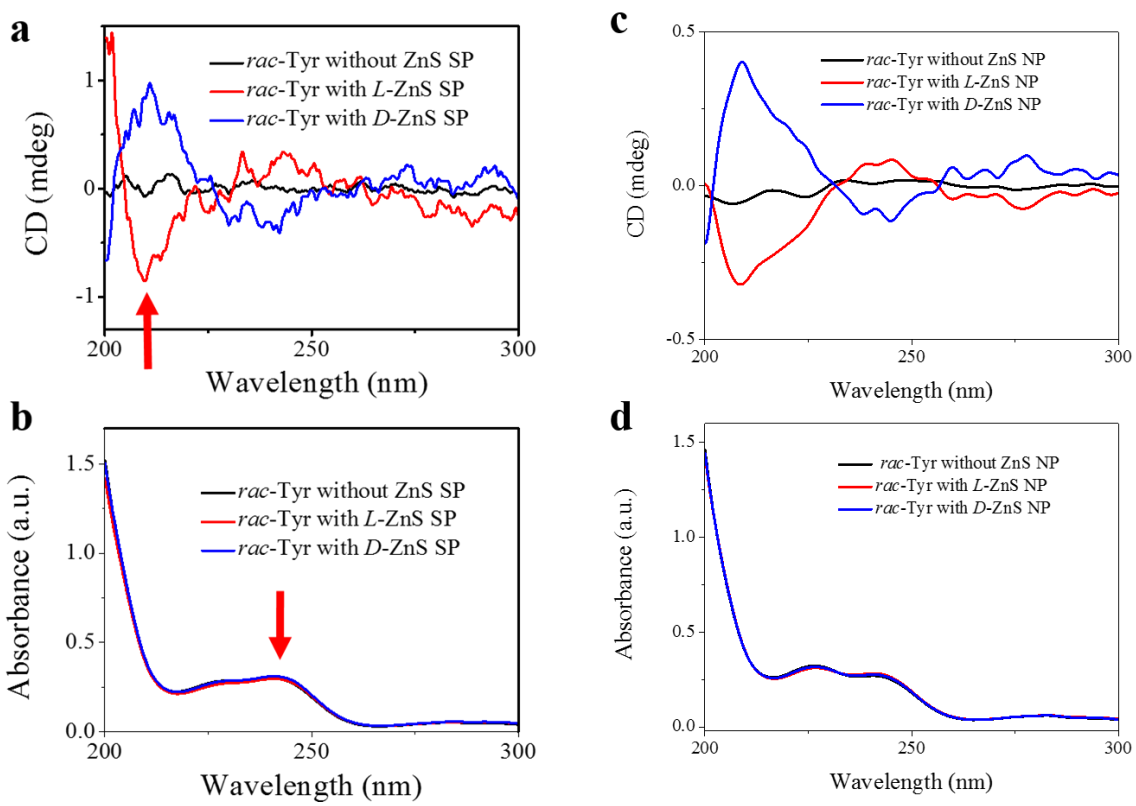

Figure 3-23. (a) CD and (b) UV-Vis spectra of *rac*-Tyr after incubation with, and without, *L*- and *D*-ZnS SPs. (c) CD and (d) UV-Vis spectra of *rac*-Tyr after incubation with, and without, *L*- and *D*-ZnS NPs. The CD spectra were measured for dispersions diluted to display identical UV-vis absorption at the CD peak of interests about 0.8 D.

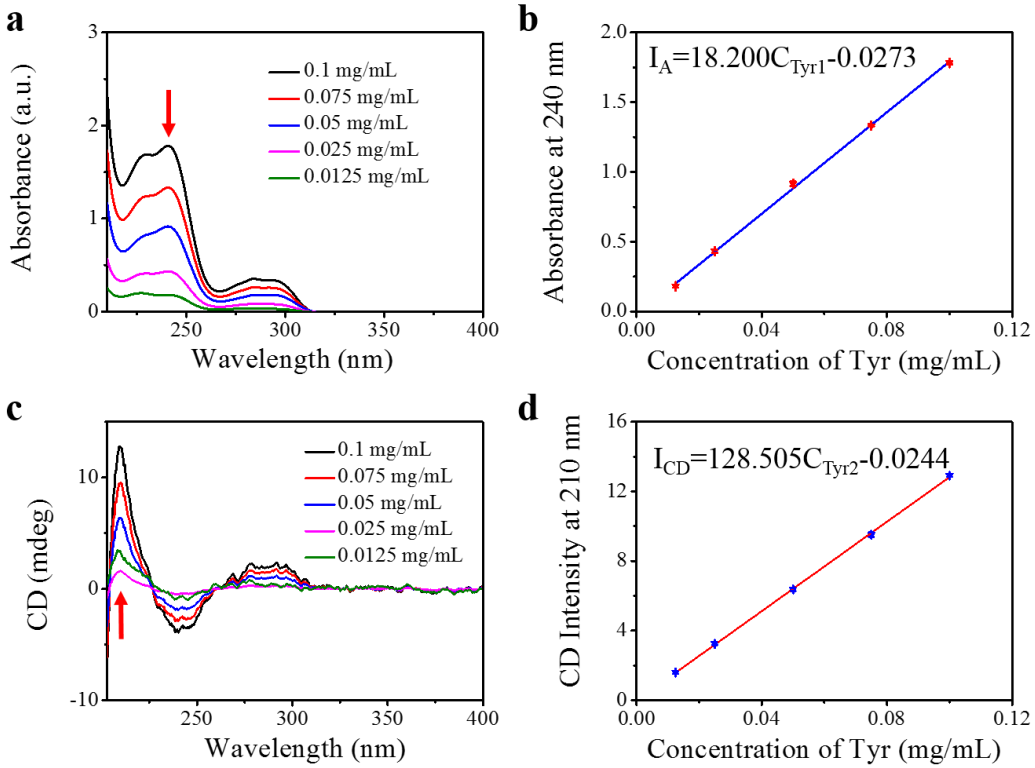

Figure 3-24. (a) UV-Vis absorption spectra of Tyr at different concentrations to establish the calibration equation for Tyr present in the supernatant. (b) The linear relationship between the absorption at 220 nm and the concentration of Tyr. (c) The CD spectra of Tyr with different concentrations. (d) The linear relationship between the CD amplitude at 210 nm and the concentration of Tyr. The error bars in b and d represent the standard deviation of sample measurements.

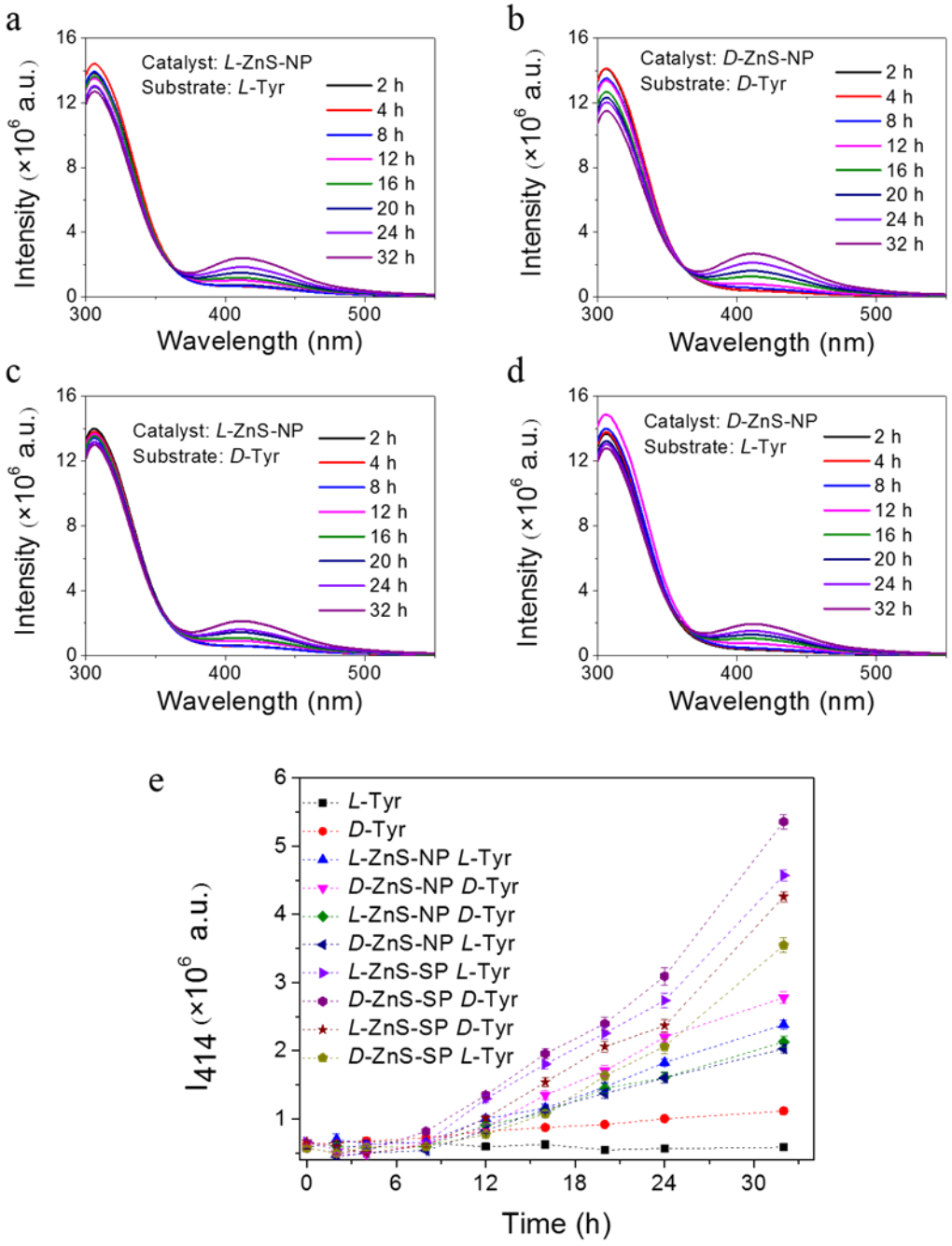

Figure 3-25. (a) L-Tyr with L-ZnS NPs. (b) D-Tyr with D-ZnS NPs. (c) L-Tyr with D-ZnS NPs. (d) D-Tyr with L-ZnS NPs. (e) The dependence of PL intensity at 414 nm on the photocatalytic reaction time with ZnS NPs and ZnS SPs of different chirality of the catalyst and the substrate. The error bars in e represent the standard deviation of sample measurements.

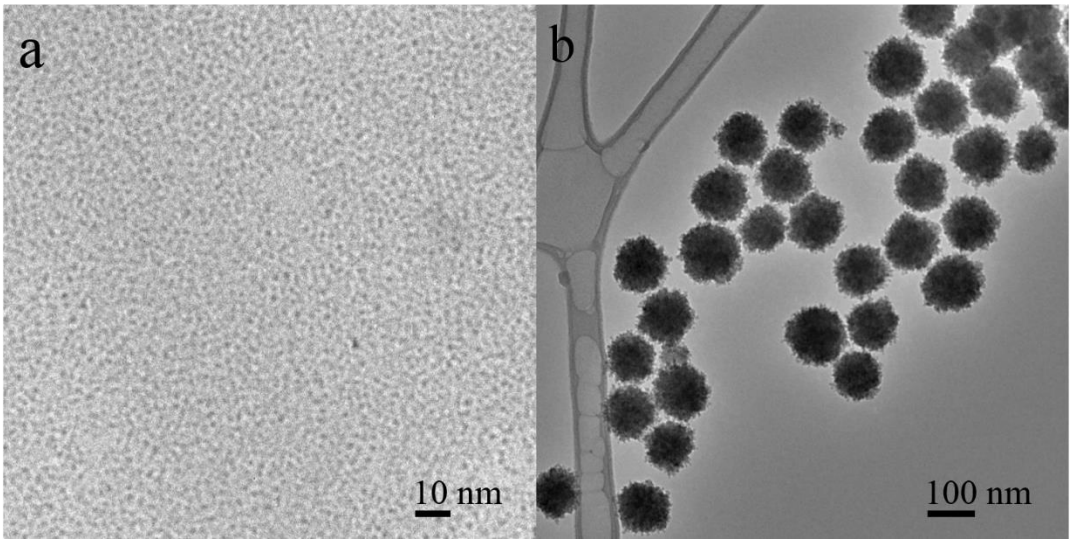

Figure 3-26. TEM images of (a) *L*-Pen-ZnS NPs and (b) *L*-Pen-ZnS SPs after photocatalysis.

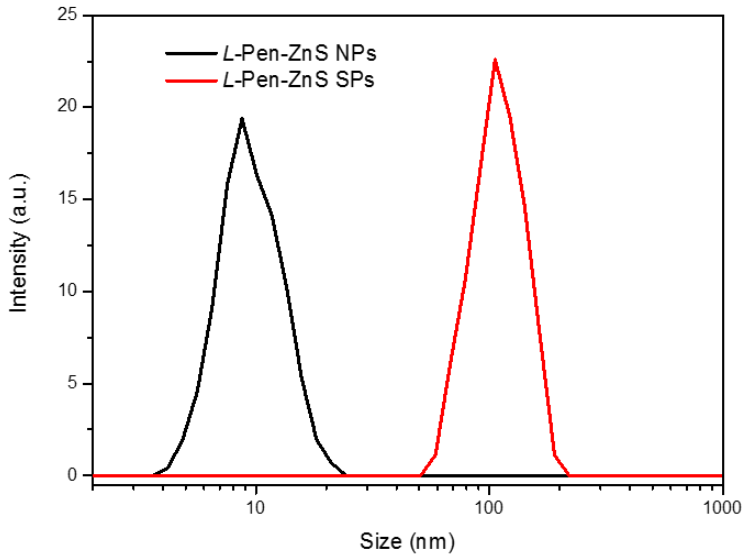

Figure 3-27. The size distribution of L-Pen-ZnS NPs and L-Pen-ZnS SPs after photocatalysis.

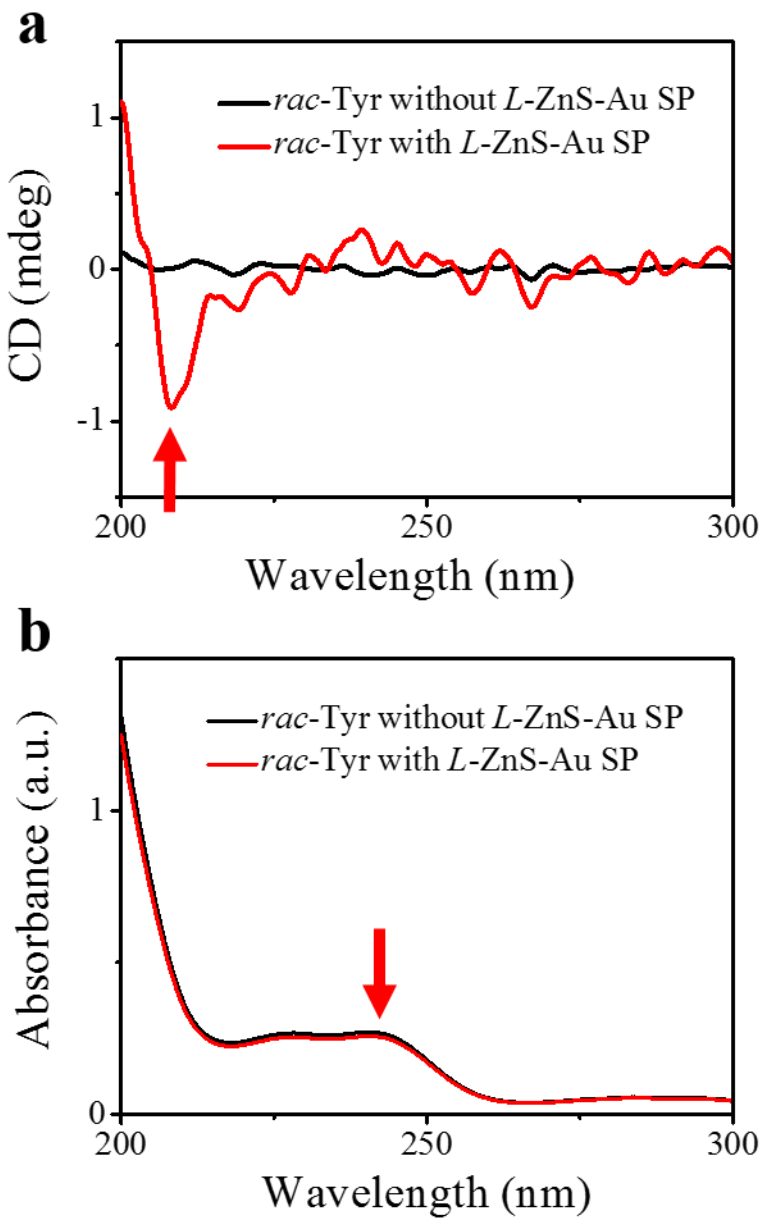

Figure 3-28. (a) CD and (b) UV-Vis spectra of *rac*-Tyr after incubation with and without *L*-ZnS-Au SPs. The CD spectra were measured for dispersions diluted to display identical UV-Vis absorption at the CD peak of interests about 0.8 D.

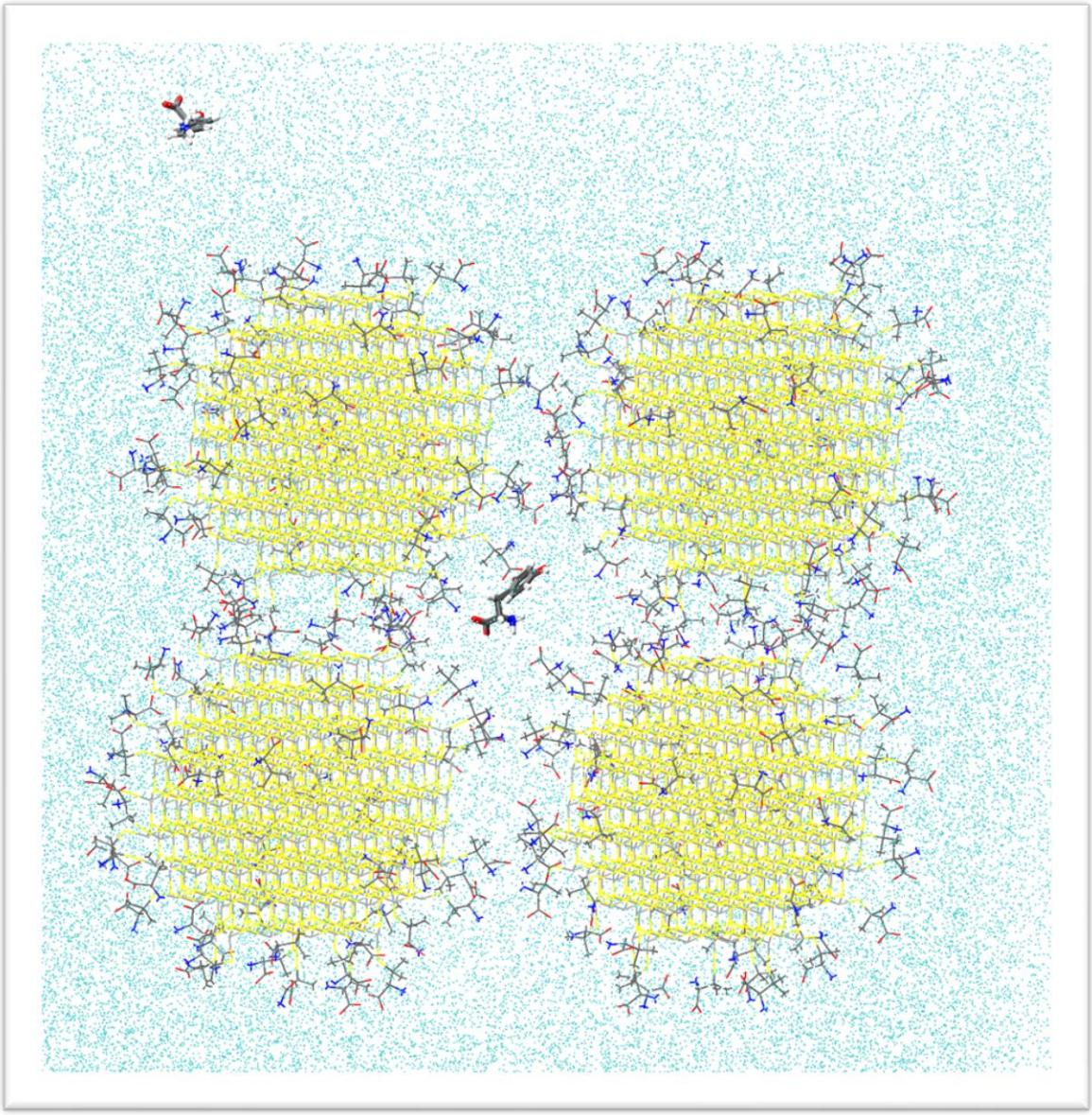

Figure 3-29. Snapshot of MD simulation

Chapter 4

Spiky Cadmium Sulfide Supraparticles

Naomi S. Ramesar, Mahshid Chekini, Ming Lei, and Nicholas A. Kotov

4.1 Abstract

Spiky cadmium sulfide (CdS) supraparticles (SPs) with tunable spike length and density were synthesized using a one-pot aqueous method at a relatively low temperature of 70 °C. The presented mechanism shows that the ethylenediamine concentration has an important role in the tunability of SP size and spike density. SPs demonstrated photoluminescence (PL) emission with both down- and up-conversion properties at an excitation λ range in UV (300 – 440 nm) and near-infrared (NIR) (700 – 940 nm), emitting from 450 – 500 nm. This conversion property was explored for the degradation of rhodamine B dye (RhB) under four illumination sources, ultraviolet (UV – 302 nm), visible (VIS), and IR, and Xenon lamp (UV to IR), with complete discoloration observed in all cases in the following order, Xenon (15 min) < VIS (20 min) < UV (30 min) < IR (24 h). The increased reaction rate may be attributed to both the collective and synergistic properties known for SPs, as well as the CdS unique down- and up-conversion properties.

4.2 Introduction

Self-assembly from molecular level to mesoscale is a well-accepted evolutionary step in biochemistry and formation of life.[147–153] This phenomenon may have played a role in the appearance of the first bimolecular building blocks as polypeptides and in higher-ordered supramolecular architectures such as folded proteins, RNA and DNA. Additionally, the self-assembled boundaries such as lipid bilayers instruct the formation of protocell towards to date living cells and organisms.[153,154]

The equivalent assembly phenomenon in inorganic nanomaterials has attracted attention due to immense potential as a stable and cost-effective biomimetic analog to biological components.[2,4,155–161] While key properties, such as composition, shape, and size, of nanoparticles (NPs) are important, their ability to self-assemble depends on their nano and micro-scale arrangement and geometry.[10] This is mainly due to the cumulative nature of self-assembled nanomaterials. Their properties originate from the collective response of their structural components which differ from the properties of individual NP and bulk assemblies.[6,95,162,163]

Self-assembly of inorganic NPs can lead to the formation of superstructures with different hierarchical shape and geometry.[155] For example it can result in one and two-dimensional assemblies such as linear chains,[164,165] sheets,[59] vesicles[166] and also three-dimensional supraparticles,[4,162,167] crystals,[168,169] and larger superlattices.[158,170]

Supraparticles (SPs) are one of the emerging types of engineered nanomaterials with well-defined shape and distinctive topological structure formed by self-limiting assemblies of individual small nanoparticles.[3,5,6,162,171,172] Their applications expand to various aspects of nanotechnology such as drug delivery and theranostic,[5,167,173,174] catalysis and energy applications,[8,172,175–177] and optics.[178]

Formation of SPs can be accomplished via two distinctive routes. For the first type, NP synthesis and self-assembly take place in two separate steps, while in the second type the NP nucleation, growth and self-assembly occurs continuously. The first type is mainly suitable for functional SP formation when different components are involved, for example when different types of nanoparticles are used[3,173] or when a combination of biological and inorganic materials self-assembles into composite superparticles.[4,5] In general, NP attachment can be influenced by different components in the dispersion media such as concentration, size, stabilizing ligands, solvent, ionic strength, pH, temperature, etc.[19] Since the synthesis and self-assembling stages are separate, the first type can be used for various types of nanoparticles. There is more freedom in adjusting the physio-chemical conditions (composition, concentration, temperature) under which the self-assembling process is taking place.

The second type has more experimental restrictions, but are important since it is analogous to its natural equivalent, bio-mineralization.[23] There are limited examples of SP formation in NP synthesizing medium[3,20,21] which highlights the lack of attention to this process despite the fact that it is an intermediate stage in the formation of many nanocrystalline structures via crystallographic fusion.[22,23] Inorganic nanomaterials oriented attachment is observed in different experimental conditions.[23,165,179,180] and the process is more favorable at a relatively low temperatures. It can be remotely controlled by applying changes in the chemical composition of the synthesis medium for engineering nanostructures with different architectures such as spherical assemblies, sheets, rods, wires and helices.[22,23]

For the fabrication of metal sulfide nanostructures such as CdS solvothermal and some hydrothermal methods are widely used.[181–183] The influence of synthetic solvothermal conditions on the evolution of CdS nanostructures and their properties, particularly for application in

photocatalytic hydrogen production, has been extensively studied[181,182,184–186] but there are limited reports on low-temperature (below 100°C) aqueous-based synthesis of CdS nanostructures.[187]

As a semiconductor, CdS-based nanostructures are heavily used for photocatalytic applications, utilizing a small portion of the light spectrum. An area of interest is broadening the range of absorption spectrum, specifically to the near-infrared (NIR) region to benefit from up-conversion properties.[188] Up-conversion is an anti-Stokes luminescence mechanism where materials sequentially adsorb two or more low energy photons and emit at shorter wavelengths.[188,189] Although inorganic nanocrystals are extensively employed for infrared-to-visible up-conversion purposes[189], typically, the up-conversion is achieved by incorporation of an IR-responsive compound as a sensitizer, like lanthanide, into the NP system.[188] Recently, the efficient up-conversion property of CdS nanobelts was recognized and attributed to efficient exciton-longitudinal optical phonon coupling.[190] Due to their ability to decrease light trapping, the CdS nanobelts were utilized for optical cooling in lasers systems, showing excellent efficiency.[191] The up-conversion properties displayed by CdS would also be exciting for photocatalytic application, effectively converting NIR to VIS. Combined with the collective and synergistic properties of SP assemblies, it would be appealing to explore the up-conversion potential in SP systems.

In this work we developed a facile one-pot aqueous-based synthesis method for fabrication of spiky CdS SPs at a relatively low temperature (70 °C), with good dispersion stability and promising up-conversion potential without the addition of a sensitizer. The synthesis procedure presents flexibility in control of shape and size by tuning the amount of ethylenediamine (En) in the reaction. PL spectra show emission independent down-and up-conversion which can open a venue for light manipulation, therefore to better evaluate the light-matter interaction in the system,

the SPs photocatalytic ability to degrade rhodamine B (RhB) dye was studied using four different light illumination sources, ultraviolet (UV), visible (VIS), IR, and Xenon lamp to benefit from both down-and up-conversion of SPs.

4.3 Materials and Methods

Synthesis of cadmium sulfide SPs: A facile synthesis procedure was developed for fabrication of spiky cadmium sulfide SPs which can be extended for the fabrication of zinc sulfide SPs. Cadmium perchlorate hexahydrate ($CdCl_2H_{12}O_{14}$, Alfa Aesar™) was used as a cadmium source and amino acid *L*-cysteine hydrochloride monohydrate (or *D*-Cysteine hydrochloride monohydrate and *L/D*-glutathione reduced) (Sigma-Aldrich) was used both as a sulfur source and stabilizing ligand. 40 mL deionized water, 0.5 mM of cadmium perchlorate hexahydrate, 1.3 mM of *L*-Cysteine hydrochloride monohydrate and 4 mL ethylenediamine was combined. The solution was left at 70 °C for two days, followed by aging in dark and at room temperature for two days.

Rhodamine B Photocatalysis experiment: 1 mg/mL of *L*-Cys CdS NP was added to rhodamine B dye (12 μM). The solution was sonicated for complete dispersion of CdS NPs and allowed to stir for 20 minutes prior to illumination. A Xenon lamp was utilized as the illumination source with respective filters for IR illumination. For the UV illumination, a 50 W UVP lamp centered at 302 nm was used.

Characterization Methods: Transmission electron microscopy (TEM) and high-resolution transmission electron microscopy (HRTEM) observations were performed using a JEOL-3011 microscope with an accelerating voltage of 200 kV. Scanning electron microscopy (SEM) was

performed on an FEI Nova system. X-ray diffraction (XRD) studies were carried out at room temperature on a Rigaku Rotating Anode X-ray Diffractometer using Cu Kα radiation (1.54 Å).

HPLC-MS equipped with an electrospray ionization source was used at a 50:50 water with 0.1 % trifluoroacetic acid (TFA): acetonitrile with 0.1 % TFA at a 0.5 mL/min flow rate for 10 minutes with a column temperature of 40 °C. Diode array detection was set to collect data at 500 and 544 nm to track the RhB and the product species.

4.4 Results and Discussion

Spiky chiral SPs of CdS were obtained in the presence of ethylenediamine (En) and (*L* or *D*-) cysteine amino acid, which functioned as both the ligand and sulfur source. Depending on the pH of the solution, the thiol group in cysteine can readily coordinate with metal ions, such as Cd, to form $[Cd(Cys)_2]^{2+}$ complexes. The $[Cd(Cys)_2]^{2+}$ complex leads to the formation of CdS nuclei, which can further grow into small CdS nanoparticles. The solution turns turbid in 8 h and becomes a pale-yellow color, which deepens with time. Under this condition, small nanoparticles of cadmium sulfide form and self-assemble into spiky (needle-like) nanostructures. NP formation and assembly continues up to 48 h at 70°C. This assembly process continues at room temperature for up to two days leading to more dense (fibrous-shaped) cadmium sulfide SPs. A proposed scheme for the assembly process is presented in **Figure 4-1A** and further supported by high-resolution transmission electron microscopy (HRTEM) images (**Figure 4-1B**). Here, the transition from individual NPs to nanowires, and finally aggregation of wires to form uniform fibrous assemblies is observed.

HRTEM images correspond to SPs (d_{TEM} = 196 ± 36 nm) synthesized using 0.5 mM of cadmium perchlorate in the presence of 4 mL En and 1.3 mM cysteine (**Figure 4-2A**) and confirms the composition of individual NPs (2-4 nm) within the larger SP (**Figure 4-2B**). Further analysis

by scanning TEM (STEM) confirms the arrangement of individual NPs rather than crystalline nanowires and identifies the flexibility in the spike structure as the assembled nanowires overlay each other in a twisted configuration (**Figure 4-7**). Estimated d-spacing values by lattice fringe measurements are in close agreement with the expected values of 3.5784, 3.3670 and 3.1600 Å corresponding to (100), (002) and (101) planes of hexagonal phase CdS (**Figure 4-2B**). The electron diffraction pattern shows the polycrystalline nature of the SPs with an average d-spacing of 3.58 Å, corresponding to (100) plane (**Figure 4-2B, inset**). Powder X-ray diffraction (XRD) pattern (**Figure 4-2D**) shows diffraction peaks at 24.8, 26.4 and 28.2 degrees corresponding to (100), (002) and (101) reflection planes in the hexagonal-phase respectively. The deviation of peak intensity from reference bulk CdS (International Centre for Diffraction Data (ICDD) Reference code 03-065-3414) confirm the formation of strong anisotropic and directional growth of nanocrystallites along the 002 direction. The calculated crystallite size using Scherrer equation for (100) reflection is 4.47 nm.

Fluorescent spectrum was acquired for particles using an excitation wavelength of 420 nm, corresponding to maximum UV absorption, with emission from 450 – 500 nm (**Figure 4-2E**). The spectrum exhibited a maximum peak at 470 nm, with two shoulder peaks centered at 485 and 495 nm. Tracking PL spectra throughout the synthesis from day 1 to 4 reveals three emission peaks present from day 1 (**Figure 4-8**), suggesting the additional peaks may be different emissive states, such as ligand to surface transition associated with intermediate complexes between Cd, En, and Cys. The incorporated chiral ligand (*L*-/*D*-Cys) at nanoparticles surface induce chirality into electronic absorption band of CdS SPs (**Figure 4-2F**). Therefore, using *L*- and *D*-Cys can result in SPs with mirror image circular dichroism (CD) bands. The presented CD spectra in **Figure 4-2F**

shows a relatively broadband in 280-500 nm with a sharp band about 450 nm which coincides with the excitonic absorption of CdS SPs.

To better understand the synthesis and assembly mechanism, the role of ethylenediamine was studied. As a bidentate ligand it strongly coordinates with Cd^{2+} ions[192] to form a stable complex, $[Cd(en)_2]^{2+}$, which affects the accessibility of Cd^{2+} ions in the precursor, to control the nucleation process, unlike hydrothermal synthesis where the complex decomposition at high temperatures results in nanoparticle growth.[184] In this study En regulates the Cd^{2+} ion transfer and release process and as a result, changes the dynamics of nanoparticle nucleation and growth.

An extended analysis was performed by changing the amount of En from 0 to 4 mL, while maintaining a consistent pH by the addition of 1 M NaOH from 4 to 0 mL for Sample 1 to 5, respectively. SP properties, including size, shape, and charge were observed using HRTEM, DLS, and zeta potential measurements (**Figure 4-3**), respectively. A closer look at TEM images (**Figure 4-3A**) shows that the presence of En leads to the formation of dense needle-like structures. The lack of En (sample 1) leads to slower nucleation, growth, and self-assembly of nanoparticles, lending to smaller, less spiky SPs. While higher En amounts not only increases the density of spikes but also the overall size of the SPs. For example, sample 5, which was synthesized with only En and no NaOH, shows much denser packing of needle-like assemblies into the final spiky SP. When 10 mL of En was added to the synthesis solution, the SPs became larger (435 ± 76 nm), as expected, and approach a spherical shape as the surface spikes appear shorter due to dense packing of needle-like assemblies **(Figure 4-9A-B**). A close view of the spikes maintains the suggestion that needle-like structures are densely packed (**Figure 4-9C**).

As observed in TEM and DLS (**Figure 4-3B**) the size of the assemblies increases as the amount of En increases. Although the trend is the same, the measured DLS values are larger than

the SP sizes observed on TEM images. This is due to the hydrodynamic diameter measured by DLS technique. The aging time does not appear to have a significant role on the overall size of SPs, but TEM micrographs show that there is a change in the shape of needle-like structures and 'spikiness' of SPs during this stage. Thus, SPs appear to go through a reorganization step, which is monitored by CD, UV-Vis, zeta potential, and PL data **(Figure 4-8;Figure 4-11; Figure 4-12; Figure 4-13**) and show no significant changes in respective spectrums during aging. It is proposed that the reorganization in this step follows an Oswald ripening mechanism, initial surface spikes, which were randomly organized, are able to detach and join a different assembly with a preferential 002 crystal orientation, dictating the oriented growth.[193] The absolute value of the zeta potential for different SP samples follows the same trend during the synthesis (**Figure 4-3C**). Except for sample 4, surface features and spikes collapse at day two but reorganizes during the aging process. Overall, we can see the system eventually approach a lower charge value over the four-day period. As SP assemblies are dynamic, the reorganization throughout the particle growth and assembly stages are expected.[4,194]

Self-assembly by oriented attachment can be derived by decreasing the ligand density on nanocrystal surface,[59] and through the presence of small molecules[22], therefore it can be deduced that the self-assembly of SPs is induced by surface attachment of En, assisted by cysteine.[195] In sample 2 to 5, it is presumed that NPs are capped by both Cys and En because of their strong affinity to the Cd surface atoms, and the nature of their interactions are different for different atomic facets of CdS nanocrystals.[196] En has also been widely used as a solvent for the 1D solvothermal synthesis of CdS nanostructures.[181,184,186,192,197–199] due to its low dielectric property.[192] Therefore, this strongly suggests that it facilitates small nanoparticles oriented-

attachment and self-assembly into needle-like structures and later to higher level assemblies of spiky SPs.

Hence, is it proposed that SP formation is as follows; first, nucleation and formation of small NPs and their loose aggregation into SPs. Second, directional self-assembly of newly synthesized NPs in an oriented fashion along the 002 direction into needle-like structures on top of the SP core. And lastly, the accumulation and formation of denser SPs which varies with different amounts of En.

Up-conversion and catalytic ability

Upon further analysis, SPs revealed unique down- and up- conversion properties without the addition of sensitizers (**Figure 4-4**). SPs were excited from 300 – 440 nm (UV range and slight blue) (**Figure 4-4A**) and 700 – 940 nm(**Figure 4-4B**). Interestingly, independent of the excitation wavelength, all emission occurred from 450 – 500 nm, with a maximum peak at 470 nm. The emission intensities for UV excitation wavelengths are an order of magnitude higher than the NIR excitation. To the best of our knowledge, one other study on carbon quantum dots reported a similar emission independent PL phenomena.[200] In CdS, highly efficient photoluminescence (PL) up-conversion has been attributed to efficient exciton–longitudinal optical phonon coupling[190] but mainly evaluated as a semiconductor material for laser cooling.[191]

To explore the full extent of the absorption properties of SPs, the PL, down- and up-conversion property, was investigated for the degradation of RhB dye under four illumination sources (**Figure 4-5**). The complete degradation of RhB was observed for all three sources with degradation rates in the following order: Xenon (15 min) < VIS (20 min) < UV (40 min) < IR (24 h) (**Figure 4-5A-B).** This was anticipated as CdS SPs peak absorption occurs at 420 nm and is part

of the VIS region. The Xenon lamp source emit the entire electromagnetic range from UV to IR and results in the fastest photocatalytic rate. This may be attributed to a collective effect exhibited by particles, utilizing down- and up-conversion properties of CdS. RhB alone did not show any discoloration under any illumination condition, suggesting that degradation occurs due to the generate of electron-hole pairs in CdS SPs to create radical species, targeting RhB. Analysis of UV-Vis (**Figure 4-5A)** and PL data (**Figure 4-5C; Figure 4-6)** shows the appearance of a new peak centered at 496 nm as the RhB peak (centered at 544 nm) decreases for all illumination sources except UV. Further evaluation of the PL data (**Figure 4-5C)** shows strong development of a new peak with a gradual blue shift from time 0 to 15 min. The color change and fluorescence are visually observable, transitioning from a reddish-pink color to orange, then yellow and finally a strong green fluorescence (**Figure 4-5C inset**). Similar to the degradation rate at 554 nm, the Xenon lamp RhB sample shows the most rapid and consistent increase at 496 nm, while the VIS and IR samples increase initially but eventually plateaus (**Figure 4-10**). While, for UV, there is a decrease consistent with the overall decrease of RhB.

High pressure liquid chromatography with mass spectrometry (HPLC-MS) was performed to analyze the origin of the new peak for the final sample (**Figure 4-5D**). At four min retention time, the HPLC shows a strong signal at 500 nm and MS outputs a m/z of 331 (**Figure 4-5D, inset**). A m/z of 331 suggests that RhB goes through a de-ethylation process,[201] while the strong green fluorescence suggest the production of a rhodamine derivative, specifically rhodamine123 (Rh123) compound. VIS, IR, and Xenon illumination of SPs all result in the formation of green, fluorescent compound from RhB, while UV illumination leads to degradation of RhB without any evidence of the Rh123 derivative. This suggest that photocatalytic degradation of RhB take different route under different light illumination, while under UV RhB is completely mineralized

or form non-emissive intermediate product without any strong optical features, under VIS, IR, and Xenon lamp illuminations it forms a stable intermediate which is recognized as an Rh123 derivative. The presented data suggest the intensity and wavelength of the illumination source has an impact on the rate and selectivity of the product.

4.5 Conclusions

A facile and tunable synthesis and self-assembly method was presented for spiky cadmium sulfide SPs. The variation in ethylenediamine concentrations lead to the development of more needle-like structures which sequentially aggregated to create dense SP assemblies. SPs exhibited unique PL, showing both down and up-conversion properties with an excitation independent emission spectrum. This property was utilized to evaluate how different illumination sources impact the overall rate and products of a given reaction. Xenon lamp showed the best performance with complete de-ethylation in 15 min to form a rhodamine derivative with a strong green fluorescence. The rates vary for other illumination sources, with UV showing no production of the new rhodamine derivative.

4.6 Figures

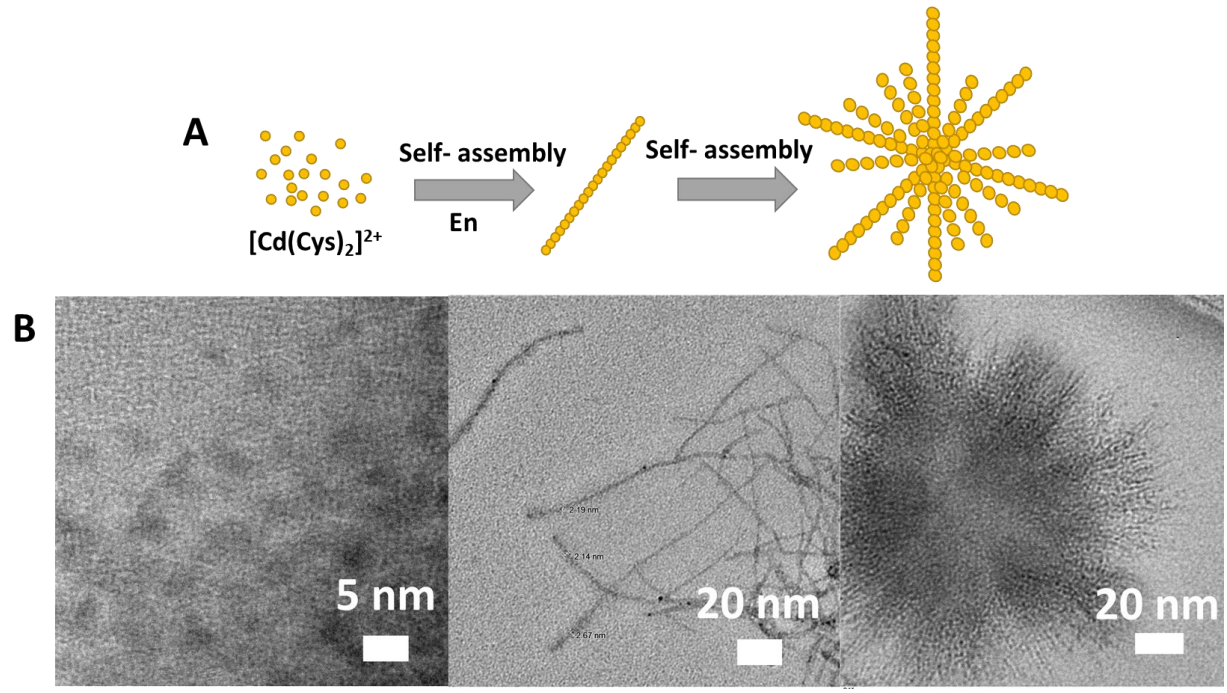

Figure 4-1. (A) Proposed scheme of CdS SP formation; (B) HRTEM of SP formation, from NPs to nanowires and lastly, loosely packed assemblies.

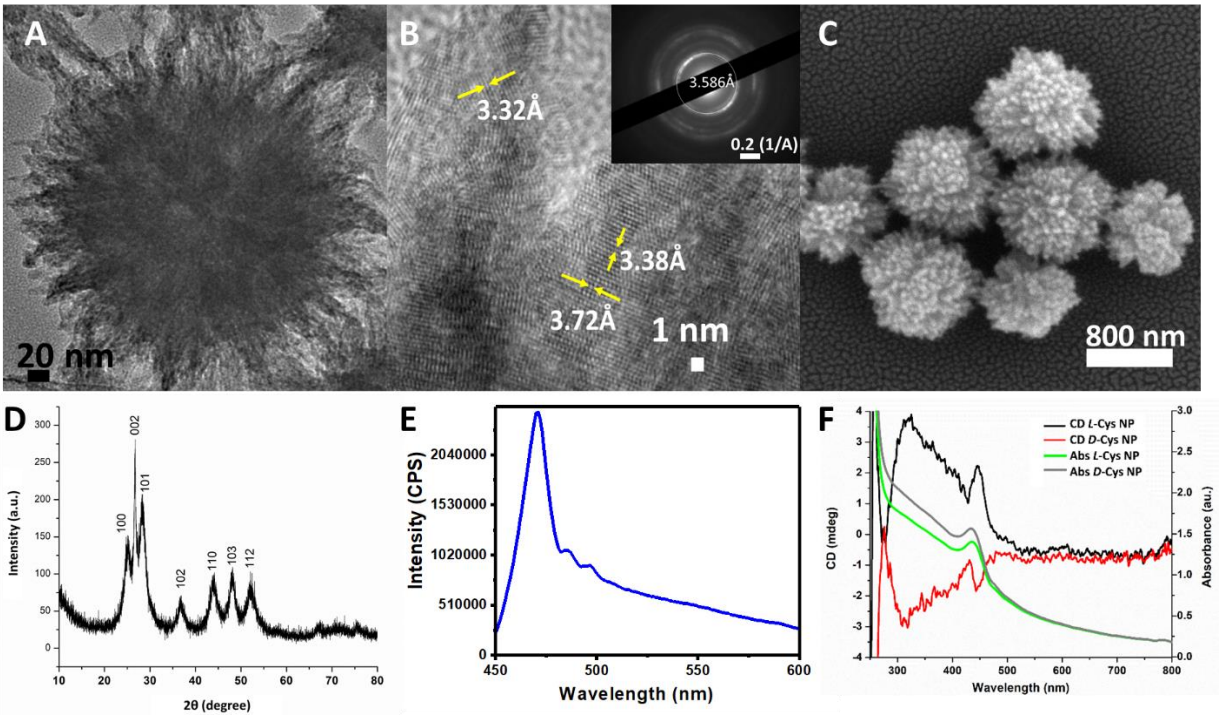

Figure 4-2. Characterization of L-cysteine CdS. HRTEM of (A) individual SP, (B) spikes with lattice fringes including inset with diffraction pattern; (C) SEM; (D) X-ray diffraction pattern; and (E) CD and UV-Vis spectra of L- and D-Cys CdS SPs.

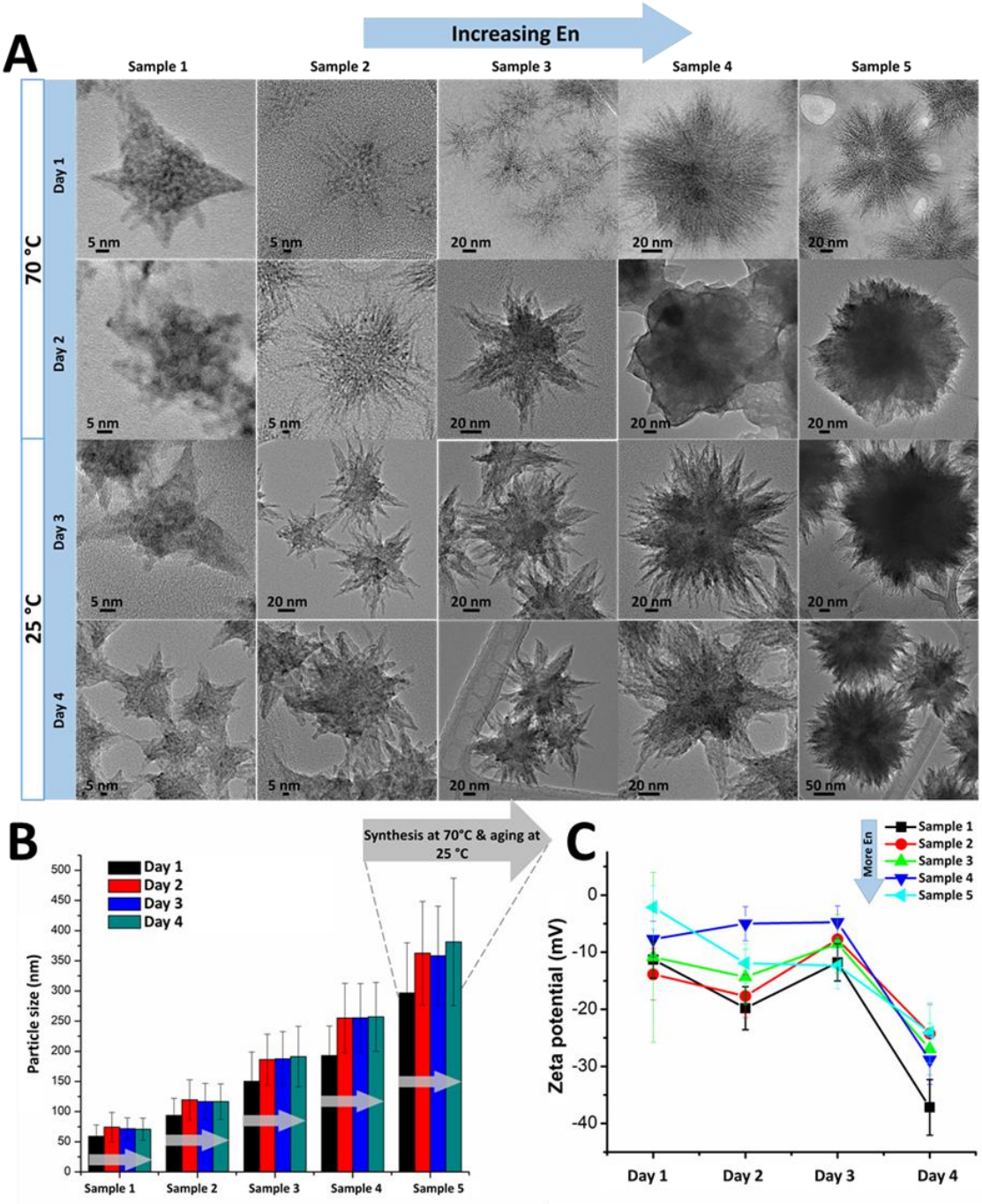

Figure 4-3. Variation in En concentration and aging. Experimental condition for different samples of L-Cys CdS nanoparticles synthesized using different amount of ethylenediamine (En) and NaOH. (A) HRTEM micrographs (B) DLS and (C) zeta potential.

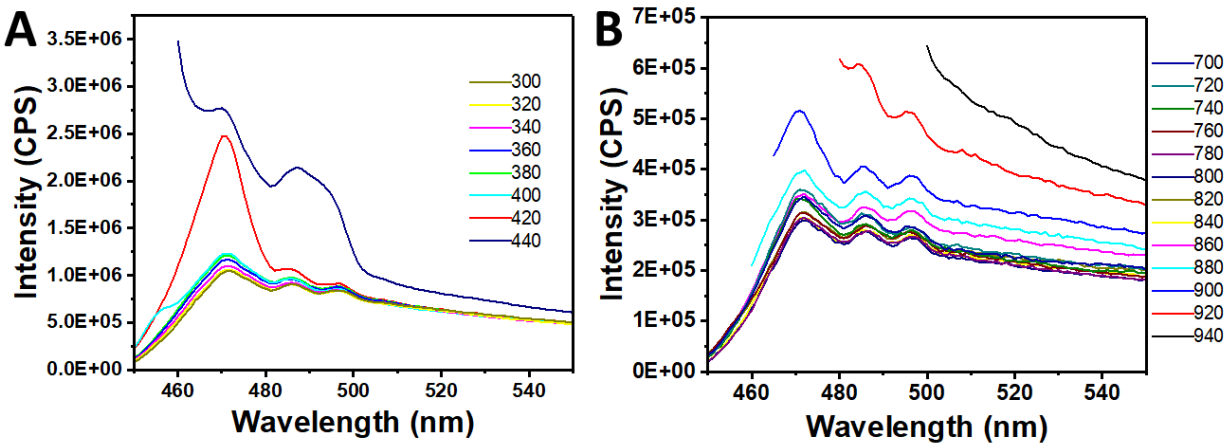

Figure 4-4. Fluorescence spectra for CdS SPs with (A)excitation wavelength from 300 to 440 nm and (B) excitation from 700 to 940 nm.

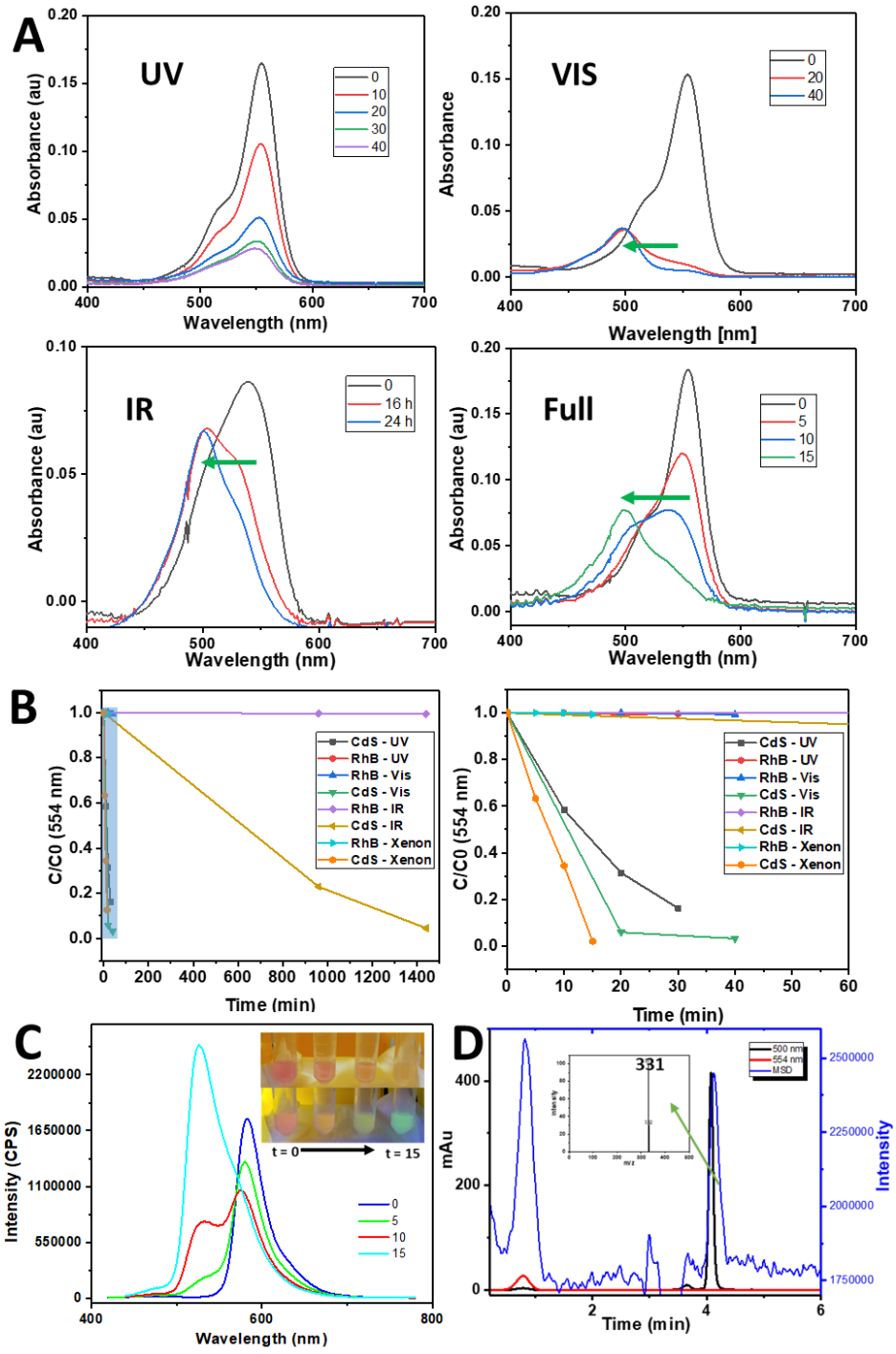

Figure 4-5. Degradation of RhB using UV, VIS, IR, and full Xenon illumination sources (A) UV-Vis reaction spectra for each illumination source; (B) C/C0 for RhB and RhB with SPs under each illumination with an additional graph zooming in on blue highlighted box; (C) fluorescent spectra from reaction with Xenon illumination with inset of reaction solution from 0 – 15 mins under white light vs UV and (D) HPLC – MS data of 15 min reaction time sample, with inset of m/z.

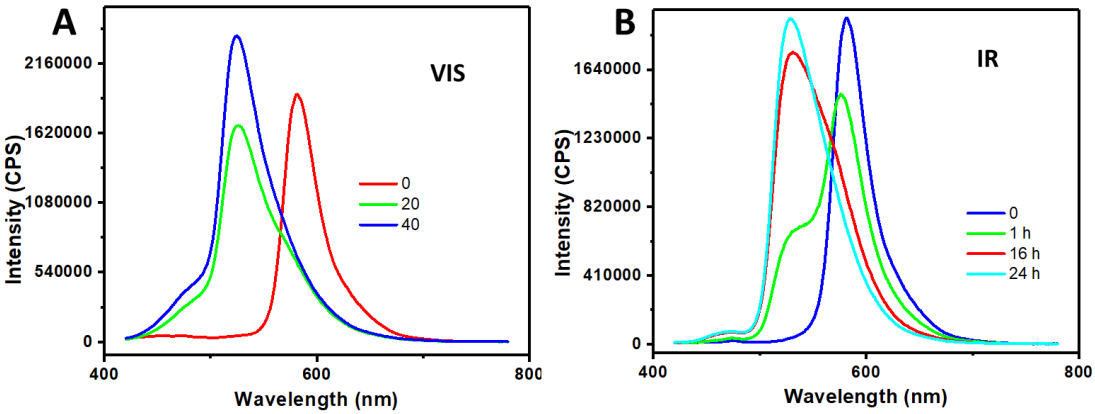

Figure 4-6. Fluorescent spectra of RhB reaction under (A) VIS and (B) IR illumination.

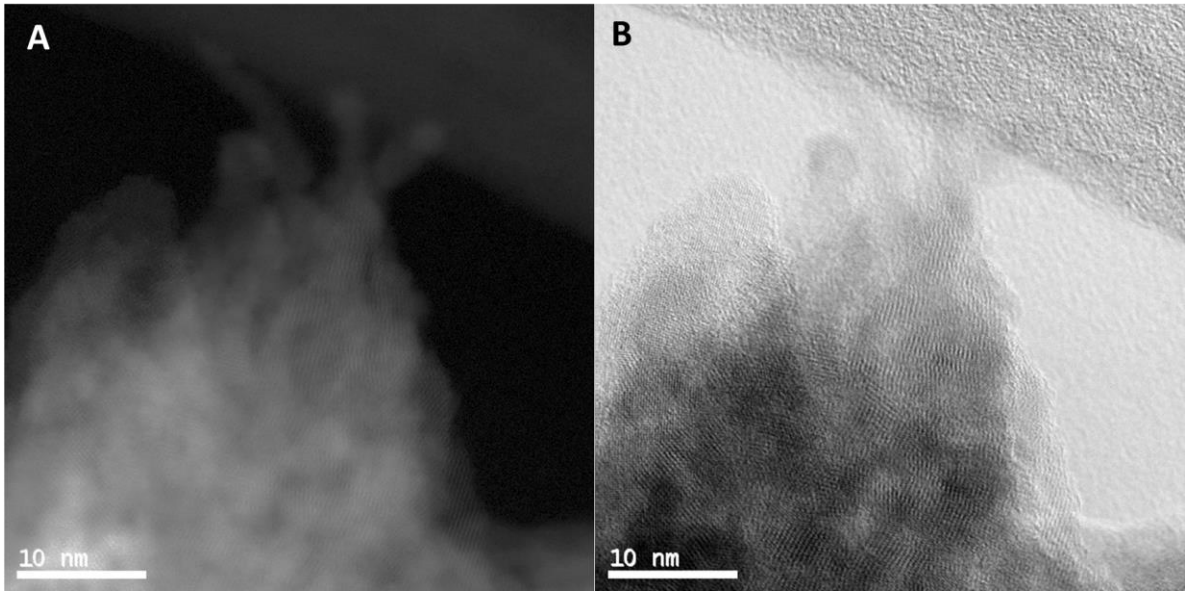

Figure 4-7. STEM of CdS SP spike (A) high angle annular dark field (HAADF) and (B) bright field (BF)

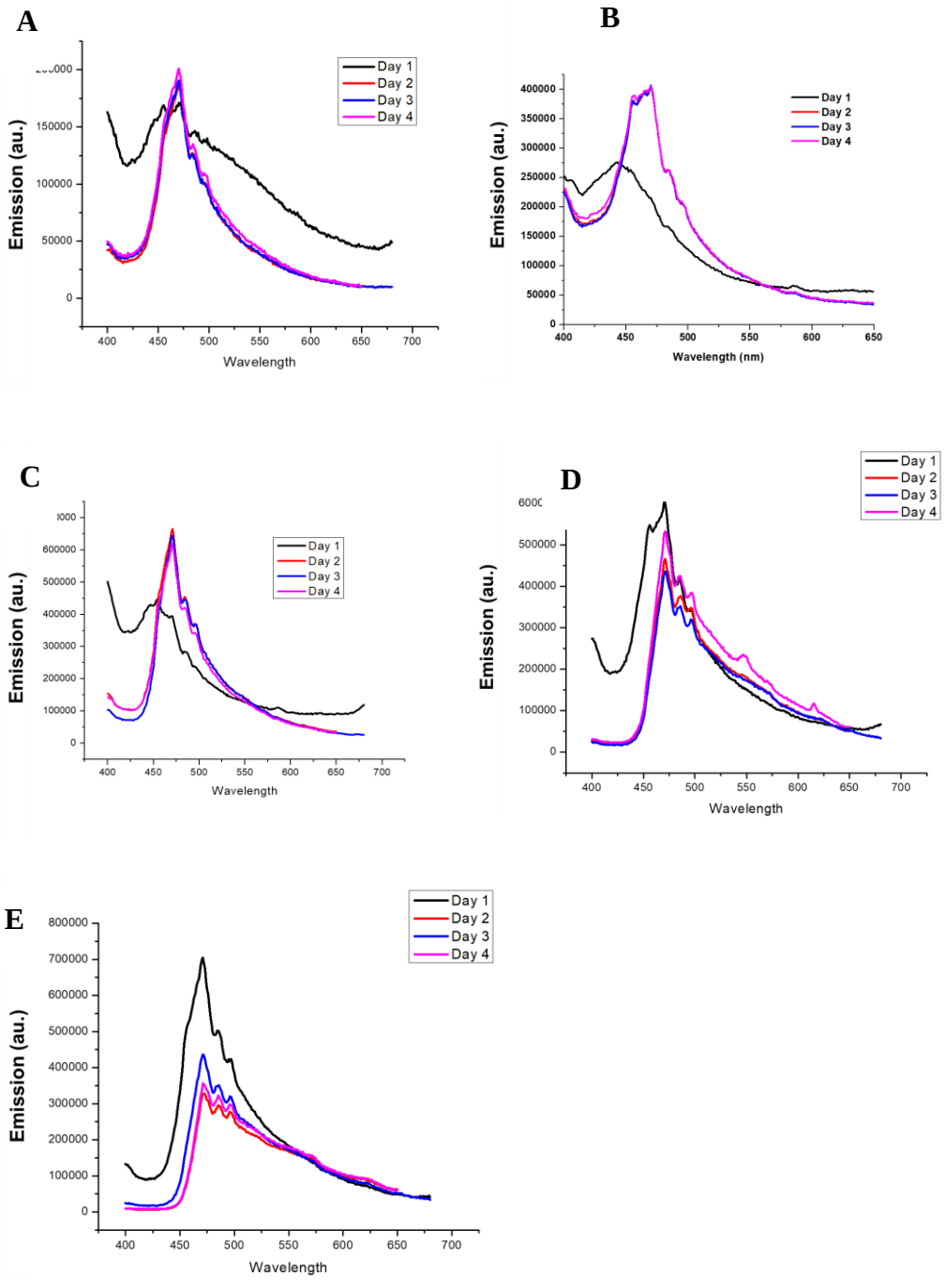

Figure 4-8. Evolution of Fluorescence emission spectra at 4 different stage of growing; (A) sample 1, (B) sample 2, (C) sample 3, (D) sample 4 and (E) sample 5.

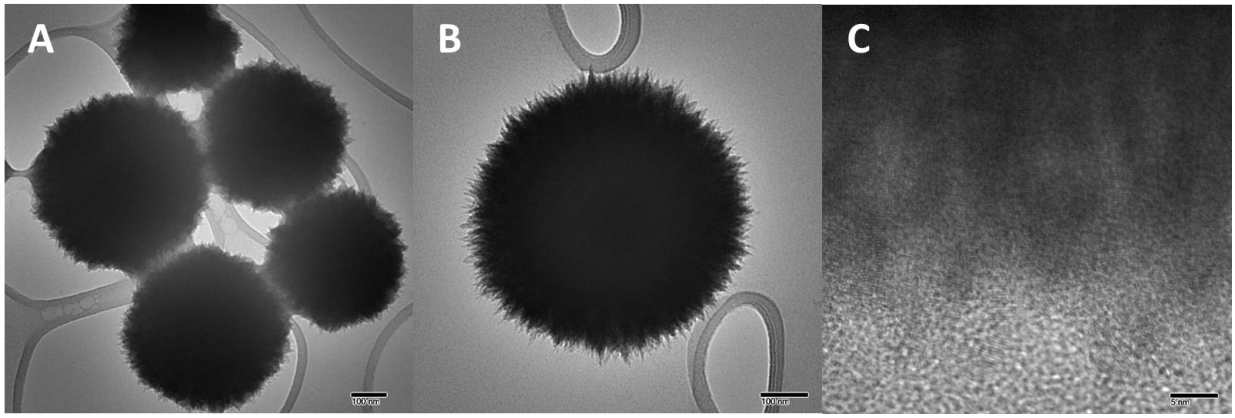

Figure 4-9. Addition of 10 mL of En to synthesis solution leads to larger, more spherical assemblies (A-B). Close up view of spike region (C).

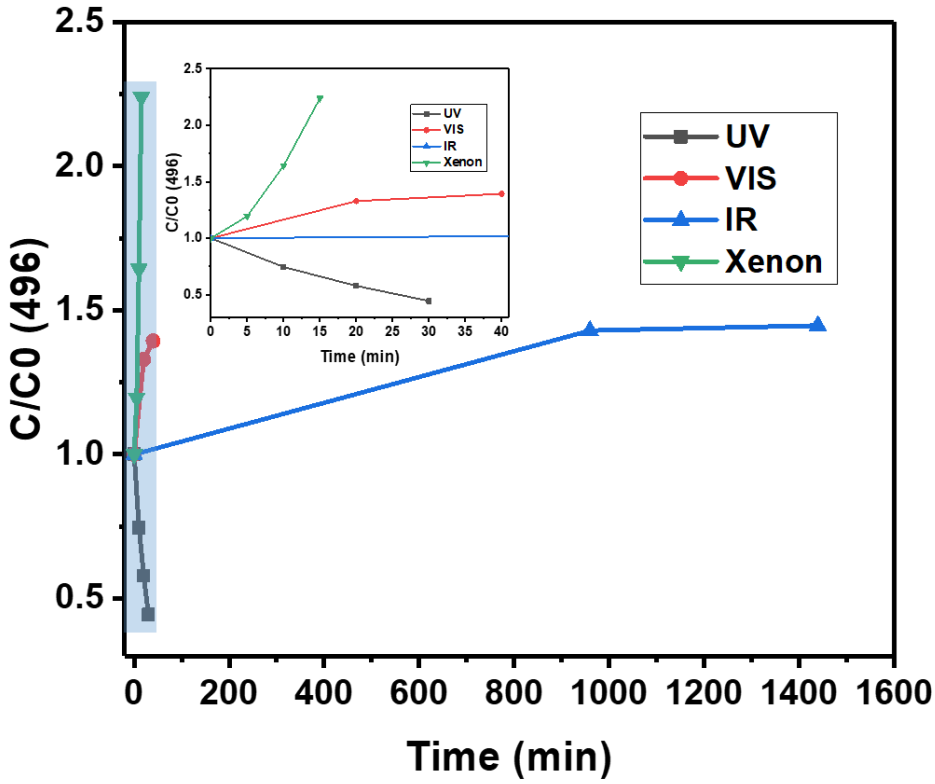

Figure 4-10. RhB degradation reaction, monitoring C/C0 at 496 nm, with inset zooming in on highlighted blue area on larger plot.

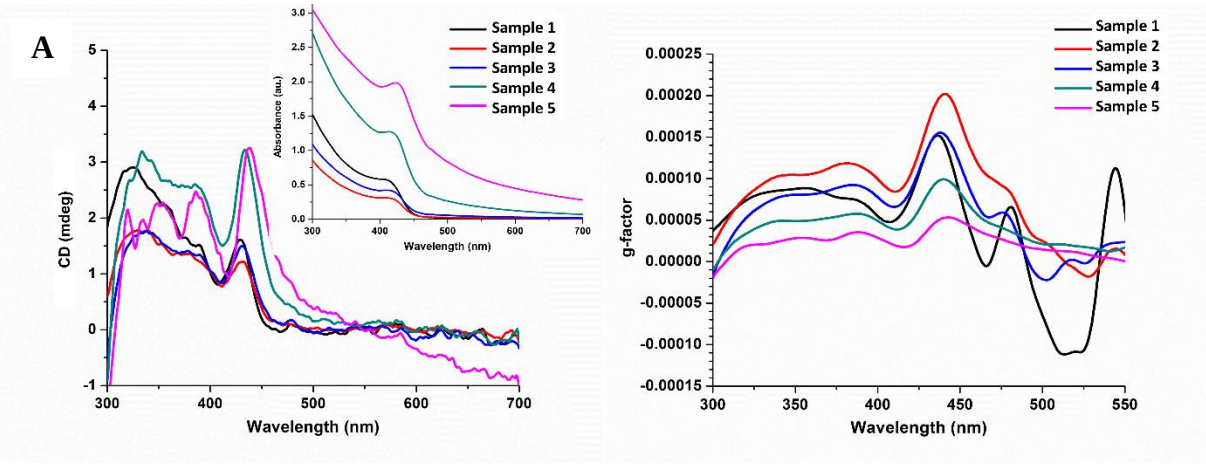
A
Sample 1
Sample 2
Sample 3
Sample 4
Sample 5
CD (mdeg)
Wavelength (nm)
Absorbance (au.)
g-factor

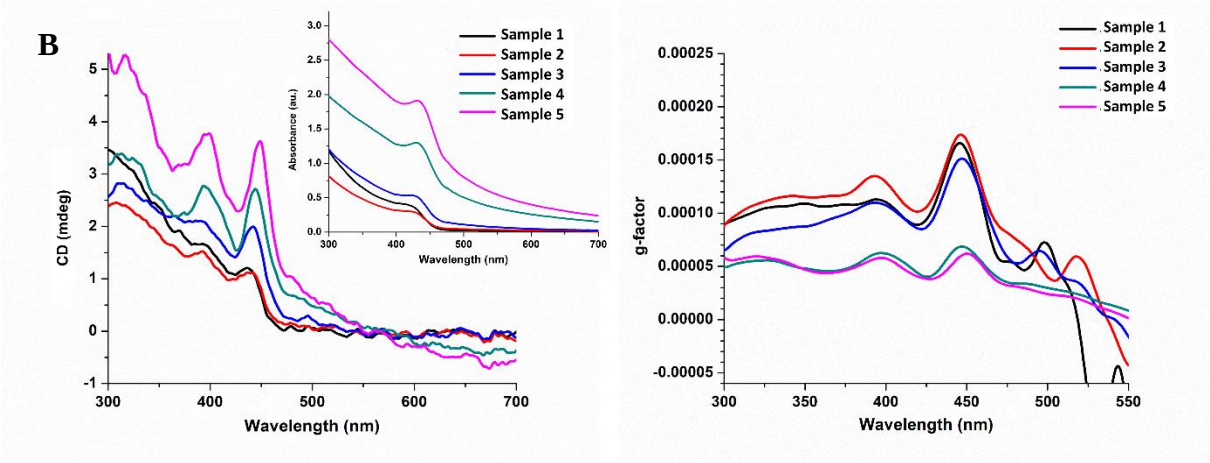
B
Sample 1
Sample 2
Sample 3
Sample 4
Sample 5
CD (mdeg)
Wavelength (nm)
Absorbance (au.)
g-factor

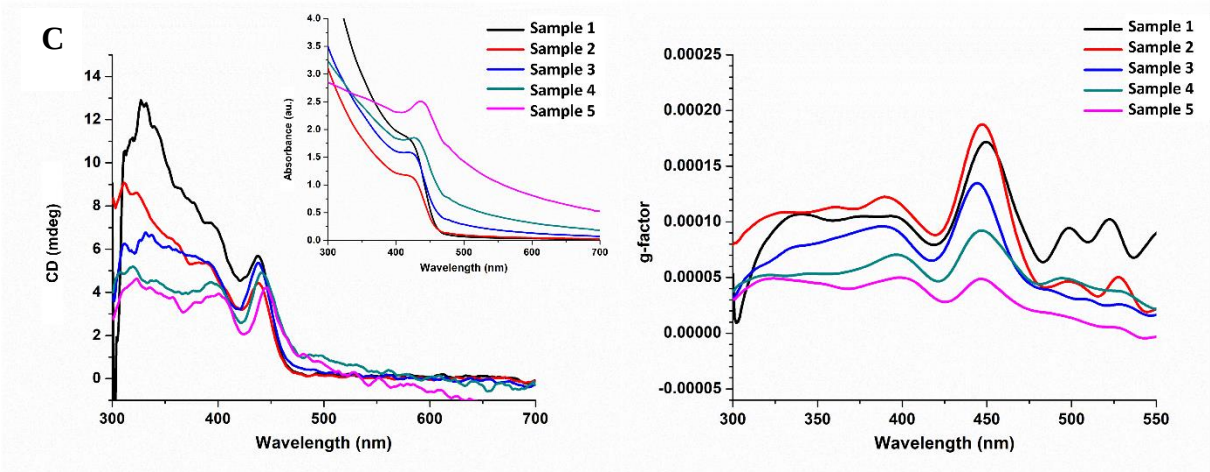
C
Sample 1
Sample 2
Sample 3
Sample 4
Sample 5
CD (mdeg)
Wavelength (nm)
Absorbance (au.)
g-factor

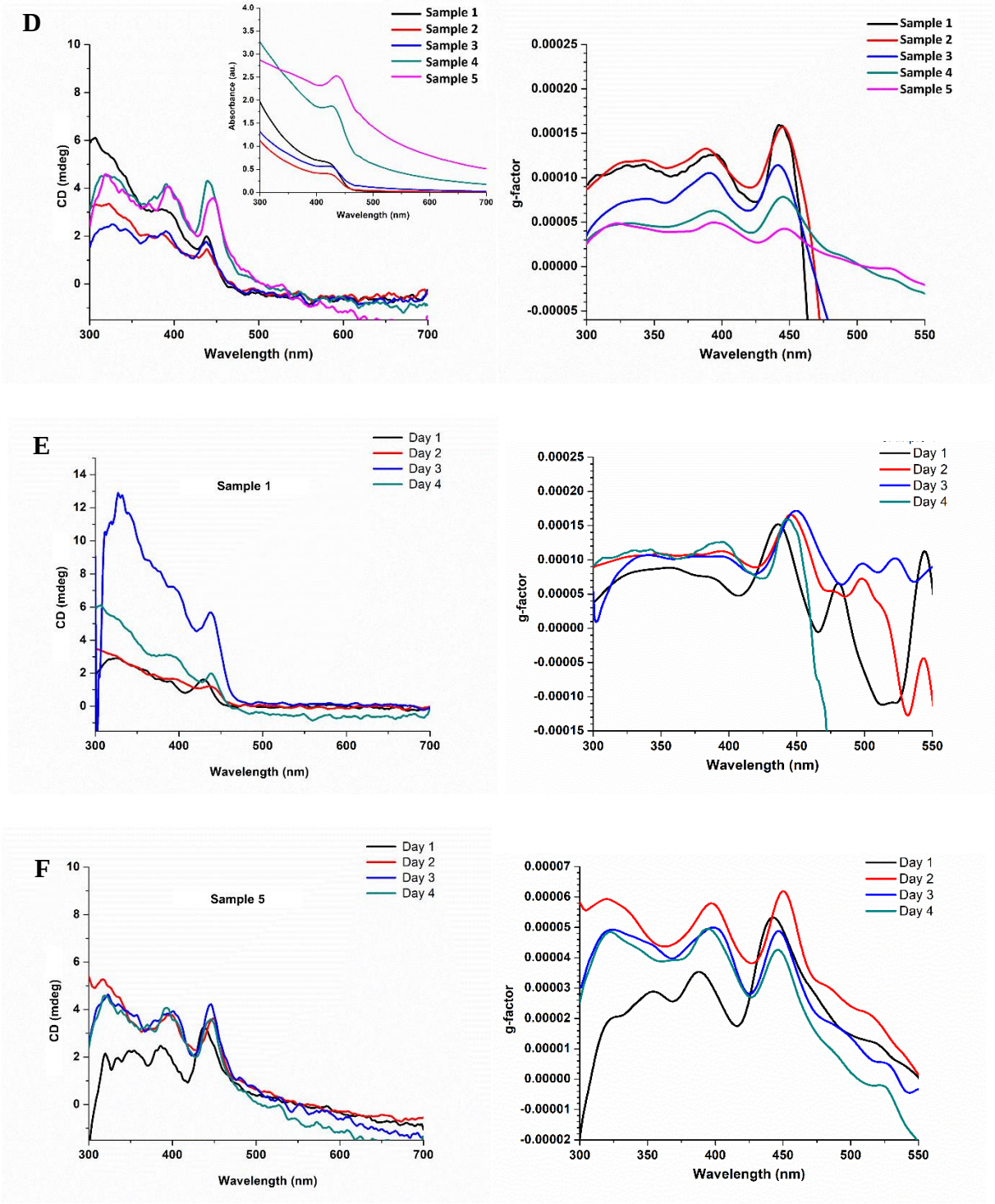

Figure 4-11. evolution of g-factor, CD spectra and corresponding absorbance for sample1 to 5 synthesized with different amount of ethylenediamine/NaOH at different stage of growth; (A) day 1, (B) day 2, (C) day 3. (D) day4 (E) and (F) Evolution of CD spectra and g-factors for sample 1 and 5 during different stage of synthesis.

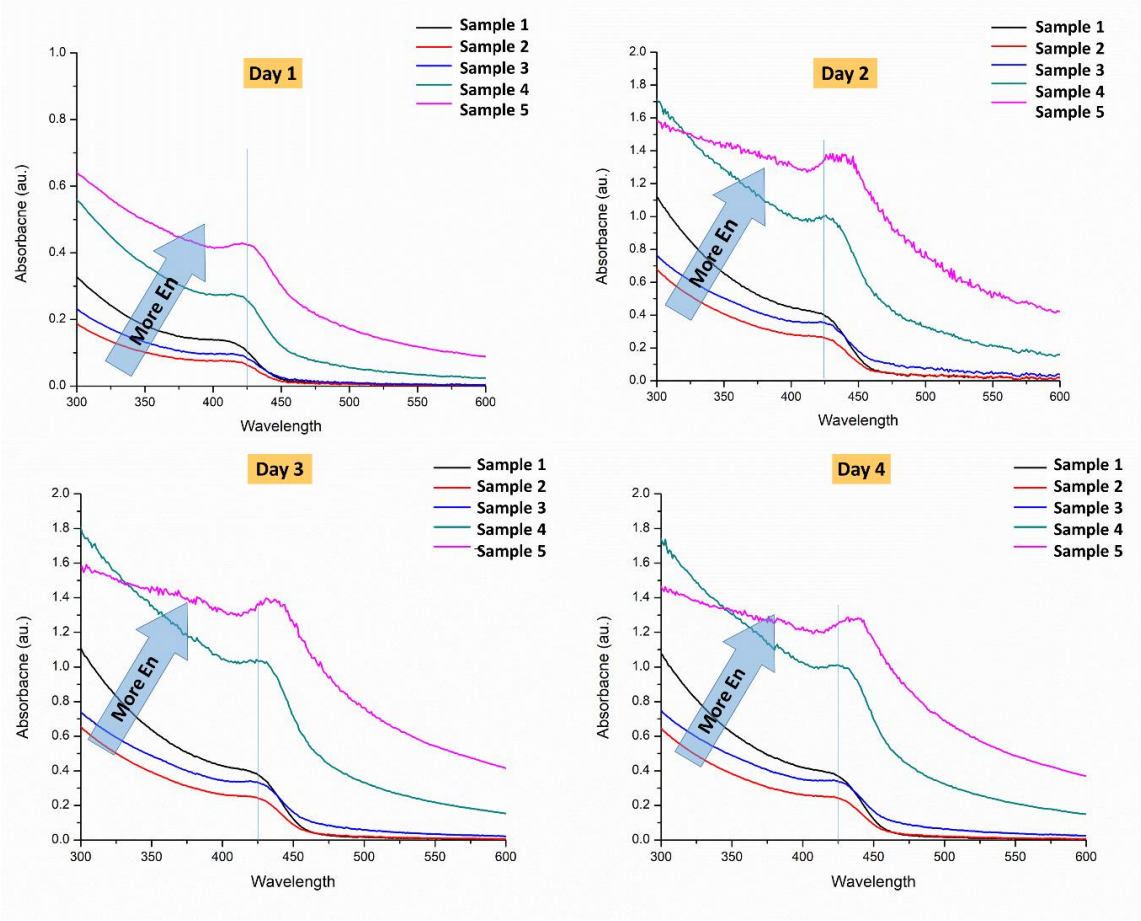

Figure 4-12. UV-Vis spectra of samples synthesized with different amount of ethylenediamine/NaOH at four different stage of synthesis and aging.

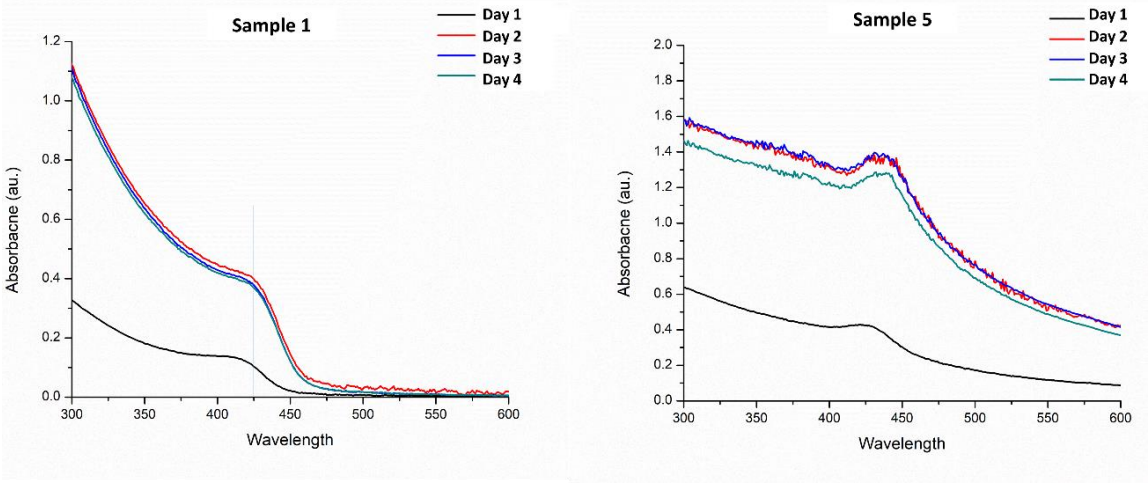

Figure 4-13. UV-Vis spectra of sample1 and 5 at different stage of synthesis and aging.

Chapter 5

Photocatalytic Supraparticles From Erdite

Naomi S. Ramesar♦, Luiz F. Gorup♦, Ming Lei, Gleiciani de Quieros Silveira, Emerson R. Camargo, Nicholas A. Kotov

5.1 Abstract

A wide spectrum of superstructures was self-assembled from erdite ($NaFeS_2$-$2H_2O$) nanoparticles (NPs) by controlling the ionic strength of the synthesis solution through the sulfur/iron (S/Fe) ratio. Particles assembled at low S/Fe ratios of 2 to 8 were fibrous in their structure, while higher S/Fe ratios, 14 to 20, caused aggregation of fibers into monodispersed spiky supraparticles (SPs), 6.62 μm ± 1.4 in diameter. As a proof of concept, the spiky erdite SPs were employed as a photo-Fenton catalyst for the degradation of methylene blue, showing proficient recyclability, when compared to existing photo-Fenton catalyst, for more than 55 cycles with the addition of hydrogen peroxide every 14 cycles. It was also found that the model lignin compound, guaiacylglycerol-beta-guaiacyl ether (GG) (at 5mg/mL), was effectively degraded up to 80 % in an aqueous environment within 3 h in the presence of SPs and H_2O_2. Reaction kinetics were significantly improved by the addition of 35 nm gold NPs to the SPs, displaying complete degradation within 40 minutes. The photocatalytic activity observed can be attributed to the synergistic interaction between NPs in the SPs along with H_2O_2. This work presents, for the first time, a facile synthesis method for a range

of hierarchical erdite superstructures with utilization as a photo-Fenton catalyst, with exceptional reusability.

5.2 Introduction

Increasing demand for renewable and clean energy sources has become a prominent issue in recent years, with enormous efforts aimed at semiconductor materials as a potential solution. Iron-based materials are attractive due to their abundance, non-toxicity, and low cost. Particularly, erdite is a naturally occurring iron-sulfide mineral found in alkalic, mafic type rocks[202] with stability in alkaline conditions. Typical synthesis routes for erdite require high energy[203] or long reaction times to produce weakly crystallized fibers[204]. Industrially, a large quantity of iron-sulfides, including erdite, are a by-product of the lead recovery process from electrolyte battery waste[205]. Dissolution-precipitation studies of the by-products indicate iron oxyhydroxide may be generated when erdite breaks down[205], resulting in large surface sites for substrate adsorption[206]. Hence, further development and use of erdite as a catalyst is a desirable direction to explore.

A recent study showed the synthesis of erdite nano-rods using MnO_2 as an auxiliary reagent for the promotion of tetracycline adsorption[203]. While few other studies focused on the upcycling of waste sludge to synthesize erdite nano-rods for adsorption applications[207,208]. However, there is a lack of research on the utilization of erdite as a catalytic material. Prior to use, development of stable and dispersible assemblies is necessary to improve the longevity and efficiency of erdite as a catalyst. The ability of heterogenous catalyst to disperse and remain stable in a wide range of solvents is advantageous but hardly recognized. Therefore, developing a new, facile method for stable and dispersible erdite fibers is highly desirable.

The advancement in NP design has led to the development and control of self-assembled

superstructures, known as supraparticles (SPs), which exhibit collective and synergistic properties unique to their constituents. Spiky SPs have attracted considerable interest as their highly corrugated surface is excellent for dispersion stability and reactivity[209] with enhanced properties for applications in catalysis. For instance, spiky SPs from TiO_2-CuS exhibited enhanced disinfection ability, improved photodegradation performance of organic pollutants, and hydrogen evolution efficiency under solar and UV light when compared to TiO_2-CuS NPs[210]. Ag_3PO_4/$LaCO_3OH$ SPs exhibited better photocatalytic activity in the degradation of Rhodamine B (RhB) along with unique morphological features which had a direct effect on the photocatalytic performance[211]. Iron sulfide in pyrite superstructures were more effective in the decomposition of methylene blue (MB) when compared to traditional pyrite particles. Pyrite SPs also showed enhanced photoelectrochemical properties, the photocurrent and rapid charge transfer performances of superstructures were more than five times larger than that of FeS_2 NPs. Hu et al showed stable discharge capacities and excellent current density of FeS_2 SPs which make a viable material for commercial utilization in rechargeable sodium batteries.

Spiky assemblies can be synthesized via different routes. *Bahng et al.* presented a hedgehog structure with a carboxylated polystyrene microsphere core with ZnO nanospikes, featuring long-term dispersion stability in both hydrophilic and hydrophobic media[209]. Chin Foo Goh et al reported that spiky nickel particles can be prepared through hydrothermal reduction using hydrazine to react with nickel salt in alkaline environment[212]. Haque et al. also shown that the presence of sodium dodecyl sulphate (SDS) surfactant and polyvinylpyrrolidone (PVP) polymer prevents the particle from gradual agglomeration during hydrothermal reduction synthesis. Dehong Chen et al utilized a phase transformation mechanism to fabricate the spiky anatase Titania particle from a metastable amorphous Titania/ammonium titanate core-shell structure[213]. By tuning

the ammonia concentration, they also showed that the size of spikes and core crystals can be controlled during solvothermal step. Stefano Stassi et al introduced that maleic acid as an anisotropic modifier used in wet-chemistry reduction of silver NPs could also result in controllable spiky particles[214]. Keisuki Kumagai et al. achieved selective growth of NP morphology between flower-like and spiky-ball-like using ascorbic acid controlled by PVP[215]. While these suprastructures show immense catalytic benefits compared to their NP counterparts, such spiky SPs are difficult or require high energy processes to uniformly synthesize and reproduce.

Based on the considerations above, we present the formation of fibrous erdite SPs through a facile synthesis and self-assembly process. Uniform, micron-sized erdite SPs with good dispersion stability are formed by controlling the ionic strength of the reactant solution under mild, favorable conditions. SPs exhibit promising photo-Fenton catalytic activity for both methylene blue and model lignin compound, guaiacylglycerol-beta-guaiacyl ether (GG), with excellent recyclability, and minor structural transformations. To the best of our knowledge, this is the first work to show the self-assembly of erdite fibers into hierarchical superstructures with immense control in the size and structure of assemblies and a range of dispersion stability for catalytic application.

5.3 Materials and Method

Materials: Iron (III) chloride tetrahydrate ($FeCl_3$· Sigma-Aldrich- ACS reagent, ≥ 99.99%), sodium thiosulfate pentahydrate ($Na_2S·9H_2O$, Sigma-Aldrich- ACS reagent, ≥99.5%). E-pure deionized water (18.2 MΩ·cm) was obtained from a Millipore Milli-Q system. All chemicals were diluted in Milli-Q water and filtered through Sterile Syringe Filter (PVDF Membrane, 0.22μm) for purification.

SPs synthesis of erdite assemblies: In a typical synthesis, 81.1 mg (0.5 mmol) of $FeCl_3$ was dissolved in 25 mL of water, while 1.86 g (7.5 mmol) of $Na_2S{\cdot}9H_2O$ was dissolved in 25 mL in a separate flask. The two solutions were mixed rapidly in a vial of volume 50 mL so that no air is inside the vial. The FeS_2 NPs were synthesized when the molar ratio of $[Fe^{3+}]/[\ S^{-2}]$ was 1:15. Initial erdite nanocolloids formed after mixed, which was accompanied by the change of the solution color to dark black. The nanoscolloids grew and crystallized into SPs by self-assembly in a dark cabinet, with no agitation, for two days. Upon completion, the SPs was separated from the reaction media by centrifugation. The precipitate was washed several times with deionized water. The final products were dried in vacuum at 60 °C for 6 h.

SPs synthesis of erdite assemblies with gold: Synthesis procedure is the same as the above method, except 5 mL of gold nanoparticles, prepared via a previously reported method[216], was added to the starting solution.

Characterization: Transmission electron microscopy (TEM) and high-resolution transmission electron microscopy (HRTEM) observations were performed using a JEOL-3011 microscope with accelerating voltage of 200 kV. Scanning electron microscopy (SEM) was performed on an FEI Nova system. X-ray diffraction (XRD) studies were carried out at room temperature on a Rigaku Rotating Anode X-ray Diffractometer using Cu Kα radiation (1.54 Å).

Photocatalytic experiments:

Methylene Blue:

The degradation efficiency of MB by SPs was completed in an aqueous solution while controlling several parameters, such as catalyst dosage, amount of H_2O_2, UV wavelength, and visible light intensity. The degradation of MB was evaluated by monitoring the evolution of the absorption at 664 nm at ambient temperature, as a function of the irradiation time. The light source was a UV handheld lamp, the distance between the lamp and the cuvette (5 mL) was about 10 cm. The average degradation rate was calculated using 3 cycles, the curve is constructed with time intervals of 30 seconds under each wavelength using a Shimadzu 1800 UV–VIS spectrophotometer.

For general photocatalysis of MB (25 μg/mL) was performed in the presence of H_2O_2 (6.0 mg/mL), SPs (0.50 mg/mL), and SPs+H_2O_2 under wavelength UV light 302 nm from UVP and dark condition.

Guaiacylglycerol-beta-guaiacyl ether (GG):

To evaluate the degradation potential of GG, 3 mL of 5 mg/mL aqueous GG was used in a quartz cuvette. 1.5 mg/mL of SPs and 6.0 mg/mL of H_2O_2 was added to the reaction and mixed for 20 minutes to allow proper distribution of particle and substrate. A 50 W handheld UV-Lamp from UVP was used for all light experiments. Control reactions with only GG, SPs, and/or H_2O_2 and in the dark was also performed. Degradation of GG was monitored using Horiba FluoroMax with an excitation wavelength of 270 nm. Further analysis was done using Agilent HPLC using a reverse phase C18 column. HPLC was ran under the following conditions: flow rate: 1.0 mL/min, temperature: 30 C, Solvent A: Acetonitrile, B: Methanol, C: Water with 0.1% trifluoroacetic acid (TFA).

Time (min)	A: Acetonitrile	B: Methanol	C: Water w/0.1% TFA
0	11.3	3.7	85
2	22.5	7.5	70
11	45	15	40
11.50	75	25	0
13	0	0	100

5.4 Results and Discussion

SP Formation and Characterization

Fibrous SPs were synthesized and assembled through the simple mixing of 1 M Na_2S and $FeCl_3$ salts with 15 S/Fe stoichiometry, without the addition of stabilizers or agitation. Samples were stored in sealed vials placed in the dark at room temperature until particles completely sediment to the bottom of the vial, leaving a translucent supernatant. This facile synthesis and assembly method is depicted by the schematic in **Figure 5-1a**. Initial solution mixtures and resulting sediments were dark green in appearance[217] (**Figure 5-1b**), while synthesis solutions that were exposed to air produced a yellow precipitate, indicative of oxidation reactions. Overall, assemblies

exhibited better shape and size homogeneity if particles sedimented completely prior to washing. Data collected from high resolution transmission electron microscopy (HRTEM) suggest that fibers are formed immediately in the reaction solution (**Figure 5-7**), however, at this early stage they are composed of loosely assembled NPs. The unidirectional assembly of particles suggest that the anisotropic shapes of the individual nanoparticles translate and contribute to the anisotropic fiber assemblies observed in this system[218].

To better understand the assembly mechanism, the stoichiometric ratio of S/Fe, 1 to 20S, was evaluated using scanning electron microscopy (SEM), while also tracking solution properties. The particles were analyzed every two days. As the concentration of sodium sulfide in the reaction varied, there was a noticeable change in the structure of self-assembled particles. For S/Fe > 4, the variation in the sodium sulfide concentration consequently increases the ionic strength of the medium. The ionic strength acts mainly on the formation speed and shape of the superstructures. It was observed that stoichiometric ratios above 15 S/Fe required less than 3 days for the self-assembly of spherical SPs and slow sedimentation of the suprastructures in the form of fibers occurred in stoichiometries between 6 to 9 S/Fe within 10 to 40 days (**Figure 5-1c**). At lower stoichiometric ratios of sulfur, 2 to 8, fiber-like assemblies were formed, whereas ratios of sulfur from 10 to 13, showed a mixture of fiber and SPs. At high sulfur ratios of 14 to 20, the exclusive formation of SPs was observed (**Figure 5-1d**).

For stoichiometries higher than 4 S/Fe no significant change in pH was observed (**Figure 5-1e**) and does not appear to contribute to the assembly process from fibers to SPs. However, the high pH does play a crucial role in the formation of the erdite crystal structure. Hydrolyzed Na_2S produces HS^- and OH^-, resulting in an increase in the pH which sequentially hydrolyzes Fe^{3+} to produce $Fe(OH)_4^-$. HS^- then proceeds to replace OH^- in the iron hydroxide structure to form

$Fe(OH)_3HS^-$, the primary species in erdite formation[203,204]. Free charges are neutralized by Na^{2+} while H_2O occupy free channels within the structure, resulting in $NaFeS_2$-$2H_2O$.

The fibrous and porous surface morphology was further investigated using SEM. Resulting SPs are monodispersed with an average size of 6.62 ± 1.4 μM and surface pore distribution ranging from 5 to 120 nm (**Figure 5-2a**). To better understand the influence of the morphology on the specific surface area, N_2 adsorption–desorption isotherms of SPs were investigated using a nitrogen adsorbtometer (**Figure 5-8**). SPs exhibited a specific surface area of 8.2 m^2/g with irregular pore size distribution, suggesting that the architecture contains multiple pore sizes. Particles synthesized with similar morphology demonstrate it is possible the erdite SPs have two prominent pore sizes, that is, a bimodal distribution with smaller (~5.0 nm) and larger (~65.6 nm) mesopores[219]. The small mesopores with an average diameter of 5.0 to 100 nm can be assigned to the interstitial pores formed along the adjacent nano-spike, and the diameter larger than 100 nm can be attributed to the pores formed on the surface of SPs in the absence of spikes.

HRTEM was utilized to further examine the spikes and crystallographic features of erdite SPs. A closer look at the individual spikes of the SP reveal they are composed of self-assembled erdite NPs with an average size of 4.3 ± 0.67 nm (**Figure 5-2b**). Lattice distances of the individual particles are determined to be 0.54 ± 0.01 nm and 0.42 ± 0.01 nm, which corresponds to the (200) and (111) plane of erdite (**Figure 5-2c**). Electron diffraction (ED) of the SPs sample show only a single set of diffraction rings, which can be indexed to the corresponding (200), (220), (221), (330), (440) planes of erdite. This pattern aligns with the obtained X-ray diffraction (XRD) pattern (**Figure 5-2e**), where all diffraction peaks are in agreement with the erdite phase (PDF No.33-1254). Energy-dispersive x-ray spectroscopy (EDS) mapping also confirmed the composition of

the SPs to contain oxygen, sodium, sulfur and iron in ratios that match the percentages found in erdite (**Figure 5-9**).

To examine the role of ionic strength on the self-assembly of superstructures from fibers to SPs, sample 15 S/Fe was diluted to concentrations of 1 to 10 mM (**Figure 5-3**). The structures presented show an intermediate stage morphology, progressively developing from fibrous assemblies to fibrous spherical superstructures as the variation in the concentration of the reactants increase. The evolution of structural complexity from fibrous SPs to spherical SPs can be represented through a new approach which utilizes graph theory (GT) method to calculate the complexity index (CI) of NPs[220]. GT models are based on a modified augmented valence sum calculation and highlights the progression of complexity in structures through a comparable base value. Proposed graphs are presented in the first row of **Figure 5-3**, followed by the complexity index (row two) and both TEM (third row) and SEM (forth row) imaging to produce a 1-dimensional phase diagram. Simple fibrous assemblies are represented as two nodes, connected by an edge, with a CI of 1.5. As these fibers continue to assemble into more complex assemblies, the CI increases to 15.75 for fibrous bundles and 18.0 for the final spherical SPs. With an increase in the ionic strength of the solution, corresponding changes can be noted in the overall complexity of the particle structure.

A key transition point in the assembly occurs at 8-9 mM when the flexible fibrous bundles begin to bend inward and transition to ‘pac-man’-like assemblies, closing in on one side. Eventually, ‘pac-man’ assemblies bend inward on the open side to close and form the final spherical assembly. A closer look indicates similarities to the radial arrangements of the flexible fiber arrays of the dandelion pappi[221].

To further investigate the role of the ionic strength, assemblies with 6S/Fe ratio, known to form fibers, was prepared in NaCl solutions with concentrations ranging from 0.06 to 1 M (**Figure 5-10**). When no NaCl is present, fibers form as expected. As the concentration of NaCl is increased to 0.06 M, intermediate fibrous bundles can be seen, turning into spherical SPs at NaCl concentrations of 0.13 and 0.25 M. At concentrations > 0.5 M, neither fibers or SPs are present. At such high concentrations, irregular flakes and fibers are produced.

Dispersion stability of SPs were evaluated in a range of solutions, from polar to non-polar, and monitored through the absorbance changes on a UV-Vis spectrometer. As expected, dispersions were more stable in polar solvents. After 20 minutes of observation, approximately 40 % of particles remained suspended in more polar solvents (water, methanol, and ethanol). For non-polar solvents, apart for hexane, 25 % of particles remained in suspension (**Figure 5-11**). It is important to emphasize that after simple manual agitation it is possible to disperse the particles again. Similar results of maintaining particles suspension in solution was found by *Bahng et al.* with particles of similar size and morphology[209]. They showed that the corrugated surface of spiky particles contributed to the colloidal stability in both polar and non-polar solutions. Dispersion stability in solution is beneficial as efficient distribution of particles can support prolonged catalytic activity.

SP photo-Fenton catalysis

To evaluate the photocatalytic ability of erdite SPs, a proof of concept photo-Fenton reaction was explored using organic dye, methylene blue (MB). Photodegradation kinetics was evaluated by observing the decrease in the absorption spectra of MB at 664 nm (**Figure 5-4a**). Control experiments with SPs in the absence of H_2O_2 and vice versa, show low removal activity, the SPs

alone removed 32 % of MB in 100 min. The results obtained indicate that SPs and/or H_2O_2 alone are inadequate catalysts for the reaction. The removal efficiency of MB was greatly increased in the presence of both SPs and H_2O_2, with MB being completely removed in less than 5 min, 13 times faster than photolysis reaction of H_2O_2 (**Figure 5-4b**). These results suggest a synergist interaction between SPs and H_2O_2, resulting in excellent catalytic performance for the degradation of MB. When compared to H_2O_2 activity, less than 15% of MB is removed in 5 min and 100 % degradation occurs after 70 min. A control experiment in the dark environment with SPs and in the absence of H_2O_2 show a rapid degradation of 80% MB in 3 minutes due to the adsorption of the dye on the particle surface, but after three minutes the surface of the particle begins to be oxidized and release the dye molecules causing the increase of colorization (**Figure 5-4c**). This process stabilizes at 40% degradation after 60 min. However, even in the dark environment, the SPs exhibits catalytic activity with the help of H_2O_2 because the hydroxyl radicals are produced from the reaction between the SPs and H_2O_2 via Fenton-thermic reaction in dark condition. The photocatalytic efficiency of MB in dark condition with SP- H_2O_2 system is a is 2.5 higher than SPs (without H_2O_2) under irradiation 302 nm, indicating the hydroxyl radicals generated from SPs and H_2O_2 plays a key role in the degradation of the MB in the presence or absence of UV-light.

Reusability of erdite SP catalyst

Recyclability and stability of a catalyst is as paramount as its performance. Therefore, reusability of SPs was performed in the presence of H_2O_2 and MB (**Figure 5-5**). For each cycle, the concentration of MB was adjusted to an initial value of 25 μg/mL. For 14 complete cycles, no significant decrease in activity was observed. However, at the 15^{th} cycle, the activity began to decrease and at the 16^{th}, there appears to be complete loss of activity (**Figure 5-5b**). The addition

of 6.0 mg/mL of H_2O_2 prior to the 17th cycle quickly restored photodegradation activity, suggesting that loss of activity was due to the complete consumption of H_2O_2 and not SP performance. This trend is repeated, between the 17th to 30th cycle and no significant decrease in photodegradation activity was observed, the SPs were stable for another 14 consecutives cycles. The SPs showed excellent activity and recyclability for more than 55 cycles, it is the first time an iron sulfide-based catalyst exhibited such high recyclability.

To further demonstrate the stability of SPs, SEM images of the catalyst was captured after 55 cycles of photocatalytic activity (**Figure 5-5c**). While there is a noticeable change to the surface of SPs after extensive cycles and the tips of spikes were reduced, the overall integrity of the primary SP structure was maintained. The morphology of the catalyst can strongly affect key features such as substrate adsorption, desorption, mass transfer and recombination of photo-generated electron/holes. Therefore, it is promising that reduction in SP spikes did not appear to have a large impact on the catalytic activity.

A common problem encountered in catalysis is the decrease in activity due to poisoning of the catalyst surface by the substrate or by-products. However, in the 55 cycles tested for the erdite SPs, this was not observed. This may be due to the co-catalyst, H_2O_2, preventing permanent adsorption to the SP surface. Comparing the degradation curves of MB with SPs and SPs + H_2O_2 in the dark condition shown in Figure 4d, we observe that the dye does not adsorb on the surface of the particles in the presence of H_2O_2 and peroxide is readily accessible to generate hydroxyl radicals.

Lignin model: Guaiacylglycerol-beta-guaiacyl ether (GG)

Promising photoactivity and recyclability of erdite SPs make them a good candidate for more extensive studies. Lignin is a highly aromatic plant polymer, rich in β-O-4 linkages that has extreme potential to serve as a renewable raw material for a tremendous wealth of products, from high value aromatics to biofuels. However, due to the sheer size and complexity of this naturally occurring polymer, evaluation of its degradation potential was explored using a model compound that contains β-O-4 linkages and represent a fragment of lignin. Typically, catalytic reactions of lignin or model compounds are carried out in organic solvents. However, to utilize the photo-Fenton reaction, the model compound, guaiacylglycerol-beta-guaiacyl ether (GG), which was soluble in water up to 5 mg/mL, was targeted for further assessment.

The degradation of GG was monitored through fluorescence emission at 330 nm after being excited at 280 nm (**Figure 5-6b**). Within 3 h, GG in the presence of SPs and H_2O_2 under 302 nm UV light showed more than 80 % degradation. Control experiments, including GG alone and GG with SPs showed no change over the 3 h period. While GG with H_2O_2 (under 302 nm), and GG with both SPs and H_2O_2 in the dark showed minimal degradation, about 15-20 % after 3 h. Again, there is a synergistic interaction between the photo reaction and the Fenton reaction to yield the most efficient degradation of GG. High pressure liquid chromatography (HPLC) shows a strong signal at 6.36 min retention time which corresponds to the pure GG compound **(Figure 5-12**). Monitoring the GG peak area at 6.36 min, a steady decrease is observed over the reaction period, while the appearance of a new peak at 1.8 min retention time begins to emerge and increases with time (**Figure 5-6c**). After 120 min the original GG peak is no longer visible, suggesting that all the substrate is converted.

One major benefit of SPs is their ability to be assembled from several different NPs in order to enhance or combine photocatalytic functionality[7,172]. To capture the full benefit of self-

assembled supraparticles, 35 nm gold (Au) NPs was added to the synthesis solution to generate Au-erdite SPs. TEM and SEM imaging show that Au NPs are randomly clustered throughout the SPs, specifically for the spike region, as the core is very electron dense and NP components are indistinguishable (**Figure 5-13)**. The reaction time is significantly improved with Au-erdite SPs and complete degradation of GG is observed in 40 minutes when SPs are used in combination with peroxide and UV-light. Control studies for Au-Erdite were performed in the dark with and without H_2O_2 (**Figure 5-14**). Au-SPs with H_2O_2 showed about 30 % decrease, while particles without peroxide showed no change, following the same trend from MB system presented above. The combination of plasmonic and semiconductor constituents in the SPs shows improved catalytic performance as electron-hole pairs are easily generated through improved light adsorption, however, recombination is reduced as the photogenerated electrons prefer the Au surface, while the holes remain on the erdite[172].

The increased rate observed from the SP-H_2O_2 pair under UV-light is due to the iron redox cycling in the $NaFeS_2$-$2H_2O$ /H_2O_2 system, where the oxidation of (Fe(II) into Fe(III)) is accelerated, thereby promoting the rate of decomposition of H_2O_2 into HO•. Hence, the decomposition of H_2O_2 significantly accelerates in the presence of SPs, leading to more efficient degradation by the SP- H_2O_2 system and demonstrating that the hydroxyl radicals generated are the main oxidative species in the Fenton reaction. Concurrently, photogenerated electrons in the SPs transfer from the valence band to the conduction band, generating an electron-hole pair. The photogenerated hydroxyl radicals can be produced by the reaction between the photogenerated hole and H_2O. Additionally, when erdite is hydrolyzed, Fe oxyhydroxide species are generated, lending to an increase source of radical species while providing a large number of surface coordination site for substrate adsorption [203,206,208].

5.5 Conclusions

We have presented a facile synthesis and self-assembly method for a wide spectrum of hierarchical erdite superstructures. SPs are self-assembled from erdite NPs by controlling the ionic strength of the synthesis solution through the sulfur/iron (S/Fe) ratio to produce fibrous assemblies that eventually agglomerate into spiky spherical SPs. Erdite SPs were successfully utilized as a photo-Fenton catalyst for the reduction of MB and lignin model compound, GG, in an aqueous dispersion. The results show that SPs + H_2O_2 catalyst have a high photocatalytic activity towards degradation of both substrates under UV light, suggesting a synergistic photo-Fenton reaction is ideal for this system. While the addition of gold NPs immensely improves the reaction time to 40 minutes from 120 minutes. SPs catalyst showed excellent activity and recyclability for more than 55 cycles, a value that is high for a Fenton catalyst.

SPs exhibits high specific surface area, high adsorption capacity, long-term colloidal stability in hydrophilic media, excellent and low recombination of the photo-generated electrons and holes due to the shape of nanostructure and erdite phase property. Therefore, our findings have opened a new approach for improving the photocatalytic activity, meanwhile put forth a green and feasible photocatalyst, which may build a bridge for environment and energy in the future.

5.6 Figures

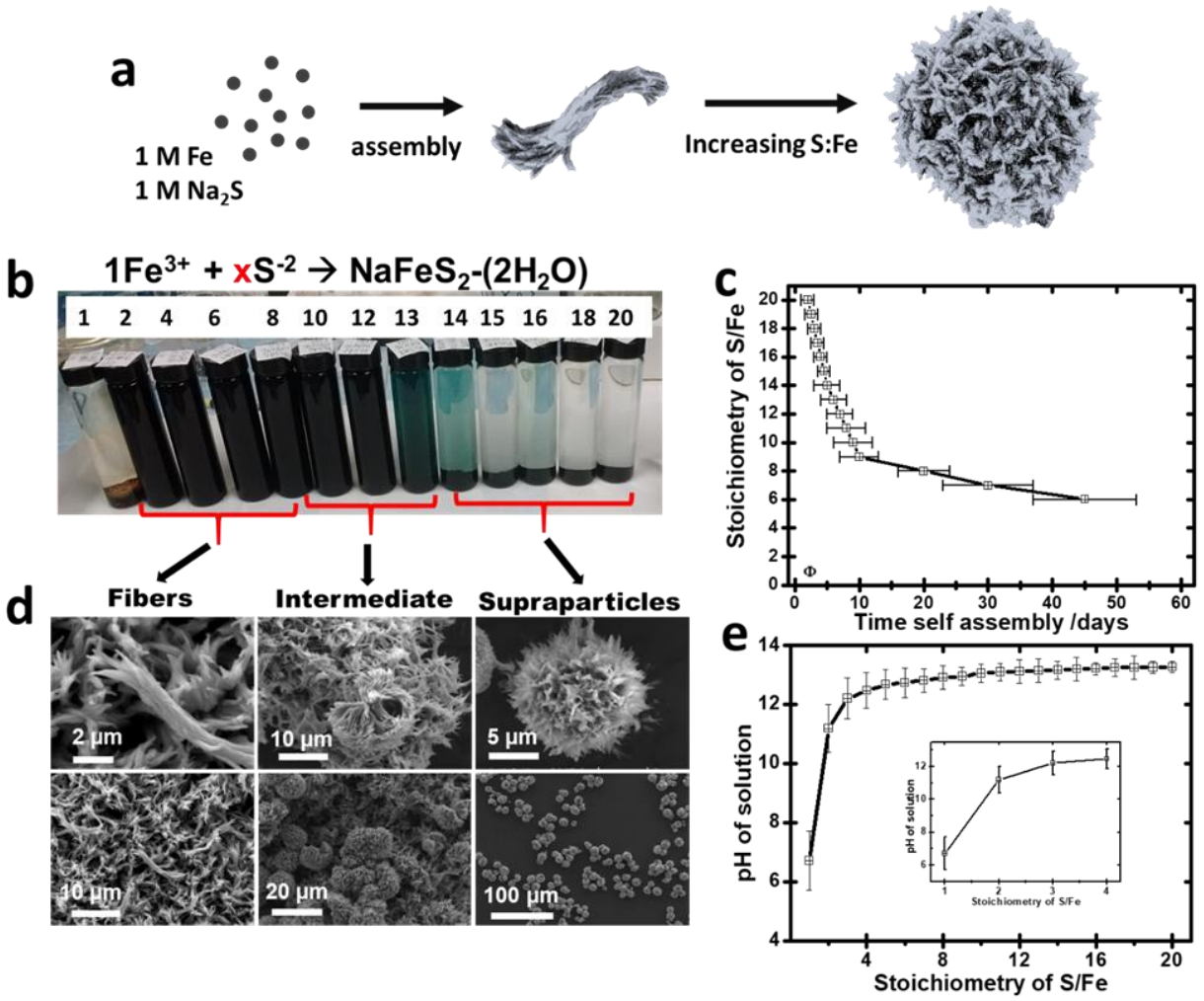

Figure 5-1. (a) Synthesis and assembly schematic of erdite SPs; (b) reaction flasks with 1 to 20 S/Fe synthesis solutions; (c) Reactant stoichiometry versus sedimentation time profile of particles; (d) SEM of SPs for different S/Fe stoichiometry; (e) pH versus varying stoichiometry of the reaction.

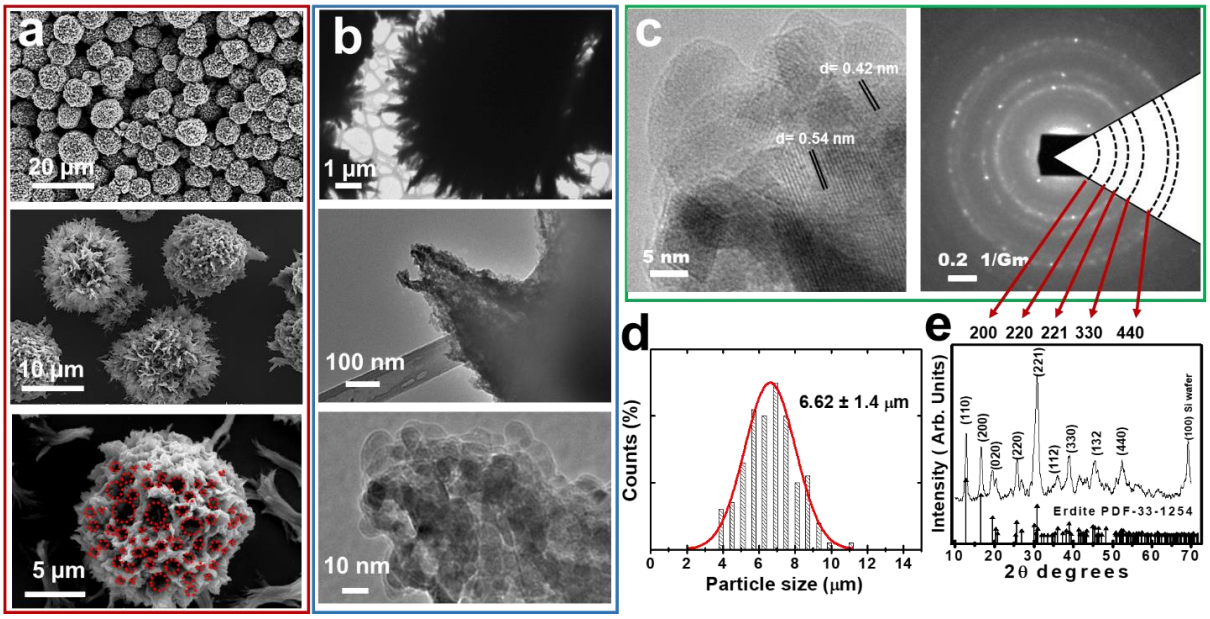

Figure 5-2. (a) Scanning electron microscopy of SPs, with focus on an individual SP; (b) Transmission electron microscopy of SP, with close up on individual spike; (c) The ring diffraction pattern from a polycrystalline erdite particles; Crystal planes and interplanar spacing are shown by Miller indices; (d) Particle size histogram fitted with a log-normal distribution of SPs in (a); (e) XRD pattern of the SP.

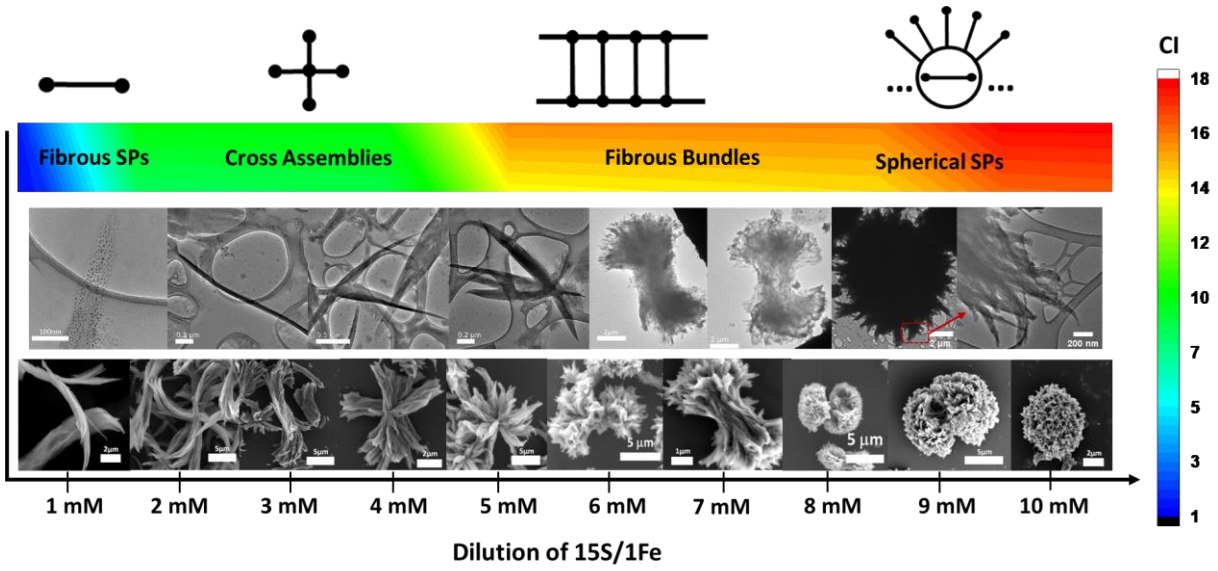

Figure 5-3. Phase diagram to showcase the complexity and diversity of assemblies as the ionic strength is increased in the reaction media. The first row interprets the respective graph theory models for the corresponding assemblies imaged by TEM (third row) and SEM (forth row). The change in structure from individual NPs, to spherical assemblies composed of fibrous SPs, is represented in the second row by the complexity index gradient.

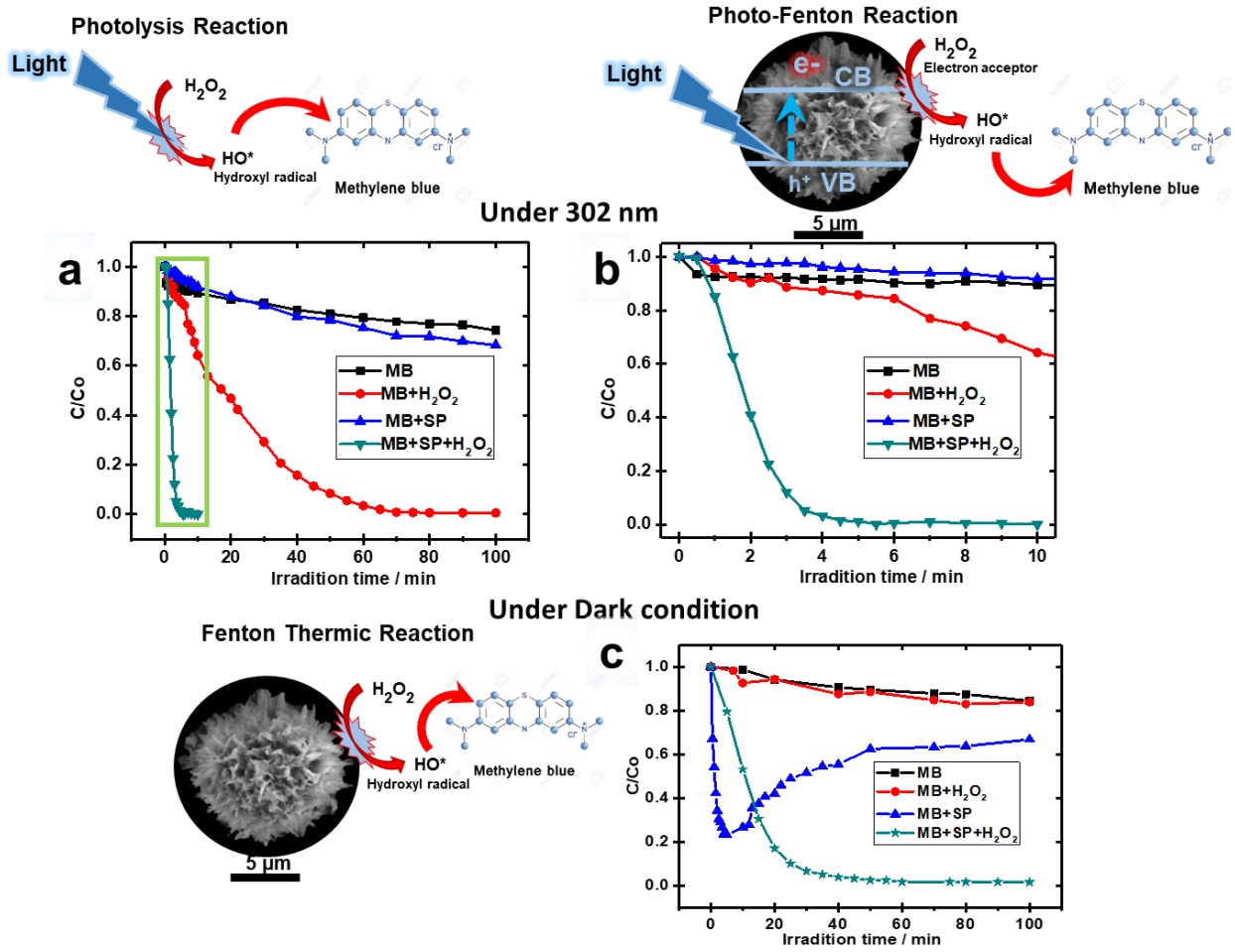

Figure 5-4. Photocatalysis of MB in the presence of erdite SPs. (a) Reaction under UV light of 302 nm, (b) closer look at the portion of graph highlighted by green rectangle in (a); (c) reaction carried out in the dark.

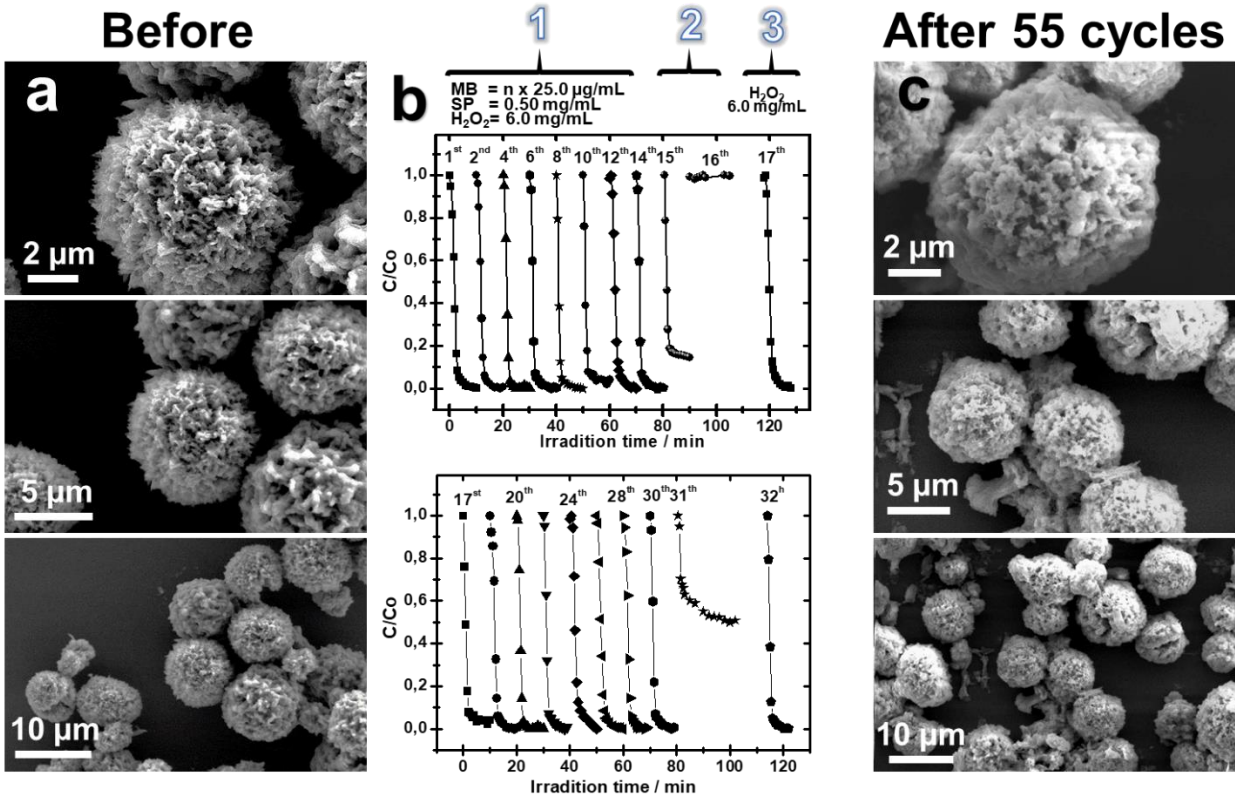

Figure 5-5. (a) SEM of catalyst before photocatalytic test ; (b) consecutive cycles of degradation of MB in the presence of the SP + H_2O_2 under UV light 302 nm; (c) SEM image of catalyst after 55 cycles photocatalytic test

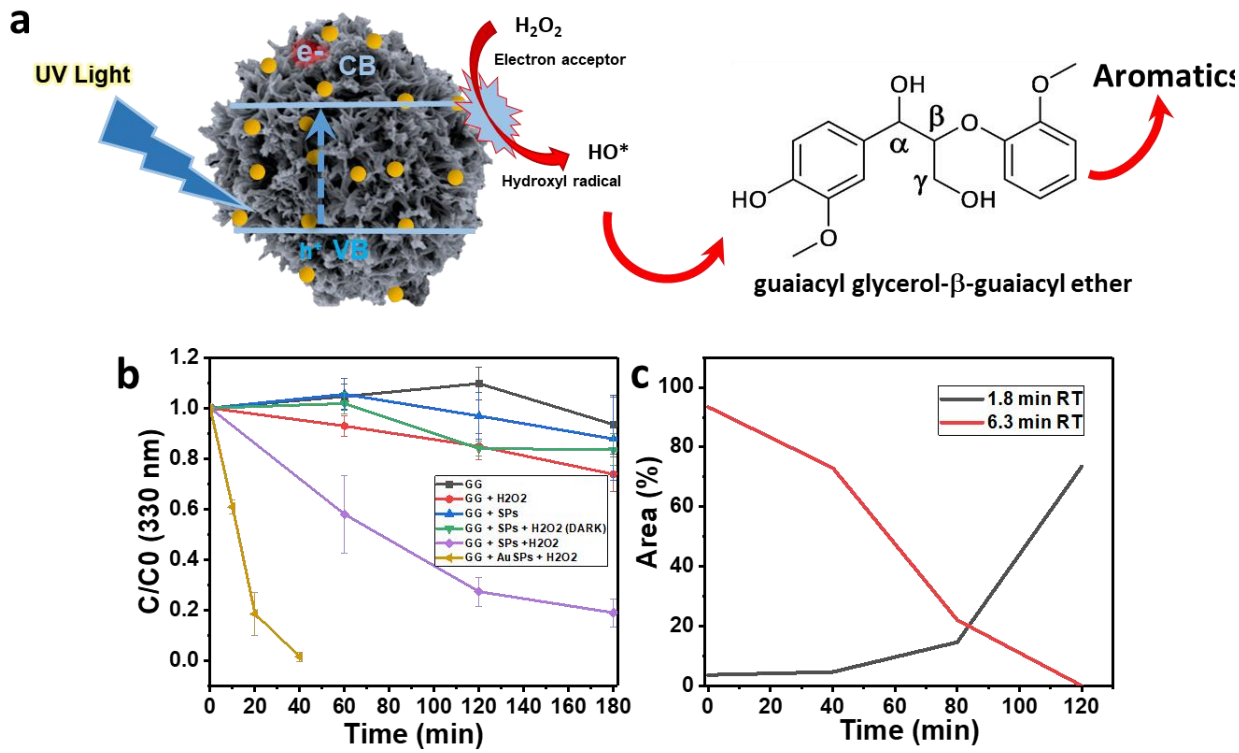

Figure 5-6. (a) schematic of photo-Fenton reaction of lignin model compound, GG, by Au-SPs; (b) C/C0 (330 nm) for GG over reaction time of 120 min; (c) HPLC area versus time at retention times of 6.3 and 1.8 minutes.

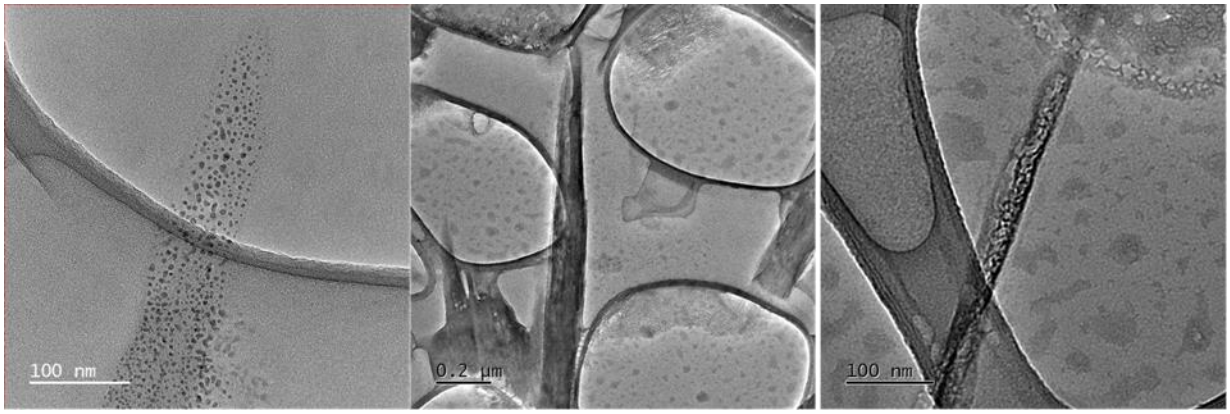

Figure 5-7. Transmission electron images of fibers produced immediately following the mixing of reactant species (15S:1Fe)

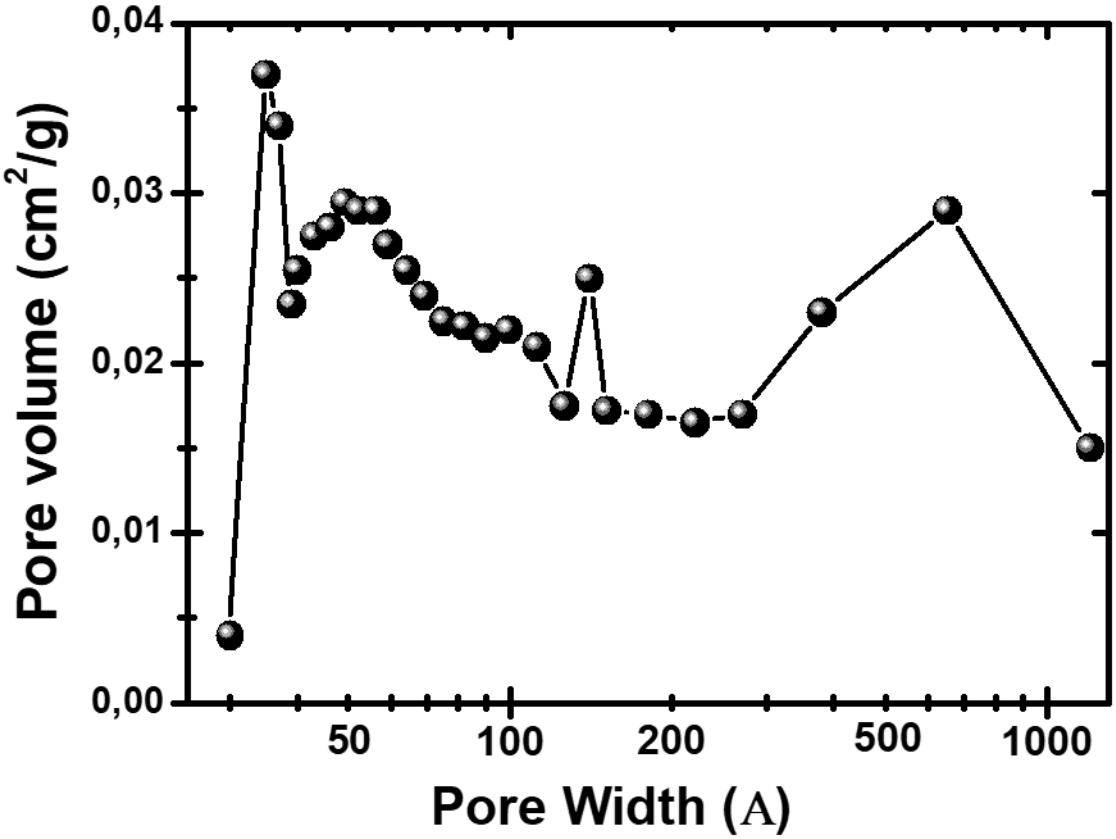

Figure 5-8. N_2 adsorption–desorption isotherms of SPs using a nitrogen adsorbtometer (BET method).

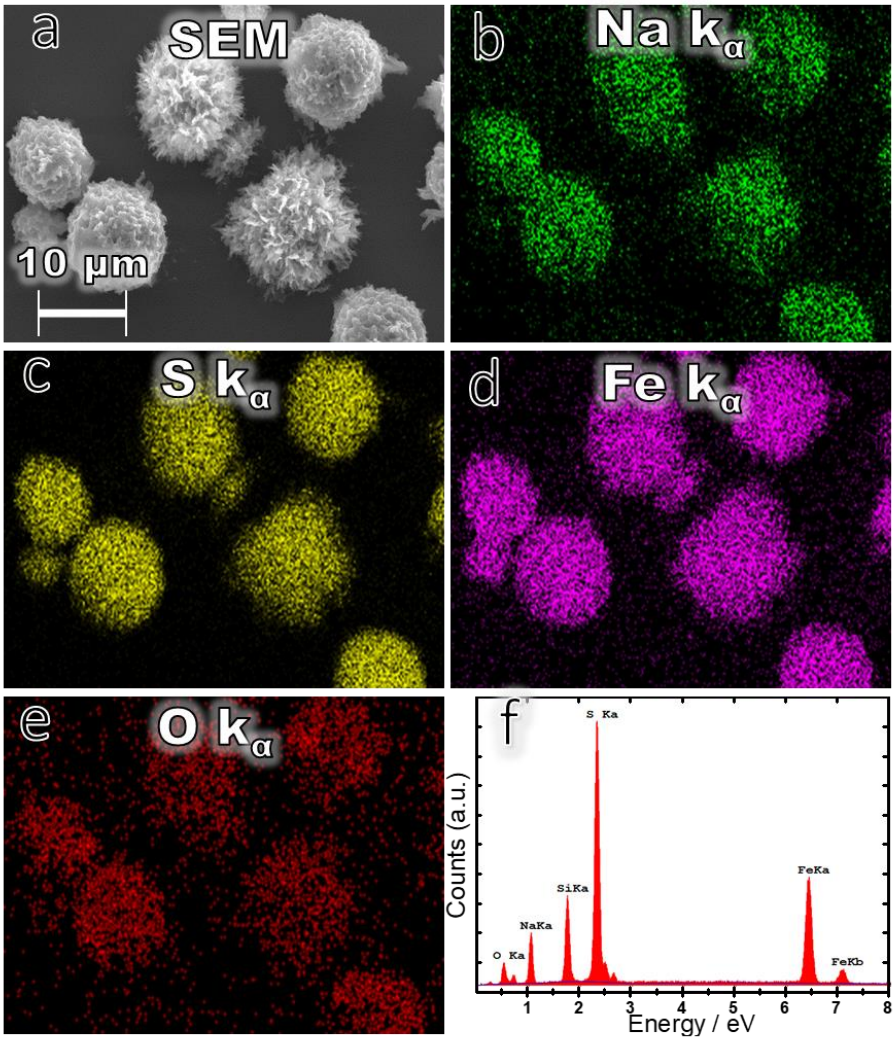

Element	Atomic % of sample	Atomic % of $NaFeS_2$-($2H_2O$)
O K	36.4	33.3
Na K	26.4	16.5
S K	27.3	33.3
Fe K	9.93	16.5
	100 %	100 %

Figure 5-9. SEM images and EDS mapping of the 2D elements Na K_a, S K_a, Fe K_a, and O K_a of sample 15Sa15 deposited on a silicon substrate.

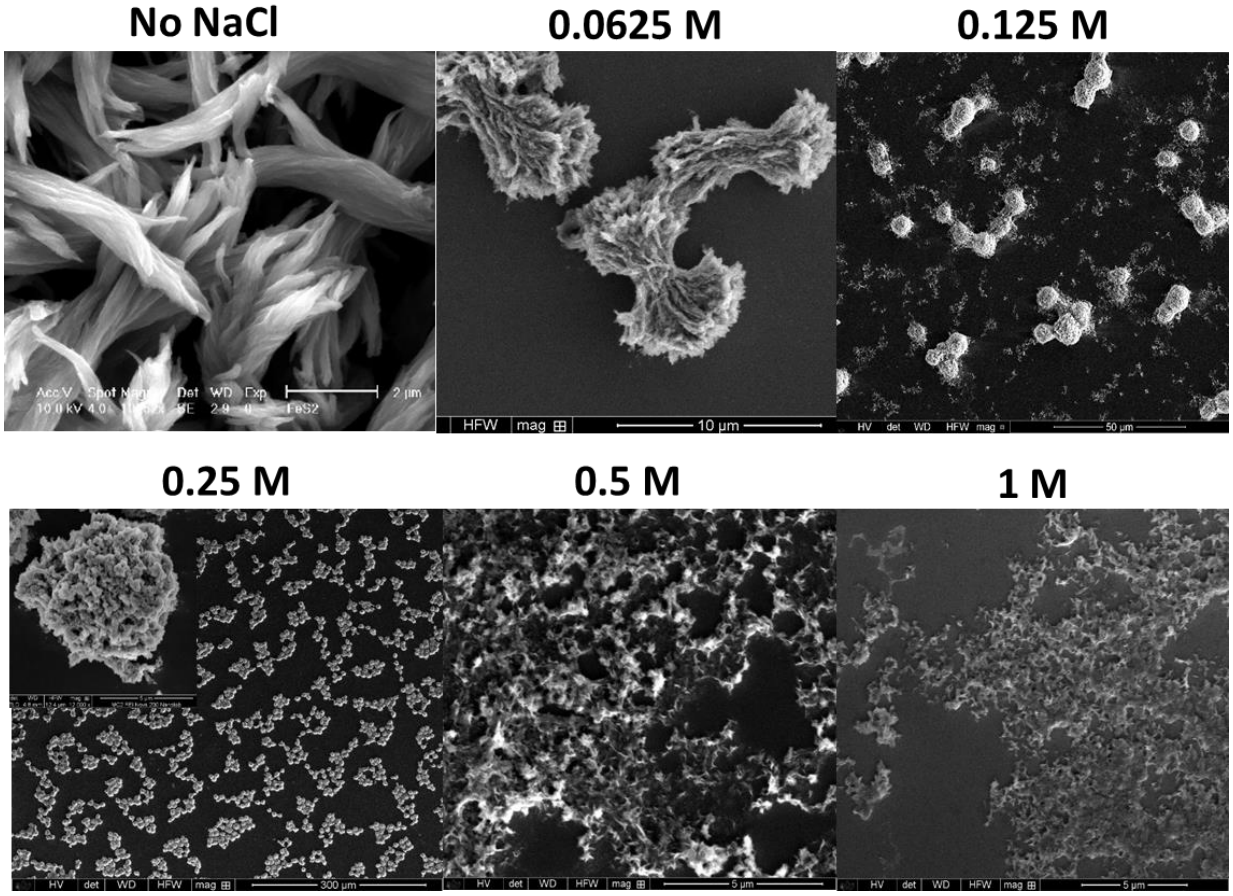

Figure 5-10. A 6S:Fe ratio was made in varying concentration of NaCl solutions, ranging from 0.06 to 1 M.

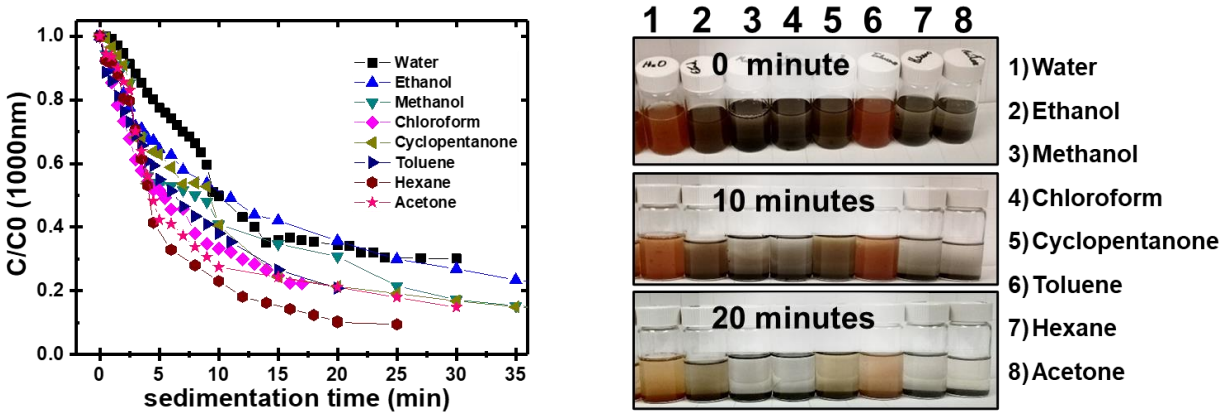

Figure 5-11. Dispersion stability of hedgehog SPs in polar and non polar solvents; tracked by UV-VIS spectrometer.

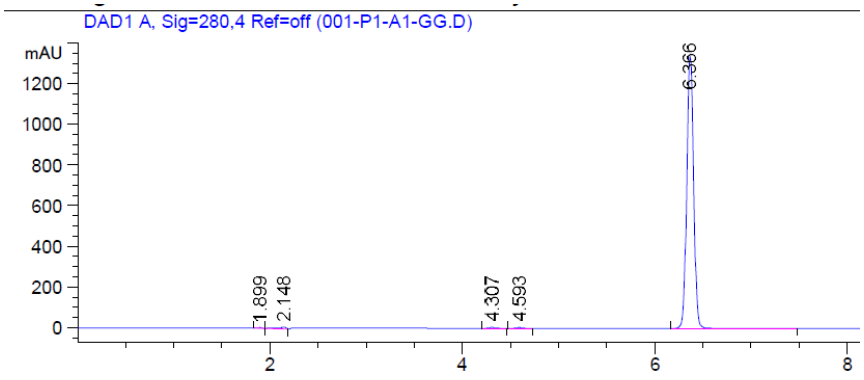

Figure 5-12. HPLC of model compound GG, DaD at 280 nm.

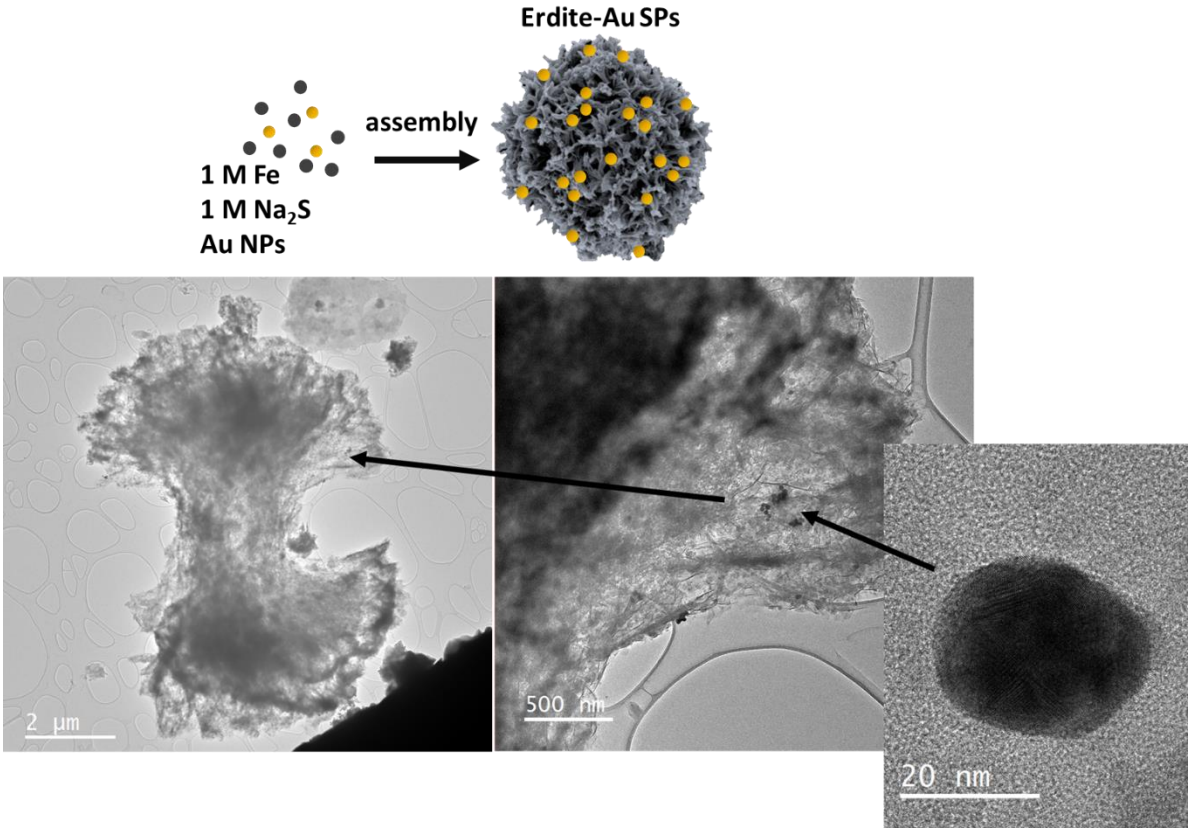

Figure 5-13. Synthesis scheme and TEM of Au-erdite SPs.

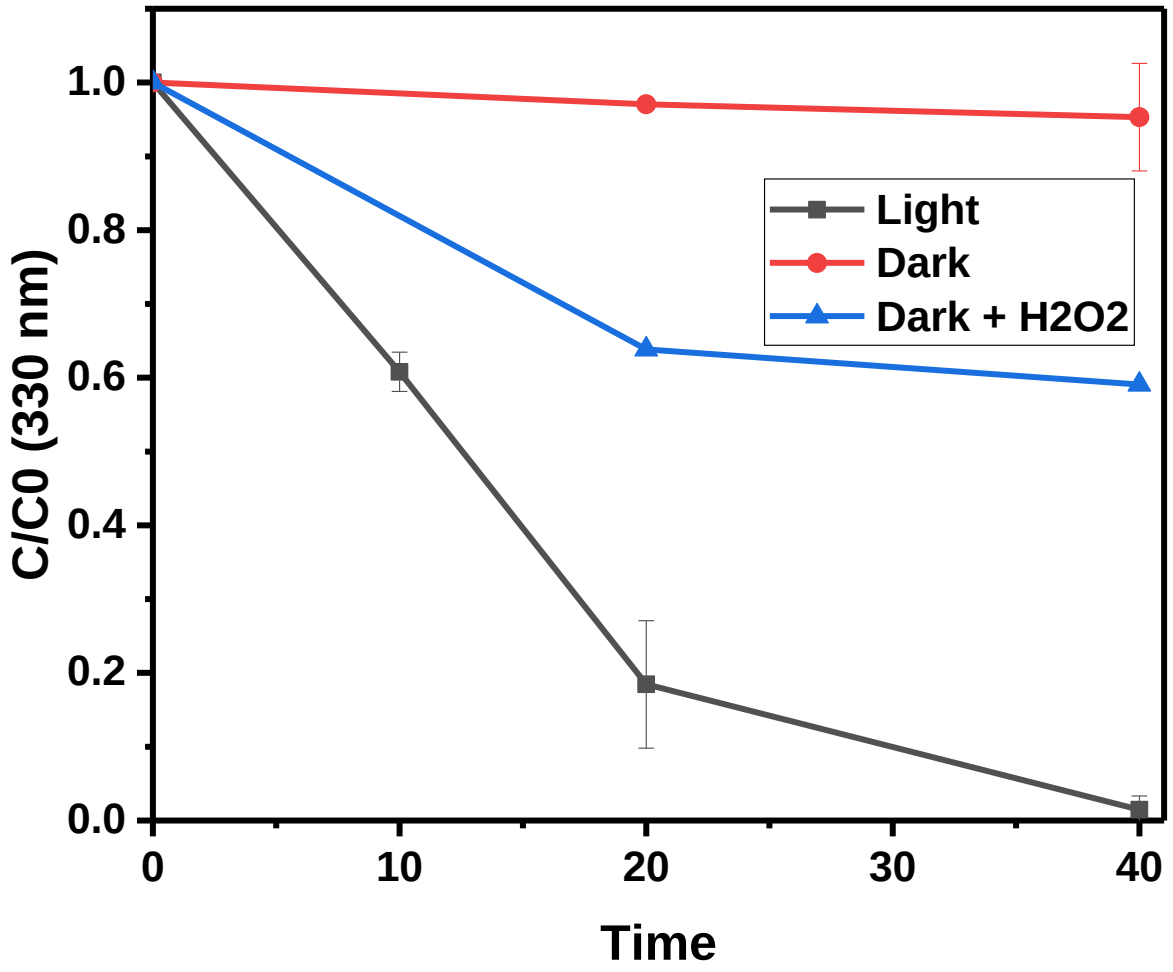

Figure 5-14. Catalysis with Au-erdite SPs with UV light at 302 nm, in the dark with no peroxide and in the dark with peroxide.

Chapter 6

Conclusions and Future Work

6.1 Conclusions

The primary focus of this dissertation was to fabricate biomimetic suprastructures and explore their potential as photocatalysts. By taking advantage of the fundamental electrostatic interactions within the system, NP properties were tuned to conveniently fabricate hierarchical structures that mimic the structural complexity and functionality of materials found in nature. Thereby, a variety of semiconductor synthesis and assembly methods were established, offering immense tunability in the overall shape and size of SPs. Due to the general nature of supraparticles, which can be defined as complexes composed of two or more subunits or constituents, the composition of NPs within the SP was controllable, offering an additional level of design flexibility. Several key components were considered necessary when engineering SPs for catalytic application, including, facile and cost-effective synthesis method, absorption range, dispersion stability, and structural tunability.

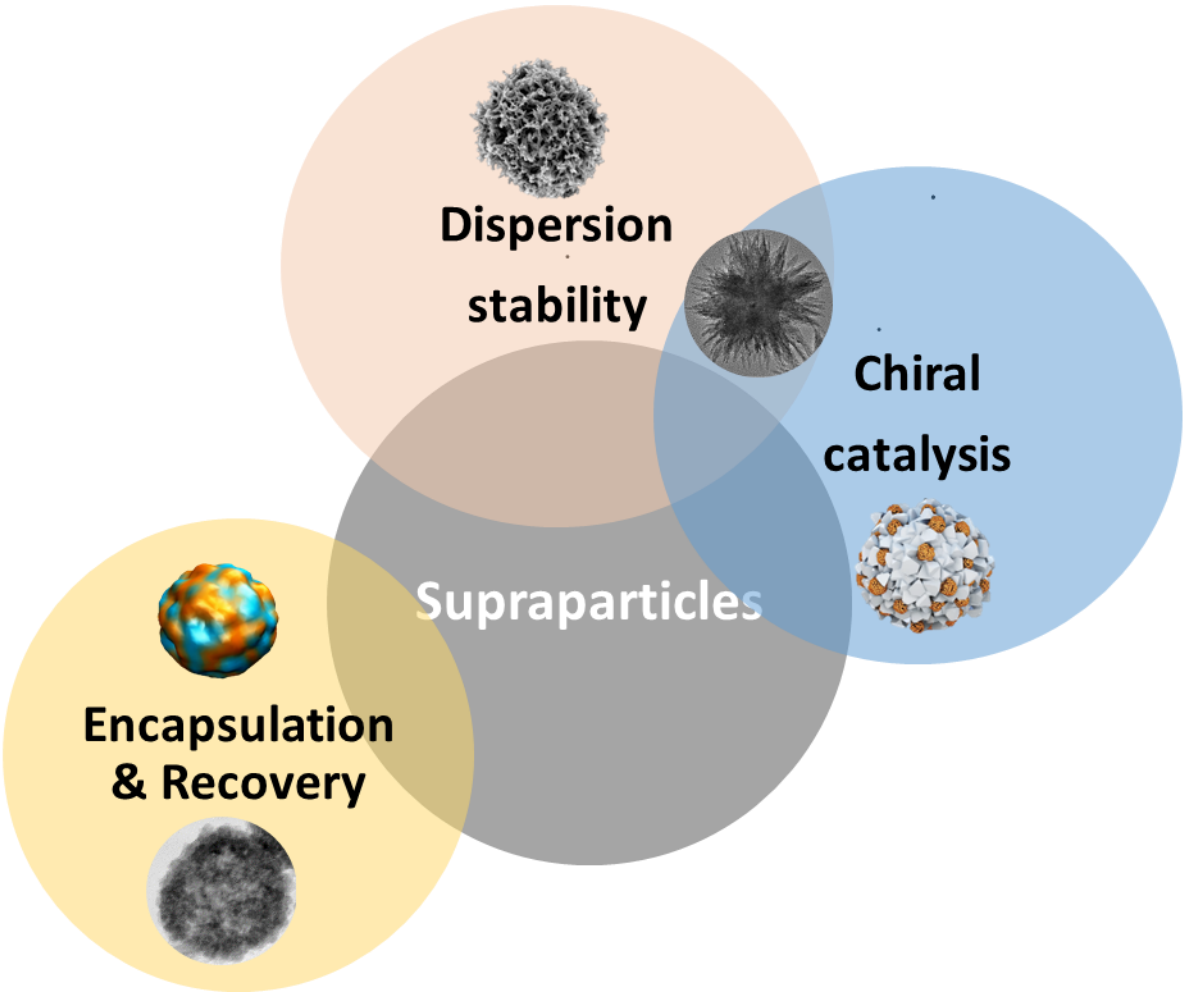

Figure 6-1. Diagram summarizing SPs formed throughout this work and some of their associated properties

In chapter 2, it was proposed that any combination of enzymes, nature's catalyst, and NPs would result in terminal SP assembly considering there was a balance between the electrostatic repulsion and attractive van der Waals interactions in the system. Thereby, five hybrid assemblies were fabricated from CdTe, ZnO, and FeS_2 NPs with protease, CytC, and FAHD proteins. Hybrid SPs exhibited the ability to encapsulate and protect the protein within the assembly while displaying similar catalytic activity in conditions deemed unfavorable to the protein. This worked

inspired the remaining assemblies by showcasing the design flexibility available within SPs. Thus, the remaining chapters focused on tuning assemblies for a range of photocatalytic reactions.

In Chapters 3 – 5, SPs were constructed from a range of semiconductors, all displaying different properties and catalytic potentials, across multiple length scales. In Chapter 3, chiral ZnS SPs were synthesized and used for the enantioselective degradation of tyrosine at considerably higher rates than any other inorganic particle. Addition of chiral Au NPs to the SP resulted in better photocatalytic performance as plasmonic contributions were employed. In Chapter 4, CdS SPs with tunable spike length and density were synthesized and self-assembled through an oriented attachment method. Spiky particles demonstrated up- and down-conversion PL emission, which was utilized for the degradation of an organic contaminant, RhB, with notable activity under infrared light. Lastly, in Chapter 5, the synthesis and self-assembly of erdite SPs was demonstrated. The assembly of erdite into complex hierarchical structures was reported for the first time and described using a recently developed technique (applying graph theory) to evaluate the complexity of NP assemblies. Taking advantage of iron in erdite, the SPs were employed as a photo-Fenton catalyst for the degradation of methylene blue and a lignin model compound. The particles displayed excellent recyclability for a Fenton catalyst (55 cycles) and improved performance with the addition of Au NPs.

Overall, the versatility and flexibility that can be introduced into the design of SP assemblies was demonstrated. From the unexpected combination of NPs and proteins to the self-assembly of multi-component systems that display improved and collective properties when compared to their constituents. The combinations become endless once the right conditions are established, which this thesis showcases to be a facile process. Thus, SPs can be a convenient platform for engineering

catalysts using different NPs as functional modules, leading to the development of more specific and sophisticated SP assemblies that can replicate multiple functions of biological nanoassemblies.

6.2 Future Directions

Expansion of Chiral SPs for enantiomeric selectivity

The results for the chiral ZnS system were exciting and novel, leading to immense interest in similar chiral systems and other targeted substrates. It is expected that similar chiral SPs can be assembled and exhibit enantiomeric selectivity of chiral substrates. To examine the design flexibility of these systems, NPs can be synthesized with different chiral ligands of similar sizes, for example, other amino acids. This will further examine the creation of interstitial gaps between NPs in SPs, which are assumed to be critical for forming chiral centers similar to enzymes, leading to enantiomeric selectivity. One example is demonstrated for the spiky CdS SPs, composed of L/D – cysteine capped NPs, which also exhibit chirality for the assembled SP. Further studies may consider the selectivity of the catalytic reaction when the ligands and composition of the NPs are varied. It would also be interesting to explore how the length of chiral ligand may affect catalytic potential of SPs, and how varying the gap size may allow for versality in the size of substrates.

Mass Transport Implications

Mass transport of substrates, intermediates, or products is critical in catalytic reactions. The proximity of NPs in SPs and interstitial gaps that are created is expected to facilitate the diffusion of reactants and intermediate products in these systems. While it is known that NPs in SPs exhibit collective and synergistic properties that are different from individual NPs or bulk components,

leading to exceptional activity, gaining information on the contribution of mass transport in the system would be insightful. Understanding the role of reactant and intermediate species may help in the design of new, optimized SPs.

Translation from Computational Design Predictions

The degree of flexibility presented by SPs allows for a range of interesting and sophisticated assemblies that display improved functionality. One may consider the impact of combining constituents based on predictions proposed by a computational study. For instance, Sabatier's principle predicts the optimal catalysis of a reaction based on the interactions between the catalyst and substrate. These results are generally presented on 'volcano' plots, with increasing potential of a material. Smart combinations of multi-components from these plots have the potential to increase the activity, along with the selectivity.[222] While computational design can help narrow a range of efficient catalyst, SP's design flexibility, not only allows for a facile combination of those components but it offers the benefit of synergistic and collective properties that are widely recognized in these assemblies.[7–9,34]

Thermal Catalysts

Another area of catalysis that may be considered for the implementation of SPs is thermal systems. Current catalysts are hindered by their lack of thermal stability, which leads to aggregation during reactions.[7] The most common catalyst used in industrial applications are noble metal particles on oxide supports,[8] however, they are also plagued by thermal instability. This instability causes particles to sinter and form large irreversible aggregates during reactions. Aggregation of particles results in the reduction of overall surface area and partial deactivation, leading to a decrease in

catalytic activity. To alleviate this problem, the development of SPs can be implemented as catalyst to address the issue of aggregation by separating metal particles from each other while keeping them immobilized.[7]

Bibliography

1. Ishii, D. *et al.* Chaperonin-mediated stabilization and ATP-triggered release of semiconductor nanoparticles. *Nature* **423**, 628–32 (2003).
2. Kotov, N. A. Inorganic Nanoparticles as Protein Mimics. *Science* **330**, 188–189 (2010).
3. Xia, Y. *et al.* Self-assembly of self-limiting monodisperse supraparticles from polydisperse nanoparticles. *Nat. Nanotechnol.* **6**, 580–587 (2011).
4. Park, J. Il *et al.* Terminal supraparticle assemblies from similarly charged protein molecules and nanoparticles. *Nat. Commun.* **5**, (2014).
5. Silveira, G. D. Q. *et al.* Supraparticle Nanoassemblies with Enzymes. *Chem. Mater.* **31**, 7493–7500 (2019).
6. Xia, Y. & Tang, Z. Monodisperse inorganic supraparticles: formation mechanism, properties and applications. *Chem. Commun. (Camb).* **48**, 6320–6336 (2012).
7. Hu, Y., Liu, Y. & Sun, Y. Mesoporous Colloidal Superparticles of Platinum-Group Nanocrystals with Surfactant-Free Surfaces and Enhanced Heterogeneous Catalysis. *Adv. Funct. Mater.* **25**, 1638–1647 (2015).
8. Chen, C. *et al.* Mesoporous multicomponent nanocomposite colloidal spheres: ideal high-temperature stable model catalysts. *Angew. Chem. Int. Ed. Engl.* **50**, 3725–9 (2011).
9. Qin, G. W. *et al.* Enhanced Catalytic Activity of Pt Nanomaterials: From Monodisperse Nanoparticles to Self-Organized Nanoparticle-Linked Nanowires. *J. Phys. Chem. C* **114**, 6909–6913 (2010).
10. Whitesides, G. M. & Boncheva, M. Beyond molecules: Self-assembly of mesoscopic and macroscopic components. *Proc. Natl. Acad. Sci. U. S. A.* **99**, 4769–4774 (2002).
11. Hormoz, S. & Brenner, M. P. Design principles for self-assembly with short-range interactions. *Proc. Natl. Acad. Sci. U. S. A.* **108**, 5193–5198 (2011).
12. Jankowski, E. & Glotzer, S. C. Screening and designing patchy particles for optimized self-assembly propensity through assembly pathway engineering. *Soft Matter* **8**, 2852–2859 (2012).
13. Piccinini, E., Pallarola, D., Battaglini, F. & Azzaroni, O. Recognition-driven assembly of self-limiting supramolecular protein nanoparticles displaying enzymatic activity. *Chem. Commun. (Camb).* **51**, 14754–7 (2015).
14. Zhang, Q., Chou, T. P., Russo, B., Jenekhe, S. A. & Cao, G. Polydisperse Aggregates of ZnO Nanocrystallites: A Method for Energy-Conversion-Efficiency Enhancement in Dye-Sensitized Solar Cells. *Adv. Funct. Mater.* **18**, 1654–1660 (2008).
15. Wang, T. *et al.* Self-assembled colloidal superparticles from nanorods. *Science* **338**, 358–63 (2012).
16. Wang, Y. *et al.* Mesoporous silica supraparticles for sustained inner-ear drug delivery. *Small* **10**, 4244–8 (2014).
17. Banin, U. & Sitt, A. Colloidal self-assembly: Superparticles get complex. *Nat. Mater.* **11**,

1009–11 (2012).
18. Li, F., Josephson, D. P. & Stein, A. Colloidal assembly: The road from particles to colloidal molecules and crystals. *Angewandte Chemie - International Edition* vol. 50 360–388 (2011).
19. Piccinini, E., Pallarola, D., Battaglini, F. & Azzaroni, O. Self-limited self-assembly of nanoparticles into supraparticles: towards supramolecular colloidal materials by design. *Mol. Syst. Des. Eng.* **1**, 155–162 (2016).
20. Wu, S. *et al.* Byproduct-induced in-situ formation of gold colloidal superparticles. *Sci China Mater* **58**, 860–866 (2015).
21. Yufang Zhu, Wenru Zhao, Hangrong Chen, and & Shi*, J. A Simple One-Pot Self-Assembly Route to Nanoporous and Monodispersed Fe3O4 Particles with Oriented Attachment Structure and Magnetic Property. (2007) doi:10.1021/JP0676843.
22. Lu, C. & Tang, Z. Advanced Inorganic Nanoarchitectures from Oriented Self-Assembly. *Adv. Mater.* **28**, 1096–1108 (2016).
23. Niederberger, M. & Coïfen, H. Oriented attachment and mesocrystals: Non-classical crystallization mechanisms based on nanoparticle assembly. (2006) doi:10.1039/b604589h.
24. Zhang, Z., Tang, Z., Kotov, N. A. & Glotzer, S. C. Simulations and analysis of self-assembly of CdTe nanoparticles into wires and sheets. *Nano Lett.* **7**, 1670–5 (2007).
25. Wu, W., Changzhong Jiang & Roy, V. A. L. Recent progress in magnetic iron oxide-semiconductor composite nanomaterials as promising photocatalysts. *Nanoscale* **7**, 38–58 (2015).
26. Sun, Y.-Q. *et al.* Complete Au@ZnO Core-Shell Nanoparticles with Enhanced Plasmonic Absorption Enabling Significantly Improved Photocatalysis. *Nanoscale* (2016) doi:10.1039/C6NR00933F.
27. Li, X.-H., Li, J.-X., Li, G.-D., Liu, D.-P. & Chen, J.-S. Controlled synthesis, growth mechanism, and properties of monodisperse CdS colloidal spheres. *Chemistry* **13**, 8754–61 (2007).
28. Bigall, N. C. *et al.* Monodisperse platinum nanospheres with adjustable diameters from 10 to 100 nm: synthesis and distinct optical properties. *Nano Lett.* **8**, 4588–92 (2008).
29. Jutz, G. & Böker, A. Bionanoparticles as functional macromolecular building blocks – A new class of nanomaterials. *Polymer (Guildf).* **52**, 211–232 (2011).
30. Asuri, P., Karajanagi, S. S., Vertegel, A. A., Dordick, J. S. & Kane, R. S. Enhanced stability of enzymes adsorbed onto nanoparticles. *J. Nanosci. Nanotechnol.* **7**, 1675–8.
31. Lynch, I. & Dawson, K. A. Protein-nanoparticle interactions. *Nano Today* **3**, 40–47 (2008).
32. Moerz, S. T., Kraegeloh, A., Chanana, M. & Kraus, T. Formation Mechanism for Stable Hybrid Clusters of Proteins and Nanoparticles. *ACS Nano* **9**, 6696–705 (2015).
33. Sevilla, P., Sánchez-Cortés, S., García-Ramos, J. V & Feis, A. Concentration-controlled formation of myoglobin/gold nanosphere aggregates. *J. Phys. Chem. B* **118**, 5082–92 (2014).
34. Kalekar, A. M. *et al.* Investigation into the Catalytic Activity of Porous Platinum Nanostructures. *Langmuir* **29**, 11431–9 (2013).
35. Vargesson, N. Thalidomide-induced teratogenesis: History and mechanisms. *Birth Defects Research Part C - Embryo Today: Reviews* vol. 105 140–156 (2015).
36. Lidmar, J., Mirny, L. & Nelson, D. R. Virus shapes and buckling transitions in spherical shells. *Phys. Rev. E* **68**, 051910 (2003).
37. Scott, C. C., Vacca, F. & Gruenberg, J. Endosome maturation, transport and functions.

Semin. Cell Dev. Biol. **31**, 2–10 (2014).
38. van der Pol, E., Boing, A. N., Harrison, P., Sturk, A. & Nieuwland, R. Classification, Functions, and Clinical Relevance of Extracellular Vesicles. *Pharmacol. Rev.* **64**, 676–705 (2012).
39. Vogelmann, T. C. & Evans, J. R. Profiles of light absorption and chlorophyll within spinach leaves from chlorophyll fluorescence. *Plant, Cell Environ.* **25**, 1313–1323 (2002).
40. Yeates, T. O., Kerfeld, C. A., Heinhorst, S., Cannon, G. C. & Shively, J. M. Protein-based organelles in bacteria: carboxysomes and related microcompartments. *Nat. Rev. Microbiol.* **6**, 681–691 (2008).
41. Aumiller, W. M., Uchida, M. & Douglas, T. Protein cage assembly across multiple length scales. *Chem. Soc. Rev.* **47**, 3433–3469 (2018).
42. Webber, M. J. & Langer, R. Drug delivery by supramolecular design. *Chem. Soc. Rev.* **46**, 6600–6620 (2017).
43. De, M. & Rotello, V. M. Synthetic "chaperones": nanoparticle-mediated refolding of thermally denatured proteins. *Chem. Commun.* **0**, 3504 (2008).
44. Borwankar, A. U. *et al.* Tunable equilibrium nanocluster dispersions at high protein concentrations. *Soft Matter* **9**, 1766–1771 (2013).
45. Park, W. M. & Champion, J. A. Colloidal Assembly of Hierarchically Structured Porous Supraparticles from Flower-Shaped Protein–Inorganic Hybrid Nanoparticles. *ACS Nano* **10**, 8271–8280 (2016).
46. Mout, R. *et al.* Programmed Self-Assembly of Hierarchical Nanostructures through Protein–Nanoparticle Coengineering. *ACS Nano* **11**, 3456–3462 (2017).
47. Yousefi, A. M., Zhou, Y., Querejeta-Fernández, A., Sun, K. & Kotov, N. A. Streptavidin inhibits self-assembly of CdTe nanoparticles. *J. Phys. Chem. Lett.* **3**, 3249–3256 (2012).
48. Iyer, P. V. & Ananthanarayan, L. Enzyme stability and stabilization—Aqueous and non-aqueous environment. *Process Biochem.* **43**, 1019–1032 (2008).
49. Krajewska, B. Application of chitin- and chitosan-based materials for enzyme immobilizations: A review. *Enzyme Microb. Technol.* **35**, 126–139 (2004).
50. Puthussery, J., Seefeld, S., Berry, N., Gibbs, M. & Law, M. Supporting Information for Colloidal Iron Pyrite (FeS 2) Nanocrystal Inks for Thin Film Photovoltaics. *J. Am. Chem. Soc.* **133**, S1–S9 (2011).
51. Bai, Y. *et al.* Universal synthesis of single-phase pyrite FeS2 nanoparticles, nanowires, and nanosheets. *J. Phys. Chem. C* **117**, 2567–2573 (2013).
52. McGuffie, M. J. *et al.* Zinc oxide nanoparticle suspensions and layer-by-layer coatings inhibit staphylococcal growth. *Nanomedicine Nanotechnology, Biol. Med.* **12**, 33–42 (2016).
53. Gaponik, N. Thiol-capping of CdTe nanocrystals: an alternative to organometallic synthetic routes. *J. Phys. Chem. B* **106**, (2002).
54. Plimpton, S. Fast parallel algorithms for short-range molecular dynamics. *J. Comput. Phys.* **117**, 1–19 (1995).
55. Brown, W. M., Wang, P., Plimpton, S. J. & Tharrington, A. N. Implementing molecular dynamics on hybrid high performance computers - Short range forces. *Comput. Phys. Commun.* **182**, 898–911 (2011).
56. Yin, L., Hsu, T. & Jiang, S. Characterization of Acidic Protease from Aspergillus niger BCRC 32720. (2013) doi:10.1021/jf3041726.
57. Haas, A. S. *et al.* Cytochrome c and Cytochrome c Oxidase: Monolayer Assemblies and

Catalysis. *J. Phys. Chem. B* **105**, 11351–11362 (2001).
58. Lu, Y., Jiang, Z., Xu, S. & Wu, H. Efficient conversion of CO 2 to formic acid by formate dehydrogenase immobilized in a novel alginate – silica hybrid gel. *Enzyme* **115**, 263–268 (2006).
59. Tang, Z., Zhang, Z., Wang, Y., Glotzer, S. C. & Kotov, N. a. Self-assembly of CdTe nanocrystals into free-floating sheets. *Science* **314**, 274–278 (2006).
60. Kittler, S. *et al.* The influence of proteins on the dispersability and cell-biological activity of silver nanoparticles. *J. Mater. Chem.* **20**, 512 (2010).
61. Saptarshi, S. R., Duschl, A. & Lopata, A. L. Interaction of nanoparticles with proteins: relation to bio-reactivity of the nanoparticle. *J. Nanobiotechnology* **11**, 26 (2013).
62. Lakowicz, J. R. Protein Fluorescence. in *Principles of Fluorescence Spectroscopy* 529–575 (Springer US, 2006). doi:10.1007/978-0-387-46312-4_16.
63. Silvera Batista, C. A., Larson, R. G. & Kotov, N. A. Nonadditivity of nanoparticle interactions. *Science (80-.).* **350**, 1242477 (2015).
64. Nguyen, T. D., Schultz, B. A., Kotov, N. A. & Glotzer, S. C. Generic, phenomenological, on-the-fly renormalized repulsion model for self-limited organization of terminal supraparticle assemblies. *Proc. Natl. Acad. Sci. U. S. A.* **112**, (2015).
65. Jones, L. J., Upson, R. H., Haugland, R. P., Panchuk-Voloshina, N. & Zhou, M. Quenched BODIPY dye-labeled casein substrates for the assay of protease activity by direct fluorescence measurement. *Anal. Biochem.* **251**, 144–52 (1997).
66. Sanatan, P. T., Lomate, P. R., Giri, A. P. & Hivrale, V. K. Characterization of a chemostable serine alkaline protease from Periplaneta americana. *BMC Biochem.* **14**, 32 (2013).
67. Misteli, T. The concept of self-organization in cellular architecture. *J. Cell Biol.* **155**, 181–185 (2001).
68. Soto, G. E. & Hultgren, S. J. Bacterial adhesins: common themes and variations in architecture and assembly. *J. Bacteriol.* **181**, 1059–71 (1999).
69. Palade, G. Intracellular Aspects of the Process of Protein Synthesis. *Science (80-.).* **189**, 867–867 (1975).
70. Eschenmoser, A. & Loewenthal, E. Chemistry of potentially prebiological natural products. *Chem. Soc. Rev.* **21**, 1 (1992).
71. Tanaka, S. *et al.* Atomic-level models of the bacterial carboxysome shell. *Science* **319**, 1083–6 (2008).
72. Brown, W. J., Shannon, W. A. & Snell, W. J. Specific and azurophilic granules from rabbit polymorphonuclear leukocytes. I. Isolation and characterization of membrane and content subfractions. *J. Cell Biol.* **96**, 1030–9 (1983).
73. Settembre, C., Fraldi, A., Medina, D. L. & Ballabio, A. Signals from the lysosome: A control centre for cellular clearance and energy metabolism. *Nat. Rev. Mol. Cell Biol.* **14**, 283–296 (2013).
74. Buchan, J. R., Kolaitis, R.-M., Taylor, J. P. & Parker, R. Eukaryotic Stress Granules Are Cleared by Autophagy and Cdc48/VCP Function. *Cell* **153**, 1461–1474 (2013).
75. Buchan, J. R. & Parker, R. Eukaryotic Stress Granules: The Ins and Outs of Translation. *Mol. Cell* **36**, 932–941 (2009).
76. Wheeler, J. R., Matheny, T., Jain, S., Abrisch, R. & Parker, R. Distinct stages in stress granule assembly and disassembly. *Elife* **5**, (2016).
77. Brangwynne, C. P. Phase transitions and size scaling of membrane-less organelles. *J. Cell Biol.* **203**, 875–881 (2013).

78. Feric, M. *et al.* Coexisting Liquid Phases Underlie Nucleolar Subcompartments. *Cell* **165**, 1686–1697 (2016).
79. Brangwynne, C. P. *et al.* Germline P granules are liquid droplets that localize by controlled dissolution/condensation. *Science (80-.).* **324**, 1729–1732 (2009).
80. MELIS, A., Spangfort, M. & Andersson, B. Light-Absorption and Electron-Transport Balance Between Photosystem Ii and Photosystem I in Spinach Chloroplasts. *Photochem. Photobiol.* **45**, 129–136 (1987).
81. Shen, X., Zhang, K. & Kaufman, R. J. The unfolded protein response - A stress signaling pathway of the endoplasmic reticulum. *J. Chem. Neuroanat.* **28**, 79–92 (2004).
82. Harding, H. P., Zhang, Y. & Ron, D. Protein translation and folding arecoupledbyan endoplasmic-reticulum- resident kinase. *Nature* **397**, 271–274 (1999).
83. Xu, X. *et al.* ROS-Responsive Polyprodrug Nanoparticles for Triggered Drug Delivery and Effective Cancer Therapy. *Adv. Mater.* **29**, 1700141 (2017).
84. Wu, M. X. & Yang, Y. W. Metal–Organic Framework (MOF)-Based Drug/Cargo Delivery and Cancer Therapy. *Adv. Mater.* **29**, 1–20 (2017).
85. Anselmo, A. C. & Mitragotri, S. Impact of particle elasticity on particle-based drug delivery systems. *Adv. Drug Deliv. Rev.* **108**, 51–67 (2017).
86. Agnes, M. *et al.* A chiroptical molecular sensor for ferrocene. *Chem. Commun.* **52**, 11492–11495 (2016).
87. Caricato, M. *et al.* Chiral nanostructuring of multivalent macrocycles in solution and on surfaces. *Org. Biomol. Chem.* **13**, 3593–3601 (2015).
88. Han, D. *et al.* DNA Origami with Complex Curvatures in Three-Dimensional Space. *Science (80-.).* **332**, 342–346 (2011).
89. Mikkilä, J. *et al.* Virus-Encapsulated DNA Origami Nanostructures for Cellular Delivery. *Nano Lett.* **14**, 2196–2200 (2014).
90. Han, D. *et al.* DNA Gridiron Nanostructures Based on Four-Arm Junctions. *Science (80-.).* **339**, 1412–1415 (2013).
91. Zhao, Z. *et al.* Nanocaged enzymes with enhanced catalytic activity and increased stability against protease digestion. *Nat. Commun.* **7**, 10619 (2016).
92. Sørensen, M. A., Fehler, A. O. & Lo Svenningsen, S. Transfer RNA instability as a stress response in Escherichia coli : Rapid dynamics of the tRNA pool as a function of demand. *RNA Biol.* **15**, 586–593 (2018).
93. Lindahl, T. Instability and decay of the primary structure of DNA. *Nature* **362**, 709–715 (1993).
94. Kotov, N. A. Chemistry. Inorganic nanoparticles as protein mimics. *Science* **330**, 188–9 (2010).
95. Kotov, N. A. Self-assembly of inorganic nanoparticles: Ab ovo. *EPL (Europhysics Lett.* **119**, 66008 (2017).
96. Xia, Y. *et al.* supraparticles from polydisperse nanoparticles. *Nat. Nanotechnol.* **6**, 580–587 (2011).
97. Grason, G. M. Perspective: Geometrically frustrated assemblies. *J. Chem. Phys.* **145**, 110901 (2016).
98. Yang, M. *et al.* Self-assembly of nanoparticles into biomimetic capsid-like nanoshells. *Nat. Chem.* **9**, 287–294 (2017).
99. Zhou, H., Kim, J.-P., Bahng, J. H., Kotov, N. A. & Lee, J. Self-Assembly Mechanism of Spiky Magnetoplasmonic Supraparticles. *Adv. Funct. Mater.* **24**, 1439–1448 (2014).

100. Bryant, D. A. & Frigaard, N.-U. Prokaryotic photosynthesis and phototrophy illuminated. *Trends Microbiol.* **14**, 488–496 (2006).
101. Kober, L., Zehe, C. & Bode, J. Development of a novel ER stress based selection system for the isolation of highly productive clones. *Biotechnol. Bioeng.* **109**, 2599–2611 (2012).
102. Noyori, R. & Takaya, H. BINAP: An Efficient Chiral Element for Asymmetric Catalysis. *Acc. Chem. Res.* **23**, 345–350 (1990).
103. Ma, W. *et al.* Chiral Inorganic Nanostructures. *Chem. Rev.* **117**, 8041–8093 (2017).
104. Han, X. *et al.* Chiral Covalent Organic Frameworks with High Chemical Stability for Heterogeneous Asymmetric Catalysis. *J. Am. Chem. Soc.* **139**, 8693–8697 (2017).
105. Miaskiewicz, S., Reed, J. H., Donets, P. A., Oliveira, C. C. & Cramer, N. Chiral 1,3,2-Diazaphospholenes as Catalytic Molecular Hydrides for Enantioselective Conjugate Reductions. *Angew. Chemie Int. Ed.* **57**, 4039–4042 (2018).
106. Wu, C.-D. & Zhao, M. Incorporation of Molecular Catalysts in Metal-Organic Frameworks for Highly Efficient Heterogeneous Catalysis. *Adv. Mater.* **29**, 1605446 (2017).
107. Hu, A., Yee, G. T. & Lin, W. Magnetically recoverable chiral catalysts immobilized on magnetite nanoparticles for asymmetric hydrogenation of aromatic ketones. *J. Am. Chem. Soc.* **127**, 12486–12487 (2005).
108. Oila, M. J. Chirally modified gold nanoparticles: nanostructured chiral ligands for catalysis. *Arkivoc* **2006**, 76–83 (2006).
109. Gross, E. *et al.* Asymmetric catalysis at the mesoscale: Gold nanoclusters embedded in chiral self-assembled monolayer as heterogeneous catalyst for asymmetric reactions. *J. Am. Chem. Soc.* **135**, 3881–3886 (2013).
110. Sawai, K., Tatumi, R., Nakahodo, T. & Fujihara, H. Asymmetric Suzuki-Miyaura Coupling Reactions Catalyzed by Chiral Palladium Nanoparticles at Room Temperature. *Angew. Chemie Int. Ed.* **47**, 6917–6919 (2008).
111. Hou, J. *et al.* Catalyzed and Electrocatalyzed Oxidation of l -Tyrosine and l -Phenylalanine to Dopachrome by Nanozymes. *Nano Lett.* **18**, 4015–4022 (2018).
112. Chen, J. *et al.* One-pot Synthesis of CdS Nanocrystals Hybridized with Single-Layer Transition-Metal Dichalcogenide Nanosheets for Efficient Photocatalytic Hydrogen Evolution. *Angew. Chemie Int. Ed.* **54**, 1210–1214 (2015).
113. Qi, P. *et al.* Catalysis and Reactivation of Ordered Mesoporous Carbon-Supported Gold Nanoparticles for the Base-Free Oxidation of Glucose to Gluconic Acid. *ACS Catal.* **5**, 2659–2670 (2015).
114. Tao, Y., Ju, E., Ren, J. & Qu, X. Bifunctionalized mesoporous silica-supported gold nanoparticles: Intrinsic oxidase and peroxidase catalytic activities for antibacterial applications. *Adv. Mater.* **27**, 1097–1104 (2015).
115. Wang, Y. *et al.* Atomically Precise Alkynyl-Protected Metal Nanoclusters as a Model Catalyst: Observation of Promoting Effect of Surface Ligands on Catalysis by Metal Nanoparticles. *J. Am. Chem. Soc.* **138**, 3278–3281 (2016).
116. Gawande, M. B. *et al.* Cu and Cu-Based Nanoparticles: Synthesis and Applications in Catalysis. *Chem. Rev.* **116**, 3722–3811 (2016).
117. Heinz, H. *et al.* Nanoparticle decoration with surfactants: Molecular interactions, assembly, and applications. *Surface Science Reports* (2017) doi:10.1016/j.surfrep.2017.02.001.
118. Heinz, H., Lin, T.-J., Kishore Mishra, R. & Emami, F. S. Thermodynamically Consistent Force Fields for the Assembly of Inorganic, Organic, and Biological Nanostructures: The INTERFACE Force Field. *Langmuir* **29**, 1754–1765 (2013).

119. Huang, J. & MacKerell, A. D. CHARMM36 all-atom additive protein force field: Validation based on comparison to NMR data. *J. Comput. Chem.* **34**, 2135–2145 (2013).
120. Liu, H. *et al.* Interaction of substituted poly(phenyleneethynylene)s with ligand-stabilized CdS nanoparticles. *J. Mater. Chem. A* (2014) doi:10.1039/c4ta01280a.
121. Chen, J. *et al.* Building two-dimensional materials one row at a time: Avoiding the nucleation barrier. *Science (80-.).* **362**, 1135–1139 (2018).
122. Phillips, J. C. *et al.* Scalable molecular dynamics with NAMD. *J. Comput. Chem.* **26**, 1781–1802 (2005).
123. Humphrey, W., Dalke, A. & Schulten, K. VMD: Visual molecular dynamics. *J. Mol. Graph.* **14**, 33–38 (1996).
124. Wattanakit, C. *et al.* Enantioselective recognition at mesoporous chiral metal surfaces. *Nat. Commun.* **5**, 3325 (2014).
125. Banerjee-Ghosh, K. *et al.* Separation of enantiomers by their enantiospecific interaction with achiral magnetic substrates. *Science (80-.).* **360**, 1331–1334 (2018).
126. Article, R. A Review on Zinc Sulphide Nanoparticles: From Synthesis, Properties to Applications. *J. Bioelectron. Nanotechnol.* **1**, 1–5 (2016).
127. Feng, W. *et al.* Assembly of mesoscale helices with near-unity enantiomeric excess and light-matter interactions for chiral semiconductors. *Sci. Adv.* **3**, e1601159 (2017).
128. Zhou, Y. *et al.* Biomimetic Hierarchical Assembly of Helical Suprapartcles from Chiral Nanoparticles. *ACS Nano* **10**, 3248–3256 (2016).
129. MacLean, M. W. A. *et al.* Unraveling Inter- and Intrachain Electronics in Polythiophene Assemblies Mediated by Coordination Nanospaces. *Angew. Chemie Int. Ed.* **55**, 708–713 (2016).
130. Yu, D. *et al.* Scalable synthesis of hierarchically structured carbon nanotube–graphene fibres for capacitive energy storage. *Nat. Nanotechnol.* **9**, 555–562 (2014).
131. Garcia-Viloca, M. How Enzymes Work: Analysis by Modern Rate Theory and Computer Simulations. *Science (80-.).* **303**, 186–195 (2004).
132. Mahmoud, S. F. & Bialkowski, S. E. Laser-Excited Fluorescence of Dityrosine. *Appl. Spectrosc.* **49**, 1669–1676 (1995).
133. Heineckes, J. W., Li, W., Daehnke, H. L. & Goldstein, J. A. Dityrosine, a Specific Marker of Oxidation, Is Synthesized by the Myeloperoxidase-Hydrogen Peroxide System of Human Neutrophils and MacrophagesDityrosine. *J. Biol. Chem.* **268**, 4069–4077 (1993).
134. Wood, A. T. & Hall, M. R. Reversed-phase high-performance liquid chromatography of catecholamines and indoleamines using a simple gradient solvent system and native fluorescence detection. *J. Chromatogr. B Biomed. Sci. Appl.* **744**, 221–225 (2000).
135. Lehrer, S. S. & Fasman, G. D. Ultraviolet Irradiation Effects in Poly-L-tyrosine and Model Compounds. Identification of Bityrosine as a Photoproduct. *Biochemistry* **6**, 757–767 (1967).
136. Cole, S. H. *et al.* Two functional but noncomplementing Drosophila tyrosine decarboxylase genes: Distinct roles for neural tyramine and octopamine in female fertility. *J. Biol. Chem.* **280**, 14948–14955 (2005).
137. Eickhoff, H., Jung, G. & Rieker, A. Oxidative phenol coupling—tyrosine dimers and libraries containing tyrosyl peptide dimers. *Tetrahedron* **57**, 353–364 (2001).
138. Reid, L. O. *et al.* A novel synthetic approach to tyrosine dimers based on pterin photosensitization. *Dye. Pigment.* **147**, 67–74 (2017).
139. Feringa, B. & Wynberg, H. Biomimetic asymmetric oxidative coupling of phenols. *Bioorg.*

Chem. **7**, 397–408 (1978).
140. Yutthalekha, T., Warakulwit, C., Limtrakul, J. & Kuhn, A. Enantioselective Recognition of DOPA by Mesoporous Platinum Imprinted with Mandelic Acid. *Electroanalysis* **27**, 2209–2213 (2015).
141. Zhang, Y. *et al.* One-step synthesis of chiral carbon quantum dots and their enantioselective recognition. *RSC Adv.* **6**, 59956–59960 (2016).
142. Wang, F., Gong, W., Wang, L. & Chen, Z. Selective recognition of d-tryptophan from d/l-tryptophan mixtures in the presence of Cu(II) by electropolymerized l-lysine film. *Anal. Biochem.* **492**, 30–33 (2016).
143. Harding, J. R., Amanchukwu, C. V., Hammond, P. T. & Shao Horn, Y. Instability of poly(ethylene oxide) upon oxidation in lithium air batteries. *J. Phys. Chem. C* **119**, 6947–6955 (2015).
144. Al-Janabi, N., Alfutimie, A., Siperstein, F. R. & Fan, X. Underlying mechanism of the hydrothermal instability of Cu3(BTC)2 metal-organic framework. *Front. Chem. Sci. Eng.* **10**, 103–107 (2016).
145. Zhang, Q. *et al.* Supernatant organics from anaerobic digestion after thermal hydrolysis cause direct and/or diffusional activity loss for nitritation and anammox. *Water Res.* **143**, 270–281 (2018).
146. Zoia, L., Bruschi, M., Orlandi, M., Tolppa, E. L. & Rindone, B. Asymmetric biomimetic oxidations of phenols: The mechanism of the diastereo- and enantioselective synthesis of thomasidioic acid. *Molecules* **13**, 129–148 (2008).
147. Cafferty, B. J. *et al.* Efficient Self-Assembly in Water of Long Noncovalent Polymers by Nucleobase Analogues. *J. Am. Chem. Soc.* **135**, 2447–2450 (2013).
148. Carnall, J. M. A. *et al.* Mechanosensitive self-replication driven by self-organization. *Science* **327**, 1502–6 (2010).
149. Keller, E. F. Self-Organization, Self-Assembly, and the Origin of Life. in *Mapping the Future of Biology* 131–140 (Springer Netherlands, 2009). doi:10.1007/978-1-4020-9636-5_9.
150. Heckl, W. M. Molecular Self-Assembly and the Origin of Life. in *Astrobiology* 361–372 (Springer Berlin Heidelberg, 2002). doi:10.1007/978-3-642-59381-9_23.
151. Segré, D., Ben-Eli, D., Deamer, D. W. & Lancet, D. The Lipid World. in *Origins of Life and Evolution of the Biosphere* vol. 31 119–145 (2001).
152. Zhang, S., Holmest, T., Lockshin, C. & Rich, A. Spontaneous assembly of a self-complementary oligopeptide to form a stable macroscopic membrane (,B-sheet/insoluble filaments/ionic bonds/origin of life/zuotin). *Chemistry (Easton).* **90**, 3334–3338 (1993).
153. Monnard, P.-A. & Deamer, D. W. Membrane Self-Assembly Processes : *Anat. Rec.* **207**, 196–207 (2002).
154. Chen, I. A. & Walde, P. From self-assembled vesicles to protocells. *Cold Spring Harbor perspectives in biology* vol. 2 (2010).
155. Wang, L., Xu, L., Kuang, H., Xu, C. & Kotov, N. A. Dynamic Nanoparticles Assemblies. *Acc Chem Res. Novemb.* **20**, 1916–1926 (2012).
156. Xu, L. *et al.* Nanoparticle assemblies: dimensional transformation of nanomaterials and scalability. *Chem. Soc. Rev.* **42**, 3114 (2013).
157. Podsiadlo, P., Shim, B. S. & Kotov, N. A. Polymer/clay and polymer/carbon nanotube hybrid organic–inorganic multilayered composites made by sequential layering of nanometer scale films. *Coord. Chem. Rev.* **253**, 2835–2851 (2009).

158. Talapin, D. V. *et al.* Quasicrystalline order in self-assembled binary nanoparticle superlattices. *Nature* **461**, 964–967 (2009).
159. Mann, S. Self-assembly and transformation of hybrid nano-objects and nanostructures under equilibrium and non-equilibrium conditions. *Nat. Mater.* **8**, 781–792 (2009).
160. Nie, Z., Petukhova, A. & Kumacheva, E. Properties and emerging applications of self-assembled structures made from inorganic nanoparticles. *Nat. Nanotechnol.* **5**, 15–25 (2010).
161. Li, M., Schnablegger, H. & Mann, S. Coupled synthesis and self-assembly of nanoparticles to give structures with controlled organization. *Nature* **402**, 393–395 (1999).
162. Wang, T., LaMontagne, D., Lynch, J., Zhuang, J. & Cao, Y. C. Colloidal superparticles from nanoparticle assembly. *Chem. Soc. Rev.* **42**, 2804–2823 (2013).
163. Wang, P. *et al.* Multivalent assembly of ultrasmall nanoparticles: One-, two-, and three-dimensional architectures of 2 nm gold nanoparticles. *Nano Res.* **5**, 283–291 (2012).
164. Devries, G. A. *et al.* Divalent metal nanoparticles. *Science* **315**, 358–61 (2007).
165. Ma, G. *et al.* Self-assembly of copper sulfide nanoparticles into nanoribbons with continuous crystallinity. *ACS Nano* **7**, 9010–8 (2013).
166. Nikolic, M. S. *et al.* Micelle and Vesicle Formation of Amphiphilic Nanoparticles. *Angew. Chemie Int. Ed.* **48**, 2752–2754 (2009).
167. Ge, R. *et al.* Fe3O4@polydopamine composite theranostic superparticles employing preassembled Fe3O4nanoparticles as the core. *ACS Appl. Mater. Interfaces* **8**, 22942–22952 (2016).
168. Iacovella, C. R. & Glotzer, S. C. Complex Crystal Structures Formed by the Self-Assembly of Ditethered Nanospheres. *Nano Lett.* **9**, 1206–1211 (2009).
169. Kalsin, A. M. *et al.* Electrostatic self-assembly of binary nanoparticle crystals with a diamond-like lattice. *Science* **312**, 420–4 (2006).
170. Shevchenko, E. V., Talapin, D. V., Kotov, N. A., O'Brien, S. & Murray, C. B. Structural diversity in binary nanoparticle superlattices. *Nature* **439**, 55–9 (2006).
171. Zhuang, J., Wu, H., Yang, Y. & Cao, Y. C. Controlling colloidal superparticle growth through solvophobic interactions. *Angew. Chem. Int. Ed. Engl.* **47**, 2208–12 (2008).
172. Li, S. *et al.* Single- and multi-component chiral supraparticles as modular enantioselective catalysts. *Nat. Commun.* **10**, 1–10 (2019).
173. Chen, O. *et al.* Magneto-fluorescent core-shell supernanoparticles. *Nat. Commun.* **5**, 5093 (2014).
174. Zhang, X. *et al.* Composite photothermal platform of polypyrrole-enveloped Fe 3O4 nanoparticle self-assembled superstructures. *ACS Appl. Mater. Interfaces* **6**, 14552–14561 (2014).
175. Liu, N. *et al.* A pomegranate-inspired nanoscale design for large-volume-change lithium battery anodes. *Nat. Nanotechnol.* **9**, 187–192 (2014).
176. Lee, S. H. *et al.* Self-Assembled Fe3O4 Nanoparticle Clusters as High-Performance Anodes for Lithium Ion Batteries via Geometric Confinement. *Nano Lett.* **13**, 4249–4256 (2013).
177. Chou, T. P., Zhang, Q., Fryxell, G. E. & Cao, G. Z. Hierarchically Structured ZnO Film for Dye-Sensitized Solar Cells with Enhanced Energy Conversion Efficiency. *Adv. Mater.* **19**, 2588–2592 (2007).
178. Elena V. Shevchenko, † *et al.* Self-Assembled Binary Superlattices of CdSe and Au Nanocrystals and Their Fluorescence Properties. (2008) doi:10.1021/JA710619S.
179. Penn, R. L. & Banfield, J. F. Morphology development and crystal growth in

nanocrystalline aggregates under hydrothermal conditions: insights from titania. *Geochim. Cosmochim. Acta* **63**, 1549–1557 (1999).
180. Ferris, J. P. Montmorillonite catalysis of 30-50 mer oligonucleotides: Laboratory demonstration of potential steps in the origin of the RNA world. *Orig. Life Evol. Biosph.* **32**, 311–332 (2002).
181. Jin, J., Yu, J., Liu, G. & Wong, P. K. Single crystal CdS nanowires with high visible-light photocatalytic H2-production performance. *J. Mater. Chem. A* **1**, 10927 (2013).
182. Yu, J., Yu, Y. & Cheng, B. Enhanced visible-light photocatalytic H2-production performance of multi-armed CdS nanorods. *RSC Adv.* **2**, 11829 (2012).
183. Ya-Dong Li, * *et al.* Nonaqueous Synthesis of CdS Nanorod Semiconductor. (1998) doi:10.1021/CM970789L.
184. Vaquero, F., Navarro, R. M. & Fierro, J. L. G. Evolution of the nanostructure of CdS using solvothermal synthesis at different temperature and its influence on the photoactivity for hydrogen production. (2016) doi:10.1016/j.ijhydene.2015.12.039.
185. Vaquero, F., Navarro, R. M. M. & Fierro, J. L. G. L. G. Influence of the solvent on the structure, morphology and performance for H2 evolution of CdS photocatalysts prepared by solvothermal method. *Appl. Catal. B Environ.* **203**, 753–767 (2017).
186. Xu, D., Liu, Z., Liang, J. & Qian, Y. Solvothermal synthesis of CdS nanowires in a mixed solvent of ethylenediamine and dodecanethiol. *J. Phys. Chem. B* **109**, 14344–14349 (2005).
187. Chen, Q., Bao, H. & Shen, X. Phase transition of CdS in the presence of ethylenediamine and formation of hollow CdS submicron particles with needle-like structure. *Phase Transitions* (2008) doi:10.1080/01411590802051657.
188. Tian, Q., Yao, W., Wu, W. & Jiang, C. NIR light-activated upconversion semiconductor photocatalysts. *Nanoscale Horiz* **4**, 10 (2019).
189. Wu, M. *et al.* Solid-state infrared-to-visible upconversion sensitized by colloidal nanocrystals. *Nat. Photonics* **10**, 31–34 (2016).
190. Morozov, Y. V. *et al.* Defect-Mediated CdS Nanobelt Photoluminescence Up-Conversion. *J. Phys. Chem. C* **121**, 16607–16616 (2017).
191. Zhang, J., Li, D., Chen, R. & Xiong, Q. Laser cooling of a semiconductor by 40 kelvin. *Nature* **493**, 504–508 (2013).
192. Phuruangrat, A., Thongtem, T. & Thongtem, S. Characterisation of one-dimensional CdS nanorods synthesised by solvothermal method. *J. Exp. Nanosci.* **4**, 47–54 (2009).
193. Liebig, F., Thünemann, A. F. & Koetz, J. Ostwald Ripening Growth Mechanism of Gold Nanotriangles in Vesicular Template Phases. *Langmuir* **32**, 10928–10935 (2016).
194. Nguyen, T. D., Schultz, B. A., Kotov, N. A. & Glotzer, S. C. Generic, phenomenological, on-the-fly renormalized repulsion model for self-limited organization of terminal supraparticle assemblies. *Proc. Natl. Acad. Sci. U. S. A.* **112**, E3161-8 (2015).
195. Xiong, S. *et al.* Shape-Controlled Synthesis of 3D and 1D Structures of CdS in a Binary Solution withL-Cysteine's Assistance. *Chem. - A Eur. J.* **13**, 3076–3081 (2007).
196. Xiong, S. *et al.* Shape-controlled synthesis of 3D and ID structures of CdS in a binary solution with L-cysteine's assistance. *Chem. - A Eur. J.* **13**, 3076–3081 (2007).
197. Mahdi, M. A., Hassan, J. J., Ng, S. S. & Hassan, Z. Growth of CdS nanosheets and nanowires through the solvothermal method. *J. Cryst. Growth* **359**, 43–48 (2012).
198. Gai, H. *et al.* Solvothermal synthesis of CdS nanowires using L-cysteine as sulfur source and their characterization. *Appl. Phys. A Mater. Sci. Process.* **91**, 69–72 (2008).
199. Li, Y., Hu, Y., Peng, S., Lu, G. & Li, S. Synthesis of CdS nanorods by an ethylenediamine

assisted hydrothermal method for photocatalytic hydrogen evolution. *J. Phys. Chem. C* (2009) doi:10.1021/jp901505j.
200. Zhang, Y. & He, J. Facile synthesis of S, N co-doped carbon dots and investigation of their photoluminescence properties. *Phys. Chem. Chem. Phys.* **17**, 20154–20159 (2015).
201. Hu, X., Mohamood, T., Ma, W., Chen, C. & Zhao, J. Oxidative decomposition of rhodamine B dye in the presence of VO 2+ and/or Pt(IV) under visible light irradiation: N-deethylation, chromophore cleavage, and mineralization. *J. Phys. Chem. B* **110**, 26012–26018 (2006).
202. Czamanske, G.K. ; Leonard, B.F.; Clark, J. R. The crystal structure of erdite, NaFeS2·2H2O | American Mineralogist | GeoScienceWorld. https://pubs-geoscienceworld-org.proxy.lib.umich.edu/msa/ammin/article/65/5-6/516/104730/The-crystal-structure-of-erdite-NaFeS2-2H2O.
203. Zhu, S. *et al.* Addition of MnO2 in synthesis of nano-rod erdite promoted tetracycline adsorption. *Sci. Rep.* **9**, (2019).
204. Konnert, J. A., Evans, H. T. The crystal structure of erdite, NaFeSr'2HrO. (1980).
205. Lassin, A., Piantone, P., Crouzet, C., Bodénan, F. & Blanc, P. Estimated thermodynamic properties of NaFeS2 and erdite (NaFeS2:2H2O). *Appl. Geochemistry* **45**, 14–24 (2014).
206. Zhu, S. *et al.* Hydrothermal synthesis of a magnetic adsorbent from wasted iron mud for effective removal of heavy metals from smelting wastewater. *Environ. Sci. Pollut. Res.* **25**, 22710–22724 (2018).
207. Qu, Z. *et al.* Recycling of groundwater treatment sludge to prepare nano-rod erdite particles for tetracycline adsorption. *J. Clean. Prod.* **257**, 120462 (2020).
208. Hu, T. *et al.* Upcycling of Fe-bearing sludge: preparation of erdite-bearing particles for treating pharmaceutical manufacture wastewater. *Sci. Rep.* (2020) doi:10.1038/s41598-020-70080-4.
209. Bahng, J. H. *et al.* Anomalous dispersions of 'hedgehog' particles. *Nature* **517**, 596–599 (2015).
210. Yu, S., Liu, J., Zhou, Y., Webster, R. D. & Yan, X. Effect of synthesis method on the nanostructure and solar-driven photocatalytic properties of TiO2-CuS composites. *ACS Sustain. Chem. Eng.* **5**, 1347–1357 (2017).
211. Deonikar, V. G. *et al.* Growth study of hierarchical Ag3PO4/LaCO3OH heterostructures and their efficient photocatalytic activity for RhB degradation. *Phys. Chem. Chem. Phys.* **19**, 20541–20550 (2017).
212. Goh, C. F. *et al.* Synthesis and cure kinetics of isotropic conductive adhesives comprising sub-micrometer sized nickel particles. *Mater. Sci. Eng. B Solid-State Mater. Adv. Technol.* **117**, 153–158 (2005).
213. Chen, D., Huang, F., Cao, L., Cheng, Y.-B. & Caruso, R. A. Spiky Mesoporous Anatase Titania Beads: A Metastable Ammonium Titanate-Mediated Synthesis. *Chem. - A Eur. J.* **18**, 13762–13769 (2012).
214. Stassi, S. *et al.* Shape-Controlled Synthesis of Silver Nature-Like Spiky Particles for Piezoresistive Sensor Applications. *Eur. J. Inorg. Chem.* **2014**, 2711–2719 (2014).
215. Kumagai, K. & Ishida, A. Synthesis and Optical Properties of Flower- and Spiky-Ball-Like Silver–Gold Nanoparticles. *Bull. Chem. Soc. Jpn.* **87**, 780–791 (2014).
216. Park, Y. K. & Park, S. Directing close-packing of midnanosized gold nanoparticles at a water/hexane interface. *Chem. Mater.* **20**, 2388–2393 (2008).
217. Taylor, P. & Shoesmith, D. W. The nature of green alkaline iron sulfide solutions and the preparation of sodium iron(III) sulfide, NaFeS 2 . *Can. J. Chem.* **56**, 2797–2802 (1978).

218. Tang, Z., Kotov, N. a & Giersig, M. Spontaneous organization of single CdTe nanoparticles into luminescent nanowires. *Science* **297**, 237–240 (2002).
219. Ma, W. *et al.* Mesostructured zinc oxide architectures with high photocatalytic activity. *Mater. Chem. Phys.* **186**, 341–352 (2017).
220. Jiang, W. *et al.* Emergence of complexity in hierarchically organized chiral particles. *Science (80-.).* **368**, 642–648 (2020).
221. Meng, Q., Wang, Q., Liu, H. & Jiang, L. A bio-inspired flexible fiber array with an open radial geometry for highly efficient liquid transfer. *NPG Asia Mater.* **6**, e125 (2014).
222. Nørskov, J. K., Bligaard, T., Rossmeisl, J. & Christensen, C. H. Towards the computational design of solid catalysts. *Nat. Chem.* **1**, 37–46 (2009).